

**Estimation and Characterization of Delay and Angular
Dispersion on Mobile Radio Channels in 2.25 GHz Microcells**

By

Guorui (Gary) Zhang

A thesis submitted to

The Faculty of Graduate Studies and Research

In partial fulfillment for the degree of

Master of Applied Science in Electrical Engineering

Ottawa-Carleton Institute for Electrical and Computer Engineering

Department of Systems and Computer Engineering

Carleton University

Ottawa, Ontario, Canada

© Copyright 2008, Guorui Zhang



Library and
Archives Canada

Published Heritage
Branch

395 Wellington Street
Ottawa ON K1A 0N4
Canada

Bibliothèque et
Archives Canada

Direction du
Patrimoine de l'édition

395, rue Wellington
Ottawa ON K1A 0N4
Canada

Your file Votre référence
ISBN: 978-0-494-40649-6
Our file Notre référence
ISBN: 978-0-494-40649-6

NOTICE:

The author has granted a non-exclusive license allowing Library and Archives Canada to reproduce, publish, archive, preserve, conserve, communicate to the public by telecommunication or on the Internet, loan, distribute and sell theses worldwide, for commercial or non-commercial purposes, in microform, paper, electronic and/or any other formats.

The author retains copyright ownership and moral rights in this thesis. Neither the thesis nor substantial extracts from it may be printed or otherwise reproduced without the author's permission.

AVIS:

L'auteur a accordé une licence non exclusive permettant à la Bibliothèque et Archives Canada de reproduire, publier, archiver, sauvegarder, conserver, transmettre au public par télécommunication ou par l'Internet, prêter, distribuer et vendre des thèses partout dans le monde, à des fins commerciales ou autres, sur support microforme, papier, électronique et/ou autres formats.

L'auteur conserve la propriété du droit d'auteur et des droits moraux qui protègent cette thèse. Ni la thèse ni des extraits substantiels de celle-ci ne doivent être imprimés ou autrement reproduits sans son autorisation.

In compliance with the Canadian Privacy Act some supporting forms may have been removed from this thesis.

Conformément à la loi canadienne sur la protection de la vie privée, quelques formulaires secondaires ont été enlevés de cette thèse.

While these forms may be included in the document page count, their removal does not represent any loss of content from the thesis.

Bien que ces formulaires aient inclus dans la pagination, il n'y aura aucun contenu manquant.

■ ■ ■
Canada

Abstract

Two of the most important factors that influence the ability of mobile radio channels to support high data rate digital communications are dispersion of transmitted signals in delay and angle of arrival. Much has been published in the past regarding both delay and angular dispersion based on measurements in Europe. However, there is a scarcity of similar information for microcells in North America. In addition, all previous work is based on averages from measurements over arbitrary intervals. This thesis has the objective of remedying these problems: results are reported for a North American city, and a novel procedure has been implemented for the selection of averaging intervals so the mixing of data from different channel processes is avoided. The thesis reports on the final stages of development and calibration of a single-input-multiple-output channel sounder, the study, implementation, and testing of algorithms for the high resolution estimation of angles of arrival using a uniform circular array at a mobile receiver, wideband propagation measurements in downtown Ottawa at a centre frequency of 2.25 GHz, the analysis of measured data to determine appropriate averaging intervals, and angular as well as delay dispersion estimates from the analysis of a subset of the recorded data.

Acknowledgements

First and foremost, I would like to thank my thesis supervisor Professor Robert Bultitude for his great support and guidance. His broad knowledge and experience in radio propagation helped me to build a solid understanding in this area even though it was totally new to me at the beginning. I appreciate the opportunity he gave me to work on this project at The Communication Research Centre, Ottawa. Second, I would like to express my gratitude to my thesis co-supervisor Dr. Yvo de Jong for his generous transfer of knowledge concerning the high resolution estimation of angles of arrival. Finally, I would like to thank Hong Zhu and Jeff Pugh for their work during the development of the measurement system and conduct of the propagation experiments.

Partial funding for the work conducted during this thesis project from Dr. Bultitude's NSERC Discovery Grant, Grant Number 299217-05, is also gratefully acknowledged.

Contents

Chapter 1 Introduction.....	1
1.1 Background.....	1
1.2 Objectives.....	9
1.3 Contributions.....	9
1.4 Thesis Outline.....	11
Chapter 2 Theoretical Background and Literature Review.....	13
2.1 Review of AOA Estimation Algorithms.....	13
2.1.1 Data Model.....	13
2.1.2 Array Geometry.....	17
2.1.3 AOA Estimation Algorithms.....	21
2.1.3.1 Beamforming.....	23
2.1.3.2 MUSIC.....	23
2.1.3.3 Forward-Backward Averaging.....	25
2.1.3.4 Spatial Smoothing.....	26
2.1.3.5 Beamspace Processing.....	26
2.1.3.6 ESPRIT.....	28
2.1.3.7 ML & SAGE.....	29

2.1.3.8 Estimation of the Number of Waves.....	30
2.1.3.9 Conclusions.....	31
2.1.4 More Details about UCA-ESPRIT.....	32
2.2 Quantification of Delay Dispersion on Multipath Channels.....	37
2.3 Quantification of Angular Dispersion on Multipath Channels.....	41
2.4 Consistency Intervals.....	43
Chapter 3 Measurement System and Data Analysis Methods.....	47
3.1 Background.....	47
3.2 The CRC Chanprobe Channel Sounder.....	49
3.3 The CRC Chanprobe Switched UCA.....	54
3.4 Measurement Set-up and Data Analysis Methods.....	56
3.4.1 Estimation of RMS Delay Spread.....	64
3.4.2 Estimation of AOAs.....	66
3.4.3 Estimation of Azimuth Angular Spread.....	69
3.4.4 Estimation of Consistency Intervals.....	70
3.5 Calibration Tests.....	74
3.5.1 The Accuracy of AOA Estimation.....	75
3.5.2 The Resolution of AOA Estimation.....	79

Chapter 4 Measurement and Analysis Results.....	83
4.1 Study of AOAs.....	85
4.2 Study of Consistency Intervals.....	88
4.3 Study of RMS Delay Spread.....	96
4.4 Study of Azimuth Angular Spread.....	102
4.5 Study of the Dependence of RMS Delay Spread on Measurement System Bandwidth.....	106
4.5.1 Measurement Results.....	106
4.5.2 Filtered Measurement Results for Different Bandwidths.....	109
4.5.3 Simulations of LOS scenarios.....	112
 Chapter 5 Summary, Conclusions and Recommendations for Further Research...121	
5.1 Summary.....	121
5.2 Conclusions.....	124
5.3 Recommendations for Further Research.....	130
 References.....	133
Acronyms.....	138
Bibliography.....	141

Chapter 1

Introduction

1.1 Background

There has been tremendous demand for wireless communication applications in recent decades. New applications such as Internet access and multimedia services require much higher air interface data rates compared with traditional voice services, thus much wider transmission bandwidths are required. Meanwhile, future wireless systems will use higher carrier frequencies, such as 2 GHz and 6 GHz, and employ sophisticated signal processing, such as space-time processing, and advanced coding schemes. Accurate new, wider bandwidth models for mobile radio channels are therefore important to aid in the design of new systems and products. Therefore, it is of significant importance to measure and characterize mobile radio channels in different environments and different frequency bands.

The microcell concept was introduced in response to the desire for high capacity, high density of subscribers and low transmitter power of mobile terminals in urban areas [1].

The base station (BS) antennas in microcells are usually mounted on poles or lamp posts with heights from 3 to 10 metres above ground, which is relatively low compared with the heights of base station antennas in macrocells, which are normally between 30 to 100 metres. The coverage of a typical microcell is several city blocks, usually in the range from 100 to 1000 metres in diameter.

The dominant radio propagation mechanisms in microcell environments are very different from those in traditional macrocell environments. It is reported [2] that in macrocells, the majority of the received power at the BS is from the direction of the mobile station (MS) in non-line-of-sight (NLOS) situations. This indicates that a significant fraction of the received power propagates from the MS to the BS via diffractions over building rooftops. In microcell environments, however, it is reported in [3] that the majority of the received power at the BS is from the direction of the nearest opening to the street along which the MS is moving in NLOS situations. This indicates that radio waves propagate mainly through street canyons among high buildings.

In a typical mobile wireless scenario, the receiver is moving in an environment with many interacting objects, such as buildings, hills, automobiles, trees, etc., and the line-of-sight (LOS) path is often blocked. In NLOS situations, propagation between the

transmitter and the receiver depends on reflection, diffraction and scattering from interacting objects. Radio waves travel to a mobile receiver over different paths, and therefore arrive from different directions, and have different amplitudes, phases, and delays. This phenomenon is referred to as multipath propagation.

When the receiver is moving, the arriving waves with different phases and amplitudes add up constructively or destructively at the receiver, resulting in the variation of the envelope of the received signal over time and space. The rapid changes in instantaneous received signal strength over a small travel distance or time interval is called multipath fading or small-scale fading. This occurs at the spatial scale on the order of the carrier wavelength, and is therefore frequency dependent. The amplitudes, phases, delays and impinging angles of the arriving waves are difficult to model and predict deterministically, so radio channels are often treated as random processes. Most characterizations of the radio channels are done in a statistical manner, and are based on the analysis of data recorded during propagation experiments made for a specific communication system or operating frequency.

Radio channels set the fundamental limit of how much information can be transmitted and at what quality. An accurate channel model helps designers to maximize the

performance of wireless communication systems. Comprehensive knowledge of radio channels helps to build an accurate channel model. In order to accurately model radio channels, one needs knowledge of the multipath composition of received signals and the way that the multipath composition changes in time and space. With the help of antenna array techniques and high resolution channel sounders, one can identify the angle of arrival (AOA), delay, and power of each multipath component from propagation experiments. This provides an insight into the way that radio waves propagate and how radio channels evolve over time.

Multipath propagation disperses received signals in time, setting the limit on transmission rate. The parameters known as mean excess delay, rms (root mean square) delay spread, and maximum excess delay are used to characterize this time dispersion of radio channels. These parameters can be determined from the average power delay profile (APDP) for the channel of interest. This profile is an average of the squared moduli of radio channel impulse response functions. The maximum excess delay is the time period over which multipath signals with significant energy arrive at the receiver. The mean excess delay is the first moment of the power-weighted delay distribution. The rms delay spread is the power-weighted standard deviation of excess delays with respect to the mean excess delay. The parameter rms delay spread is a good measure of multipath

dispersion and is very important for wideband wireless system design. This is because time dispersion introduces inter-symbol interference (ISI) unless symbol durations are significantly greater than rms delay spreads on the channels of interest. Therefore, without modern signal processing techniques, the maximum practical transmission rate on an unprotected channel is limited by the rms delay spread.

Another important parameter called coherence bandwidth can be approximated based on knowledge of rms delay spread values, with which it has an inverse relationship. Coherence bandwidth sets a limit on the range of frequencies over which the channel exhibits “flat” fading. Time dispersion due to multipath propagation causes the transmitted signal to undergo either flat fading or frequency selective fading. If the coherence bandwidth of the radio channel is much larger than the bandwidth of the transmitted signal, then the received signal will undergo flat fading, and will not be distorted by the radio channel. Typical flat fading channels experience deep fading and the amplitude distribution of the signal is commonly described by a Rayleigh distribution for NLOS scenarios and by a Rician distribution for LOS scenarios. If the coherence bandwidth of the radio channel is smaller than the bandwidth of the transmitted signal, or if the symbol period of the transmitted signal is on the order of or smaller than the rms delay spread of the channel, then the channel creates frequency selective fading of the

received signal. Since the rms delay spread of the channel approaches or is larger than the symbol period of the transmitted signal, ISI is introduced, and this brings about error rate floors that are irreducible no matter how much receiver signal to noise ratio (SNR) is increased, unless channel protection, such as equalization or coding, is employed. Angular spread became an important parameter in the characterization of radio channels when new technologies such as smart antenna and multiple-input-multiple-output (MIMO) systems were introduced. MIMO wireless systems, using multiple antenna elements at the transmitter and receiver, have demonstrated the potential for improved capacity on multipath channels. In such systems, the antenna properties and the multipath channel characteristics ultimately impact the system performance. Angular spread is a measure of how multipath components are distributed in space based on the AOA and multipath signal powers. In a so-called “rich scattering” environment, multipath components arrive randomly from different directions with similar powers, as can be typical in urban NLOS scenarios, where the angular spread at the receiver can be large. On the contrary, the angular spread is small in LOS scenarios. MIMO systems perform better when the correlation of received multipath components is lower, which generally occurs for a large set of multipath components with large angular spread. Hence, the angular spread is an important parameter to describe the spatial characteristics of the radio channel.

Rms delay spreads and rms angular spreads must be estimated from the temporal or spatial average of radio channel characteristics. To effect the needed averaging, one needs to know the lengths over which channel impulse response data should be averaged to estimate APDPs. In order to get useful results, the averaging should be done over intervals that are free from significant changes of channel properties to avoid the mixing of multiple random processes, which can yield misleading results. Herein, such intervals are referred to as consistency intervals (CIs) [4] which are intervals over which the power-weighted cumulative distribution functions (CDFs) for AOA and delays remain approximately the same. In this thesis CIs are estimated using Kolmogorov-Smirnov tests (K-S tests) [5], and averaging is conducted over these intervals for the estimation of rms delay spreads and angular spreads. Radio propagation experiments were conducted in downtown Ottawa using a channel sounder built at the Communications Research Centre (CRC). The transmit antenna was raised to a height near 5 metres according to the typical microcell configuration. The receive antenna was a uniform circular array (UCA), also built at CRC, mounted on a moving minivan. Downtown Ottawa is a typical North American downtown area with rectangular street grids and high buildings.

There are many reports of propagation loss, impulse response, and angle of arrival information derived from propagation measurements in both macrocellular and microcellular mobile radio environments in different parts of the world. There are also papers that deal with the definition and methods for the measurement, analysis, and modeling of both rms delay spreads and rms angular spreads. While rms delay spreads are reported in much of the past literature, the concept of and requirement for, information on angular spreads is much newer, and some reports that focus on their estimation, modeling and associated measurements in situations other than at the mobile station in a microcellular environment are listed in the bibliography at the end of this thesis. However, following an extensive literature search, only one report could be found [3] of rms delay spread and rms azimuth spread values estimated from the same data measured at a mobile station. The cited report is based on measurements in Paris, where streets mostly have random orientations and are often not straight, whereas the streets in the area where measurements reported herein were conducted are laid out in a rectangular grid.

1.2 Objectives

The objective of this thesis is to characterize the delay and angular dispersion in microcells. First, in order to estimate rms delay spreads and angular spreads, one must determine the intervals that should be used for averaging measured data. It is believed that this interval should be the CI between significant changes of the radio channel. Therefore, one needs a method to identify significant changes of channel properties to determine the CI. Second, one needs to find a suitable AOA estimation algorithm for use with data measured using a circular array to accurately and efficiently estimate AOAs. Third, one needs to carry out propagation experiments in microcells to record the data for analysis. This thesis report gives a description how each of these tasks were carried out, and presents analysis results in the form of channel parameters and the statistics thereof.

1.3 Contributions

The main contributions of the thesis are in the development and implementation of procedures, methods, and algorithms for the estimation and modeling of the parameters of interest, including:

- A study and evaluation of different high-resolution AOA estimation algorithms.
- Writing MATLAB codes for the processing of measured data, and for the implementation of algorithms to estimate the AOA, rms delay spreads angular spreads and CIs, as well as for various channel simulations.
- Determination of the accuracy and resolution capabilities of the measurement equipment.
- Determination of the statistics of rms delay spreads and azimuth angular spreads for the measured radio channels.
- Determination of the statistics of CIs, in other words, the statistics of change, on the measured radio channels.
- Determination of the dependence of rms delay spreads on measurement system bandwidth.
- Channel simulations using a geometrical model for LOS scenarios.

1.4 Thesis Outline

This thesis is organized as follows.

- Chapter 1 explains what multipath propagation is and what problems it can cause on radio channels, why it is necessary to characterize and model microcellular mobile channels, as well as the importance of rms delay spreads, angular spreads, and CIs. This chapter also gives the objectives and contributions of this thesis work.
- Chapter 2 is a review and evaluation of the most popular high-resolution AOA estimation algorithms. This chapter also contains a review of some previous work concerning rms delay spread, angular spread, and CIs in microcells.
- Chapter 3 describes the measurement system, including the channel sounder, the switched UCA, and the measurement set-up in the field. It also discusses methods for the estimation of rms delay spreads, angular spreads, and CIs that are used in this thesis work. Finally, calibration tests to determine the accuracy and resolution of the measurement equipment are reported.
- Chapter 4 reports AOA, CI, rms delay spread, and azimuth angular spread results estimated from selected measurement data. Experimentally-determined cumulative distribution functions (ECDFs) for rms delay spreads, azimuth angular spreads, and CIs for three typical propagation scenarios (LOS, NLOS on perpendicular streets,

and NLOS on parallel streets) are given. Additionally, a report on the dependence of rms delay spread on measurement system bandwidth based on both experiments and simulations is presented.

- Chapter 5 contains conclusions from the entire work and recommendations for future research.

Chapter 2

Theoretical Background and Literature Review

2.1 Review of AOA Estimation Algorithms

2.1.1 Data Model

In this section, a data model [6] that is generally used in array signal processing and will be used throughout this thesis is presented. One of the assumptions of this model is that the receive antenna is in the far-field of the source of energy incident upon it, so that impinging waves are plane waves. In the intended application, it is recognized that this will not always be strictly true. However, since the absolute physical extent of the receive antenna aperture is small compared with distances to large reflectors, such as buildings along the streets in the measurement area, the plane wave assumption is considered to be a good approximation in many cases, and it is considered probable that this would render associated errors to be insignificant in the estimation of averages. This assumption will therefore be carried in theoretical developments to follow, for the estimation of angles of arrival. In order for the plane-wave assumption to hold, the physical size of the array should be much smaller than the distance, r , between the array

and the interacting object, which could be any object in the environment acting as a secondary source of multipath components, and r should be greater than $2D^2/\lambda$, where λ represents the wavelength at the operating frequency and D is the aperture of the interacting object. It is also assumed that the signal bandwidth is much smaller than the inverse of the time needed for a radio wave to travel across the length of the array aperture (narrowband assumption). Through this assumption, each multipath signal is received identically at all antenna elements except for a phase shift.

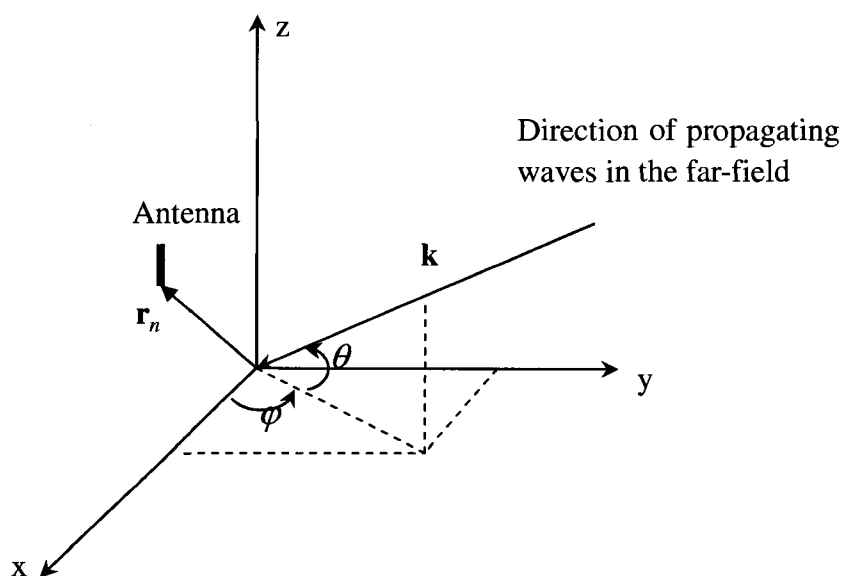


Fig. 2.1 Three-dimensional geometric model.

In Fig. 2.1, a receive antenna and the direction of arriving plane waves are shown in

three-dimensional coordinates. The AOA is defined by the azimuth angle $\varphi \in [0, 360^\circ]$ and the elevation angle $\theta \in [-90^\circ, 90^\circ]$. The wave-vector \mathbf{k} points in the direction of propagation and its magnitude $|\mathbf{k}| = k = \omega/c = 2\pi/\lambda$ (where λ is the wavelength of the arriving waves) is called the wave-number. In this case, $\mathbf{k} = k[\cos\varphi\cos\theta \quad \sin\varphi\cos\theta \quad \sin\theta]^T$. The radius vector \mathbf{r}_n points to the position of the n th sensor and $\mathbf{r}_n = [x_n \quad y_n \quad z_n]^T$.

The output of the n th receive antenna can be written as

$$x_n = s(t)e^{-j\mathbf{r}_n^T\mathbf{k}} = a_n(\varphi, \theta)s(t), \quad (2-1)$$

where $s(t)$ denotes the baseband signal.

For an N -element antenna array of arbitrary geometry, the signals received by all antenna elements can be represented by an array output vector as

$$\mathbf{x}(t) = \mathbf{a}(\varphi, \theta)s(t), \quad (2-2)$$

where $\mathbf{a}(\varphi, \theta) = [a_1(\varphi, \theta), \dots, a_N(\varphi, \theta)]^T$ is called the array response vector. If L signals from different directions impinge on an N -element array, the superposition principle is applied as

$$\mathbf{x}(t) = \mathbf{A}(\varphi, \theta)s(t), \quad (2-3)$$

where $\mathbf{A}(\varphi, \theta) = [\mathbf{a}(\varphi_1, \theta_1), \dots, \mathbf{a}(\varphi_L, \theta_L)]$ is called the array response matrix.

In the presence of additive white noise $\mathbf{n}(t)$, the model for the array output that is commonly used in array signal processing is given by

$$\mathbf{x}(t) = \mathbf{A}(\varphi, \theta)\mathbf{s}(t) + \mathbf{n}(t). \quad (2-4)$$

To characterize the spatial correlation among the signals at the various antenna elements, the spatial covariance matrix of the array output is defined as

$$\mathbf{R} = E[\mathbf{x}(t)\mathbf{x}^H(t)] = \mathbf{A} E[\mathbf{s}(t)\mathbf{s}^H(t)]\mathbf{A}^H + E[\mathbf{n}(t)\mathbf{n}^H(t)], \quad (2-5)$$

where $E[\cdot]$ denotes statistical expectation,

$$E[\mathbf{s}(t)\mathbf{s}^H(t)] = \mathbf{P}, \quad (2-6)$$

is the source covariance matrix and

$$E[\mathbf{n}(t)\mathbf{n}^H(t)] = \sigma^2 \mathbf{I}, \quad (2-7)$$

is the noise covariance matrix. \mathbf{I} denotes the identity matrix and σ^2 is the variance of the white noise at each antenna element. With eigendecomposition of the square matrix \mathbf{R} , \mathbf{R} can be represented as

$$\mathbf{R} = \mathbf{A}\mathbf{P}\mathbf{A}^H + \sigma^2 \mathbf{I} = \mathbf{U}\mathbf{\Lambda}\mathbf{U}^H = \mathbf{U}_s \mathbf{\Lambda}_s \mathbf{U}_s^H + \mathbf{U}_n \mathbf{\Lambda}_n \mathbf{U}_n^H, \quad (2-8)$$

with eigenvectors \mathbf{U} , and $\mathbf{\Lambda} = \text{diag}[\lambda_1, \lambda_2, \dots, \lambda_N]$ is a diagonal matrix of real eigenvalues ordered such that $\lambda_1 \geq \lambda_2 \geq \dots \geq \lambda_N > 0$. One can partition the eigenvalue and eigenvector pairs into the signal subspace (corresponding to eigenvalues $\lambda_1 \geq \dots \geq \lambda_L > \sigma^2$), which is spanned by the columns of \mathbf{U}_s , and the noise subspace

(corresponding to eigenvalues $\lambda_{L+1} = \dots = \lambda_N = \sigma^2$), which is spanned by the columns of \mathbf{U}_n .

In practice, an estimate of \mathbf{R} (denoted by a hat) is obtained by averaging over several snapshots

$$\hat{\mathbf{R}} = \frac{1}{T} \sum_{t=1}^T \mathbf{x}(t)\mathbf{x}^H(t). \quad (2-9)$$

This representation will be used in the description and implementation of the subspace-based estimation algorithms in the following sections.

2.1.2 Array Geometry

Array geometry and antenna element characteristics place fundamental limitations on the performance of AOA estimation techniques. A comparison of the benefits and disadvantages of different planar array geometries based on detection, resolution, and accuracy criteria has been reported in [7]. In the following section, three array geometries are briefly reviewed. These include: The uniform linear array (ULA), which is a one-dimensional array, the UCA, which is a two-dimensional array, and the uniform tilted cross array (UTCA) [8], which is a three-dimensional array.

A one-dimensional array can provide AOA estimation relative to the array axis. The ULA can estimate azimuth angles correctly only if the elevation angle with which they impinge is zero, and with a 180 degree ambiguity. The ULA is an array of identical antenna elements lined up on a straight line with equal inter-element spacing between all adjacent elements, as depicted in Fig. 2.2.

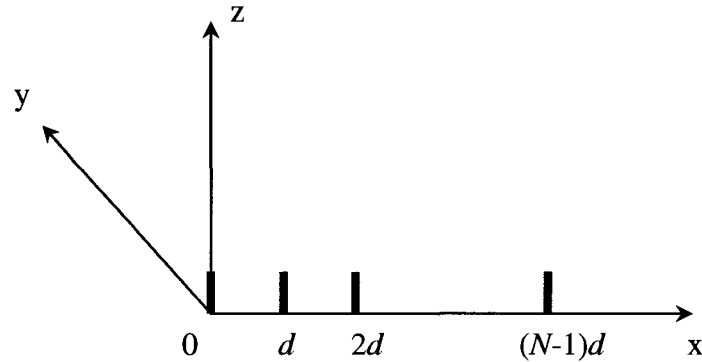


Fig. 2.2 ULA geometry.

For the ULA, $\mathbf{r}_n = [(n-1)d \ 0 \ 0]^T$, $n = 1, 2, \dots, N$, where d denotes the inter-element spacing. From Eq. (2-1), the array response vector is given by

$$\mathbf{a}_{ULA}(\varphi) = \left[1 \ e^{jkd \cos \varphi} \ \dots \ e^{j(N-1)kd \cos \varphi} \right]^T. \quad (2-10)$$

A ULA oriented along the x-axis has the lowest resolution for azimuth angles close to 0° and 180° , and the highest resolution for azimuth angles close to 90° .

The array response matrix of the ULA is a Vandermonde matrix (each column has a constant magnitude and each element undergoes a linear phase increase), which takes the form

$$\mathbf{A}(\varphi) = \begin{bmatrix} 1 & 1 & \dots & 1 \\ e^{j\psi 1} & e^{j\psi 2} & \dots & e^{j\psi L} \\ \vdots & \vdots & & \vdots \\ e^{j(N-1)\psi 1} & e^{j(N-1)\psi 2} & \dots & e^{j(N-1)\psi L} \end{bmatrix}, \quad (2-11)$$

where $\psi = kd \cos \varphi$.

Some AOA estimation algorithms (ESPRIT, root-MUSIC, etc) and some techniques used to improve the performance of AOA estimation algorithms (forward-backward averaging, spatial smoothing, etc) exploit this structure and can be only applied to arrays that have this structure.

A two-dimensional array is required to estimate both azimuth and elevation angles, but it has a 180 degree ambiguity in elevation angles. It could, for example, be an array of identical antenna elements uniformly distributed on a circle, commonly referred to as a uniform circular array as shown in Fig. 2.3.

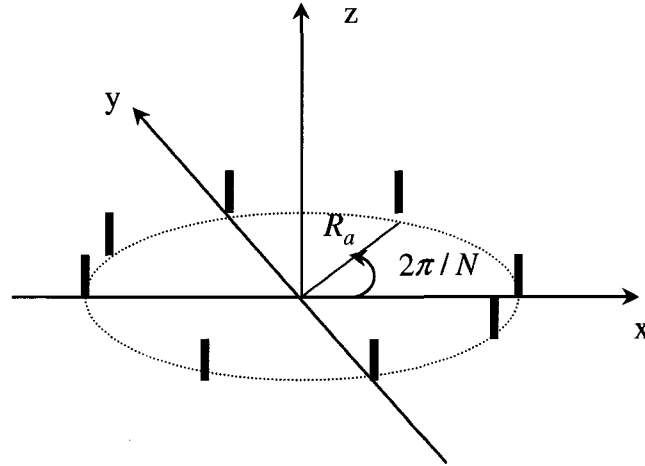


Fig. 2.3 UCA geometry.

For the UCA, $\mathbf{r}_n = [R_a \cos(2\pi(n-1)/N) \quad R_a \sin(2\pi(n-1)/N) \quad 0]^T$, $n = 1, 2, \dots, N$, where R_a denotes the radius of the circle. From Eq. (2-1), the array response vector for a UCA can be written as

$$\mathbf{a}_{UCA}(\varphi, \theta) = \left[e^{-jkR_a \sin \theta \cos \varphi} \quad e^{-jkR_a \sin \theta \cos(\varphi - \frac{2\pi}{N})} \quad \dots \quad e^{-jkR_a \sin \theta \cos(\varphi - \frac{2\pi(N-1)}{N})} \right]^T. \quad (2-12)$$

One significant advantage of a UCA lying in the horizontal plane is that it has uniform performance at all azimuth angles.

A three-dimensional array can provide data for the estimation of both azimuth and elevation angles without ambiguity. An example is a UTCA, which is an array that consists of three ULAs orthogonal to each other. Such an array has already been

implemented at CRC [8] and is now being used for measurements in Europe. A second such array is now being implemented at CRC for future measurements in Canada.

2.1.3 AOA Estimation Algorithms

Array signal processing is the analysis, interpretation, and manipulation of signals induced on antenna array elements for different applications, including pointing radio beams towards desired directions and estimating parameters such as directions of radiating sources. Direction finding by antenna arrays has been of great interest in research related to sonar, radar, seismology, mobile communication systems, etc. for many years. AOA estimation techniques exploit the temporal data collected by antenna array elements at fixed, pre-determined intervals (snapshots) and the prior information of the antenna array (array geometry, sensor characteristics, etc.) to carry out given estimation tasks (space-time processing). AOAs and complex voltages of arriving signals are important parameters that are required to calculate the angular dispersion of the radio channels. One objective of this thesis is to estimate two-dimensional AOAs (both azimuth and elevation angles), excess delays, amplitudes and phases of received multipath signals with as great resolution in each domain as possible and as small a number of snapshots as possible at a moving UCA receiver under realistic measurement

SNR conditions. This section provides a brief overview of today's most commonly used techniques for AOA estimation.

According to [6], most popular estimation techniques can be roughly categorized as shown in Fig. 2.4. A detailed comparison of commonly used AOA estimation algorithms is provided in [9], including a report of accuracy (bias), resolution, variance, sensitivity, computational load, and performance. The most studied techniques, such as beamforming, MUSIC (Multiple Signal Classification), ESPRIT (Estimation of Signal Parameters via Rotational Invariance Techniques), SAGE (Space-Alternating Generalized Expectation-maximization), are briefly reviewed in the following sections.

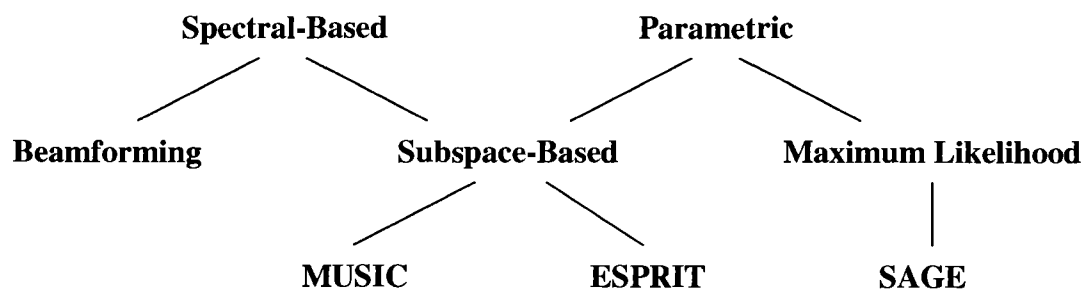


Fig. 2.4 Category of AOA estimation algorithms.

2.1.3.1 Beamforming

The Beamforming method is a conventional Fourier-based spectral analysis (spatial filtering). A detailed review of beamforming techniques is presented in [10]. A beamforming algorithm can be used to estimate the AOAs with only one snapshot (a set of complex voltages collected by array elements at the same time or in a period much smaller than the coherence time of the channel). The result of searching among possible AOAs forms a spectrum and the highest peaks of the spectrum are recorded as the AOA estimates. The resolution (the ability to distinguish closely spaced signal sources) of the beamforming algorithm mainly depends on the array aperture (physical size of the array).

2.1.3.2 MUSIC

The MUSIC algorithm was introduced in [11] and resulted in tremendous interest in the signal subspace approach for high resolution AOA estimation. Subspace-based methods offer clear performance improvements compared to conventional beamforming methods. High resolution and accuracy is achieved when the number of snapshots and SNR are sufficiently large and the data model accurately reflects the experimental scenario. Subspace-based methods are based on the eigenvalue decomposition of the array covariance matrix. When the environment consists of uncorrelated directional sources

and uncorrelated white noise, the eigenstructure is partitioned into two subspaces: the signal subspace and the noise subspace. The subspace spanned by the signal eigenvectors is referred to as the signal subspace whereas the subspace spanned by the noise eigenvectors is referred to as the noise subspace. Since all eigenvectors are orthogonal to each other, the signal subspace and the noise subspace are orthogonal to each other. The array response vectors corresponding to AOAs are orthogonal to the noise subspace and are contained in the signal subspace. In practice, the algorithm estimates the Euclidean distance from an array response vector $\mathbf{a}(\varphi, \theta)$ (with any possible φ and θ combination) to the signal subspace and searches for minima. The MUSIC spectrum is the reciprocal of this distance, and is defined as

$$P_{MUSIC} = \frac{1}{\mathbf{a}^H(\varphi, \theta) \mathbf{U}_n \mathbf{U}_n^H \mathbf{a}(\varphi, \theta)}. \quad (2-13)$$

A search typically shows peaks in the vicinity of the true AOAs in the MUSIC spectrum. The MUSIC algorithm is applicable to arbitrary array geometries and can be used to estimate AOAs, complex voltages, and polarizations. Performance of the MUSIC degrades significantly when:

- The arriving signals are correlated or coherent (two signals are coherent if one is a scaled and delayed version of the other), which is the case for signals in a multipath propagation environment, as shown in [12]. This is because of a rank deficiency in

the source covariance matrix.

- The number of snapshots is small and the SNR is low, which is common in practical mobile applications. The associated loss of resolution is more pronounced for highly correlated signals. And the collected snapshots should not be highly correlated, which means either the transmitter or the receiver must be moving or the propagation channel must be changing due to moving interacting objects.

Two methods are available to deal with the problem of estimation information about coherent signals: forward-backward averaging and spatial smoothing, as outlined in the following.

2.1.3.3 Forward-Backward Averaging

Forward-backward averaging [6] can be applied to data measured using arrays with a centro-symmetric array response matrix, such as a ULA, in order to double the rank of the covariance matrix, for a given number of measurement snapshots, thus reducing the distance over which data must be recorded for equivalent results. Forward-backward averaging is applied to the covariance matrix, in accordance with

$$\mathbf{R}_{FB} = \frac{1}{2}(\mathbf{R} + \mathbf{J}\mathbf{R}^*\mathbf{J}) = \mathbf{A}\tilde{\mathbf{P}}\mathbf{A} + \sigma^2\mathbf{I}, \quad (2-14)$$

where \mathbf{J} is the anti-diagonal identity matrix. The resulting covariance matrix $\tilde{\mathbf{P}}$ generally has full rank.

2.1.3.4 Spatial Smoothing

A technique called spatial smoothing [13, 14] can also be applied to solve the rank deficiency problem. The data recorded on the array is divided into a number of data vectors from overlapping subarrays that have the same structure, and the covariance matrices of the subarrays are then averaged. The rank of the averaged covariance matrix increases by 1 for each additional subarray in the averaging. The drawback of the spatial smoothing technique is that it only applies to arrays with a translational invariance property, such as the ULA and the uniform rectangular array, and the effective array aperture is reduced, resulting in degradation of the resolution.

2.1.3.5 BeamSpace Processing

Another important technique used to improve the performance of AOA estimation algorithms is known as beamspace processing. In contrast to element space algorithms where the received signals are directly passed to the AOA estimation algorithm,

beam-space processing involves passage of the array data through a beamforming processor before processing by the AOA estimation algorithm. The array data vector and the array response vector are both first multiplied by a beamformer to obtain beam-space vectors. Beam-space processing has some distinct advantages such as reduced computational load, improved resolution, reduced sensitivity to system errors, and reduced bias in resulting estimates of signal parameters [12]. By proper design of the beamformer for a UCA, the beam-space array response vector can be given the structure of a ULA. Therefore, ULA techniques such as spatial smoothing can be made applicable in beam-space. In [15], a transformation that maps a UCA into a ULA is proposed and analyzed, enabling estimation of both azimuth and elevation in beam-space. An algorithm called UCA_RB_MUSIC (RB represents Real Beam-space) is described, offering numerous advantages over element space operation, including reduced computational load (since subspace estimates are obtained via real-valued eigendecompositions), enhanced performance in correlated source scenarios (due to the attendant forward-backward averaging effect), and compatibility with the spatial smoothing technique when elevation angles are known.

2.1.3.6 ESPRIT

The ESPRIT algorithm [16] is a computationally efficient and robust method of AOA estimation. It must be used with an antenna array that can be divided into two identical subarrays, in which paired elements of the two subarrays have an identical displacement vector. The signal subspace estimates are obtained by eigenvalue decompositions, and the AOA estimates are obtained by the least squares or total least squares solution of an overdetermined system of equations. Thus, expensive search procedures, such as those required when the MUSIC algorithm is used are avoided. ESPRIT can provide estimation of both azimuth and elevation angles if used with planar arrays having a centro-symmetric structure [17]. For a UCA, an algorithm called UCA-ESPRIT [15] provides closed-form, automatically paired azimuth and elevation estimates. This algorithm will be discussed in the following section. As a subspace-based method, ESPRIT cannot handle coherent signals unless techniques such as forward-backward averaging and spatial smoothing, and the recording of multiple measurement snapshots are used. It should also be noted that ESPRIT results in greater variance of AOA estimates than MUSIC.

2.1.3.7 ML & SAGE

The Maximum Likelihood (ML) method [18] is another important method that can be used to estimate AOAs. The estimates obtained by this method are unbiased, which means the expected values of the estimates are equal to their true values. The ML method can be applied when there is only one snapshot and for arbitrary geometries. It results in superior performance compared to the methods mentioned above particularly when SNR is small and the sources are coherent. However, the extensive computational burden due to the multidimensional search required to find the AOAs makes it prohibitive for practical application.

An algorithm called SAGE [19] was proposed to replace the high-dimensional optimization procedure required in the ML method by several separate maximization processes, which can be performed sequentially. The SAGE algorithm improves the convergence rate. The actual convergence rate, however, depends on the accuracy of the initial estimate, which is usually obtained by methods such as beamforming, or MUSIC.

2.1.3.8 Estimation of the Number of Waves

Many high resolution AOA estimation algorithms, such as MUSIC, ESPRIT, and SAGE, require the apriori estimation of the number of impinging waves and their performance is dependent on the correct estimation of this number. The most commonly used methods for estimating the number of waves are based on Akaike's Information Criterion (AIC) and Rissanen's Minimum Description Length (MDL) [20]. The number of waves is equal to the number of "large" eigenvalues of the array covariance matrix, and the rest "small" eigenvalues equal to σ^2 correspond to the noise subspace. In practice, however, the noise eigenvalues are all different, making it difficult to determine the number of signals by only observing the eigenvalues. The AIC and MDL methods search for the number of signals that maximizes the log likelihood function of the eigenvalues. The AIC criterion is given by

$$AIC(n) = -2 \log \left(\frac{\prod_{i=n+1}^p l_i^{1/(p-n)}}{\frac{1}{p-n} \sum_{i=n+1}^p l_i} \right)^{(p-n)M} + 2n(2p-n), \quad (2-15)$$

while the MDL criterion is given by

$$MDL(n) = -\log \left(\frac{\prod_{i=n+1}^p l_i^{1/(p-n)}}{\frac{1}{p-n} \sum_{i=n+1}^p l_i} \right)^{(p-n)M} + \frac{1}{2} n(2p-n) \log M, \quad (2-16)$$

where $l_i = \lambda_i$ ($(i = 1, \dots, p)$) and M is the number of snapshots.

The number of signals is determined as the value of $n \in [0, 1, \dots, p-1]$ for which either the AIC or the MDL function is minimized.

2.1.3.9 Conclusions

Several AOA estimation techniques are briefly reviewed above and their performance, advantages, and limitations are discussed. Although SAGE and UCA-RB-MUSIC are more accurate and can be applied with fewer snapshots, UCA-ESPRIT was chosen for use in the final analysis of measured data during this thesis project for the following reasons:

- It is computational efficient compared with UCA-RB-MUSIC and SAGE. UCA-ESPRIT is more than 10 times faster than UCA-RB-MUSIC in practice, and does not sacrifice much performance.
- It has enhanced performance in correlated source scenarios, due to forward-backward averaging.
- It works with the UCA to provide closed-form 2D angle estimation, which meets the requirement of this thesis.
- Beamspace processing, which is inherent with this algorithm, has distinct advantages compared with element-space processing, such as reduced computational load,

improved resolution, and reduced bias in AOA estimates.

2.1.4 More Details about UCA-ESPRIT

The UCA-ESPRIT algorithm is fundamentally different from ESPRIT because it is not based on the displacement invariant array structure required by ESPRIT. The detailed development of UCA-ESPRIT algorithm is presented in [15], and it will be briefly summarized in this section.

UCA-ESPRIT is a closed-form algorithm that provides automatically paired source azimuth and elevation estimates. The signal subspace estimates are obtained by real-valued eigenvalue decompositions, and the automatically paired AOA estimates are obtained through knowledge of the eigenvalues of the matrix Ψ which is obtained from the least squares solution to an overdetermined system of equations. Therefore, expensive search procedures, as required with MUSIC and SAGE are avoided. Practical data analysis that was conducted by the candidate shows that UCA-ESPRIT is more than 10 times faster than UCA-RB-MUSIC. Both algorithms were implemented during this thesis project.

The array response vector of a UCA in element space is given by

$$\mathbf{a}(\varphi, \theta) = \begin{bmatrix} e^{-jkR_a \sin \theta \cos \varphi} \\ e^{-jkR_a \sin \theta \cos(\varphi - \frac{2\pi}{N})} \\ e \\ \vdots \\ e^{-jkR_a \sin \theta \cos(\varphi - \frac{2\pi(N-1)}{N})} \\ e \end{bmatrix}. \quad (2-17)$$

A beamformer \mathbf{F}_r^H is employed to make the transformation from element space to beamspace. This essentially Fourier transforms the spatial sequence of complex voltages in the above-given element space array response vector, which for a UCA, is periodic. The resulting spectrum in beamspace is thus discrete, having energy at a finite number of spectral positions, which are harmonics or multiples of a fundamental angular spacing, often referred to as beams or eigenmodes. This number is given by

$$N_b = 2M + 1, \quad (2-18)$$

where M is the index, or order, of the highest-ordered eigenmode that can exist at reasonable strength. The index M is a function of the complexity of variations of the spatial sequence of array element voltages, and hence, for fixed uniform, element spacing, the radius of the UCA [15]. It can be approximated by

$$M = kR_a. \quad (2-19)$$

The beamformer \mathbf{F}_r^H is defined by

$$\mathbf{F}_r^H = \mathbf{W}^H \mathbf{C}_v \mathbf{V}^H, \quad (2-20)$$

where,

$$\mathbf{W} = \frac{1}{\sqrt{N_b}} \begin{bmatrix} e^{\eta_b(-M)(-M)} & e^{\eta_b(-M)(-M+1)} & \dots & e^{\eta_b(-M)(0)} & \dots & e^{\eta_b(-M)(M-1)} & e^{\eta_b(-M)(M)} \\ e^{\eta_b(-M+1)(-M)} & e^{\eta_b(-M+1)(-M+1)} & \dots & e^{\eta_b(-M+1)(0)} & \dots & e^{\eta_b(-M+1)(M-1)} & e^{\eta_b(-M+1)(M)} \\ \vdots & \vdots & & \vdots & & \vdots & \vdots \\ e^{\eta_b(0)(-M)} & e^{\eta_b(0)(-M+1)} & \dots & e^{\eta_b(0)(0)} & \dots & e^{\eta_b(0)(M-1)} & e^{\eta_b(0)(M)} \\ \vdots & \vdots & & \vdots & & \vdots & \vdots \\ e^{\eta_b(M-1)(-M)} & e^{\eta_b(M-1)(-M+1)} & \dots & e^{\eta_b(M-1)(0)} & \dots & e^{\eta_b(M-1)(M-1)} & e^{\eta_b(M-1)(M)} \\ e^{\eta_b(M)(-M)} & e^{\eta_b(M)(-M+1)} & \dots & e^{\eta_b(M)(0)} & \dots & e^{\eta_b(M)(M-1)} & e^{\eta_b(M)(M)} \end{bmatrix}$$

in which $\eta_b = j \frac{2\pi}{N_b}$,

$\mathbf{C}_v = \text{diag}\{j^{-M} \quad j^{-M+1} \quad \dots \quad j^{-1} \quad j^0 \quad j^{-1} \quad \dots \quad j^{-M+1} \quad j^{-M}\}$, and

$$\mathbf{V} = \begin{bmatrix} 1 & 1 & \dots & 1 & \dots & 1 & 1 \\ e^{\eta(1)(-M)} & e^{\eta(1)(-M+1)} & \dots & e^{\eta(1)(0)} & \dots & e^{\eta(1)(M-1)} & e^{\eta(1)(M)} \\ \vdots & \vdots & & \vdots & & \vdots & \vdots \\ e^{\eta(N-2)(-M)} & e^{\eta(N-2)(-M+1)} & \dots & e^{\eta(N-2)(0)} & \dots & e^{\eta(N-2)(M-1)} & e^{\eta(N-2)(M)} \\ e^{\eta(N-1)(-M)} & e^{\eta(N-1)(-M+1)} & \dots & e^{\eta(N-1)(0)} & \dots & e^{\eta(N-1)(M-1)} & e^{\eta(N-1)(M)} \end{bmatrix},$$

in which $\eta = j \frac{2\pi}{N}$.

The transformation is effected through the equation

$$\mathbf{x}_b(t) = \mathbf{F}_r^H \mathbf{x}(t), \quad (2-21)$$

and the beamspace covariance matrix is given by

$$\mathbf{R}_b = \mathbf{E}[\mathbf{x}_b(t)\mathbf{x}_b^H(t)]. \quad (2-22)$$

Let $\mathbf{R}_r = \text{Re}\{\mathbf{R}_b\}$ denote the real part of the beamspace covariance matrix. Performing the real-valued eigenvalue decomposition of the matrix \mathbf{R}_r and applying either the AIC or the MDL algorithm to estimate the number of waves, one can estimate the ordered eigenvalues of $\lambda_1 \geq \dots \geq \lambda_L$ spanning the signal subspace and $\lambda_{L+1} \geq \dots \geq \lambda_{N_b}$ spanning the noise subspace respectively.

The objective is to solve for $\hat{\Psi}$ from the equation $\hat{\Psi} = [\hat{\Psi}^T \quad \hat{\Psi}^H]^T$, which is the solution to the equation

$$\hat{\mathbf{E}}\hat{\Psi} = \Gamma\hat{\mathbf{S}}^{(0)}, \quad (2-23)$$

where $\Gamma = (\lambda/\pi R_a) \text{diag}\{-(M-1) \quad \dots \quad -1 \quad 0 \quad 1 \quad \dots \quad (M-1)\}$, and λ is the wavelength of the arriving waves.

Then,

$$\hat{\mathbf{E}} = [\hat{\mathbf{S}}^{(-1)} \quad \mathbf{D}\tilde{\mathbf{I}}\hat{\mathbf{S}}^{(-1)*}], \quad (2-24)$$

where $\mathbf{D} = \text{diag}\{(-1)^{(M-2)} \quad \dots \quad (-1)^1 \quad (-1)^0 \quad (-1)^1 \quad \dots \quad (-1)^M\}$ and $\tilde{\mathbf{I}}$ is the reverse permutation matrix with ones on the anti-diagonal and zeros elsewhere.

Matrices $\hat{\mathbf{S}}^{(0)}$ and $\hat{\mathbf{S}}^{(-1)}$ are obtained from the equation

$$\hat{\mathbf{S}}^{(i)} = \mathbf{\Delta}^{(i)}\hat{\mathbf{S}}_o, \quad i = -1, 0, 1, \quad (2-25)$$

here $\mathbf{\Delta}^{(-1)}$, $\mathbf{\Delta}^{(0)}$, and $\mathbf{\Delta}^{(1)}$ are the selection matrices, used to pick out the first, middle, and last $N_b - 2$ elements from $\hat{\mathbf{S}}_o$. Thus, $\mathbf{\Delta}^{(-1)}$ is given by

$$\mathbf{\Delta}^{(-1)} = \begin{bmatrix} 1 & & 0 & 0 & 0 \\ & \ddots & & & \\ 0 & & 1 & 0 & 0 \end{bmatrix}, \quad (2-26)$$

and $\mathbf{\Delta}^{(0)}$ is given by

$$\mathbf{\Delta}^{(0)} = \begin{bmatrix} 0 & 1 & & 0 & 0 \\ \vdots & & \ddots & & \vdots \\ 0 & 0 & & 1 & 0 \end{bmatrix}. \quad (2-27)$$

The matrix $\hat{\mathbf{S}}_o$ which spans the beamspace array response matrix is given by

$$\hat{\mathbf{S}}_o = \mathbf{C}_o \mathbf{W} \hat{\mathbf{S}}, \quad (2-28)$$

where $\mathbf{C}_o = \text{diag}\{(-1)^M \quad (-1)^{M-1} \quad \dots \quad (-1)^1 \quad 1 \quad \dots \quad 1\}$ and $\hat{\mathbf{S}}$ is the matrix of eigenvectors that span the signal subspace.

Since, by using the foregoing equations, one has the knowledge of the matrices $\hat{\mathbf{E}}, \mathbf{\Gamma}$, and $\hat{\mathbf{S}}^{(0)}$, one can use least-square methods or total-least-squares methods to solve for $\hat{\mathbf{\Psi}}$, or simply use the inverse matrix method, which is given by

$$\hat{\mathbf{\Psi}} = \text{inv}(\hat{\mathbf{E}}^H \hat{\mathbf{E}}) \hat{\mathbf{E}}^H \mathbf{\Gamma} \hat{\mathbf{S}}^{(0)}. \quad (2-29)$$

And $\hat{\mathbf{\Psi}}$ can be obtained from $\hat{\mathbf{\Psi}} = [\hat{\mathbf{\Psi}}^T \quad \vdots \quad \hat{\mathbf{\Psi}}^H]^T$. The estimates of the azimuth and elevation angles are obtained from the eigenvalues of $\hat{\mathbf{\Psi}}$, which can be denoted as μ_i , $i = 1, \dots, L$. The azimuth angle is obtained by $\varphi_i = \arg(\mu_i)$ and the elevation angle is obtained through the equation $\theta_i = \cos^{-1}(|\mu_i|)$.

2.2 Quantification of Delay Dispersion on Multipath Channels

Multipath delay spread and coherence bandwidth are parameters that describe the time dispersive nature of a radio channel in the time (delay) and frequency domains, respectively. Time dispersion is the result of multipath propagation and varies widely on different mobile radio channels.

The estimation of rms delay spread is a good measure of the multipath spread and is very important for wideband wireless system design, because time dispersion introduces ISI as the rms delay spread on the channel approaches a significant fraction of symbol durations. That is, the maximum practical transmission rate on an unprotected fading channel is limited by the rms delay spread. Strong echoes with long delays contribute significantly to the rms delay spread. There will be ISI if the symbol period is less than about 10 times the rms delay spread, and it begins to be serious when the symbol period is only marginally greater than the rms delay spread. When ISI becomes significant, error rate floors are encountered such that one cannot decrease the probability of error on the channel by simply increasing SNR. Therefore, equalization, or diversity are required to achieve better performance.

Many measurements have been made and propagation models have been reported for conventional macrocells with high-powered base stations and elevated antennas. In such systems, LOS propagation is mostly blocked in an urban area. The multipath propagation results in Rayleigh fading of received signal envelopes. Recent research concerning both delay spread and angular spread in a macrocell environment is reported in [2]. Wideband experiments were conducted in Aarhus, Denmark, and Stockholm, Sweden at a carrier frequency of 1.8 GHz. The distributions of AOAs in azimuth angle and of multipath signal delays as well as the estimated power of associated multipath signals were obtained from the measurements and a statistical model of azimuthal and temporal dispersion on mobile channels was proposed. The power azimuth spectrum (PAS) is modeled by a Laplacian function and the power delay spectrum (PDS) is modeled by a one-sided exponential decaying function as shown in Fig. 2.5.

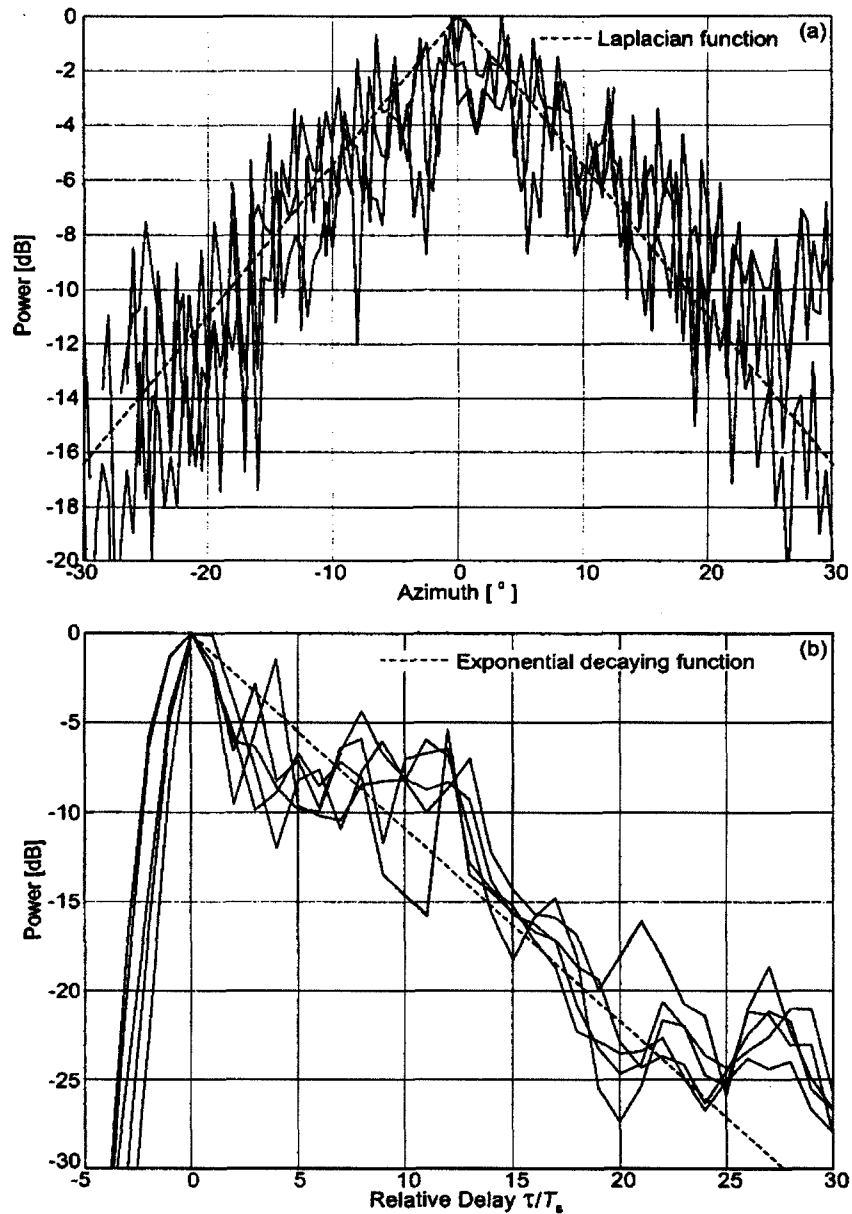


Fig. 2.5 Typical partial power spectra: (a) partial PAS at different delays, and (b) partial PDS at different azimuths ($T = 122$ ns) [2].

The literature review revealed that few experiments have been conducted for the development of channel models for microcells. A pioneer work of wideband

measurement and characterization of microcellular channels was reported in [21] at a carrier frequency of 910 MHz with a bandwidth of 20 MHz. The overall minimum rms delay spread computed for these channels was 61 ns, the average was 480 ns, and the maximum was 2940 ns. The paper concluded that multipath conditions are significantly less severe on microcellular-type than on conventional urban mobile radio channels, and that channel characteristics are independent of base station antenna height, so long as it is maintained lower building heights. Comparisons with measurements on macrocellular channels reported in the same paper showed that rms delay spreads are approximately 3.7 times lower in microcells than in macrocells.

Another microcell measurement experiment was done in an area with buildings more than 20 metres high in Paris, France. The measurement was performed at 2.2 GHz with 25 MHz bandwidth [22]. The rms delay spread in the LOS case was from about 10 ns to 170 ns, and in the NLOS case was from about 40 ns to 310 ns.

2.3 Quantification of Angular Dispersion on Multipath Channels

Spatial diversity is a technique that potentially increases the system capacity of wireless systems. Smart antennas and MIMO are promising technologies that use antenna arrays to mitigate the effects of multipath fading. In these systems, the angular distribution of received multipath components is important in determining the performance of the radio link. For example, if a smart antenna with beamforming is used, the beamwidth should be adjusted to the azimuth angular spread, so it can capture most of the power of the arriving waves. MIMO systems offer greater capacity when the correlation of received multipath components is lower, which generally occurs for a large set of multipath components with large angular spread. Hence, the angular spread is an important parameter for the description of the spatial characteristics on a radio channel. It should be also noted, however, that severe multipath, often referred to as “rich scattering” also generally accompanies low SNR, which decreases the channel capacity [23].

Angular dispersion determines the correlation between the output signals at spatially separated antennas and consequently the ability to mitigate fast fading by means of antenna diversity techniques. The spatial properties of the channel therefore have an enormous impact on the performance of antenna array systems and, hence, need to be

well characterized in order to make it possible to design efficient radio communication systems for the future.

Angular spread is a measure of how the arrival of received multipath components is distributed in space based on their AOAs and powers. In very dense multipath environments, multipath components arrive from different directions randomly with similar powers, as in typical urban NLOS scenarios, resulting in a large angular spread. On the contrary, the angular spread is small in LOS scenarios.

Experiments have shown that angular dispersion in microcell channels is totally different from that in conventional macrocells. In [2], reported measurements showed that in macrocell environments the received power is highly concentrated from the direction of the base station in the NLOS case, which indicates that a significant fraction of the received power propagates from the base station to mobile receivers via rooftop diffractions. It was found that the power azimuth spectrum can be modeled by a Laplacian function which is shown in Fig. 2.5.

Experiments in microcell environments in Paris were reported in [3]. Results showed totally different propagation mechanisms than those from macrocell environments [2].

The experiments were carried out with a channel sounder at 2.2 GHz with 12.5 MHz bandwidth and the receiver was equipped with a rotational virtual UCA. The beamforming algorithm was used to estimate the AOAs. Results showed that most received power was not coming from the base station as in the macrocell case, but from the street canyon in the general direction towards the transmitter in the NLOS case. There was always a dominant direction from which the waves with the greatest powers arrived. This was, for example, the direction to the BS in the LOS case, or the direction along a street canyon in the NLOS case. In the LOS case, the azimuth angular spread ranged from 3 to 30 degrees with the median at 7 degrees. In the NLOS case, the azimuth angular spread ranged from 5 to 120 degrees with the median at 20 degrees. The associated measurements were made in an area of irregular street patterns.

2.4 Consistency Intervals

The estimation of rms delay spreads and azimuth angular spreads from measured data should be derived from the temporal average of channel impulse response estimates. In order to obtain useful results, the averaging should be done over intervals where there are no significant changes of channel properties. Such intervals are herein referred to CIs.

Within CIs, CDFs for the power-weighted AOA, and power-weighted excess delay, of arriving waves remains almost constant, and channel variations are considered to be primarily the result of phase changes, over which it is standard practice to average radio propagation measurements.

To accurately characterize radio channels, it is desired to know the time evolution of radio channels. It was recognized by Bultitude, et. al [24] that simulations of time evolution are being done such that the channels of interest are assumed to be random and wide sense stationary (WSS), being characterized with the same stochastic parameters throughout the simulation time. However, this is contrary to the way in which real world channels evolve with time. Instead, fading and dispersive properties of mobile radio channels often change rapidly as the local environment of the mobile receiver changes. The work reported in [24] was a first attempt to identify when changes in measured channel characteristics take place, so simulators could be developed to produce channel characteristics that change in realistic fashion. Two other conference papers [25] [26] reporting similar analyses have also been presented. These three reports used a physics based approach in the analysis of measured data, but they reported different measures for the identification of change in the measured channel data. In their common approach, it was assumed that the statistics of channel variations would change

in response to changes in physical conditions on the measured channels. The above three reports were based on the analysis of continuous wave (CW) data from virtual antenna arrays to determine multipath angles of arrival. Uncertainties in these previous results are thus greater than those expected with the wideband data recorded during measurements with a real-world antenna array reported in this thesis.

In this thesis, a new method proposed by Bultitude [4] is used to estimate CIs. First, the AOA, relative power, and excess delay of each arriving wave are estimated using the UCA-ESPRIT algorithm. Secondly, the power-weighted ECDFs for multipath AOAs and their associated delays are formed. Third, these ECDFs are compared for consecutive time series measurements using a K-S test. It is well known that a K-S test can be used as the basis for a decision concerning whether or not two ECDFs for a random variable represent the same underlying random population. If the distance between two ECDFs exceeds a pre-determined critical value, it is considered that there has been a change in the channel characteristics. The detailed procedure of obtaining CIs is presented in Chapter 3.

This chapter has reported a review and evaluation of the most popular high-resolution AOA estimation algorithms, and reports the conclusion that the UCA-ESPRIT is the best

algorithm to apply for the application at hand. It also contains a review of some previous work concerning rms delay spread, angular spread, and CIs in microcells.

Chapter 3

Measurement System and Data Analysis Methods

3.1 Background

Radio channels can be represented as linear time-varying filters with additive noise at the output and can be characterized through knowledge of time series of their impulse response functions, $h(t, \tau)$ derived from propagation experiments. At a certain time t , a radio channel can be regarded as a linear time-invariant filter $h(\tau)$. A linear time-invariant filter can be characterized by its frequency transfer function in the frequency domain or its impulse response function in the time domain, which is the Fourier transform of its frequency transfer function. The impulse response $h(\tau)$ of a filter is defined as the output of the filter when the input signal is an impulse $\delta(\tau)$. Given the impulse response, the filter output $y(t)$ can be determined for any arbitrary input signal $x(t)$, and can be written as

$$y(t) = \int_{-\infty}^{\infty} x(\tau)h(t - \tau)d\tau = x(t) * h(t), \quad (3-1)$$

where $*$ denotes convolution.

The intuitive way to measure the impulse response of a radio channel is thus to transmit an impulse and record the output response. However, this is not practical because of the excessive bandwidth required and the exceptionally high peak power of a transmitter that would be required to transmit an impulse. An alternative called the pseudo-noise (PN) correlation method is mostly used to circumvent the transmitter peak power limitation. If the radio channel input has an auto-correlation function given by

$$R_{xx}(\tau) = \frac{1}{T} \int_0^T x(t)x(t+\tau)dt, \quad (3-2)$$

then the input/output cross-correlation function is given by

$$R_{xy}(\tau) = \frac{1}{T} \int_0^T y(t)x(t+\tau)dt = h(\tau) * R_{xx}(\tau). \quad (3-3)$$

If the input is white noise, which means $R_{xx}(\tau) = \delta(\tau)$, then

$$R_{xy}(\tau) = h(\tau) * R_{xx}(\tau) = h(\tau). \quad (3-4)$$

In other words, by transmitting a white noise signal, the impulse response can be obtained by cross-correlating the received signal with the transmitted signal. Instead of white noise, however, a PN sequence is often used for channel sounding because it is repeatable and yet, possesses most of the randomness properties of white noise. This results in good estimates of the channel impulse response function, with the accuracy of the estimate depending on transmission bandwidth and SNR conditions.

A PN signal is usually generated by a maximum length linear shift register of degree n ,

which is the number of consecutive registers. The length of the maximum length sequence is $2^n - 1$. The rectangular waveforms of maximum length shift register sequences can be considered as pseudo-random in the sense that they satisfy most randomness properties and their autocorrelation functions are similar to the autocorrelation of band limited noise. The CRC Chanprobe Channel Sounder, which is based on the PN correlation method, is discussed in the following section.

3.2 The CRC Chanprobe Channel Sounder

A channel sounder can be used to determine the time-variant impulse response of mobile radio channels. One such channel sounder called CRC-Chanprobe was built at CRC over the period during which the thesis project reported herein was conducted. The candidate participated in some redesign of the IF/baseband portions of the receiver, and calibration of the complete system, including the UCA used at the mobile receiver. The CRC-Chanprobe system consists of a transmitter mounted in a trailer and a receiver mounted in a minivan. All data recorded during experiments reported in this thesis were measured using CRC-Chanprobe. CRC-Chanprobe is based on the PN correlation method and a simplified block diagram of the transmitter and the receiver are shown in

Fig. 3.1 and Fig. 3.2, respectively.

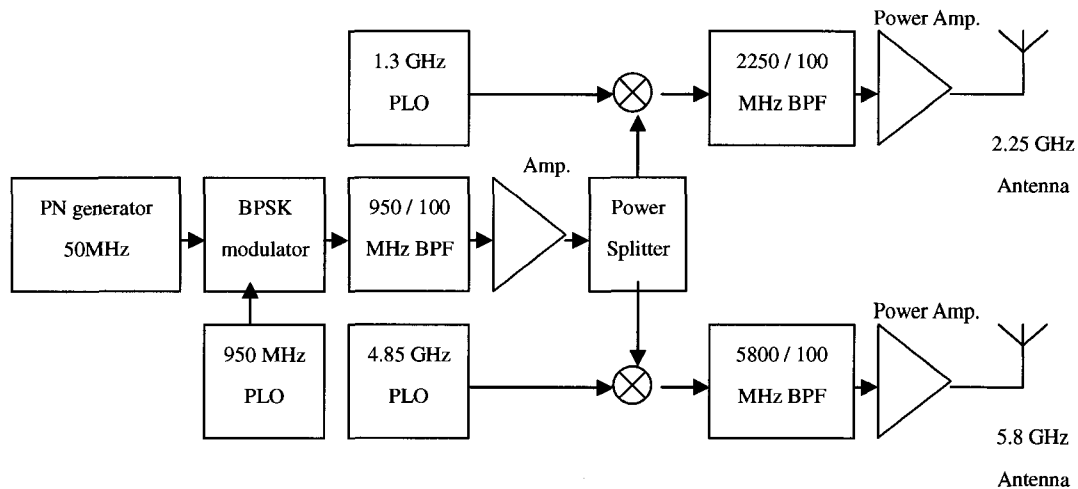


Fig. 3.1 Simplified block diagram of the CRC-Chanprobe transmitter.

At the channel sounder transmitter, a PN sequence with a length of 255 bits at 50 Mbps is modulated on a 950 MHz carrier using binary phase-shift keying (BPSK). A chip rate 50 Mbps was the maximum speed of the CRC-built PN generator available at the time the system was designed. This meant that the length of each bit was 20 ns, and because previous measurements [21] showed that maximum excess delays in microcells are shorter than $5 \mu\text{s}$, it was concluded that a sequence of 255 chips, giving a maximum excess delay of $5.1 \mu\text{s}$ was adequate. The use of sequences longer than necessary was avoided because of the need to sample voltages at all 32 elements of the receive array before the vehicle moved 0.01 wavelengths. Extra long sequence lengths would

therefore have meant that receive vehicle speed would be too slow for measurements in typical traffic densities on downtown streets. The modulator output is bandpass filtered, amplified, and split into two identical signals by a power splitter. The split signals are up converted to 2.25 GHz and 5.8 GHz by different mixers, bandpass filtered, amplified and radiated via suitable antennas. The transmitter can therefore simultaneously transmit a signal at both frequencies.

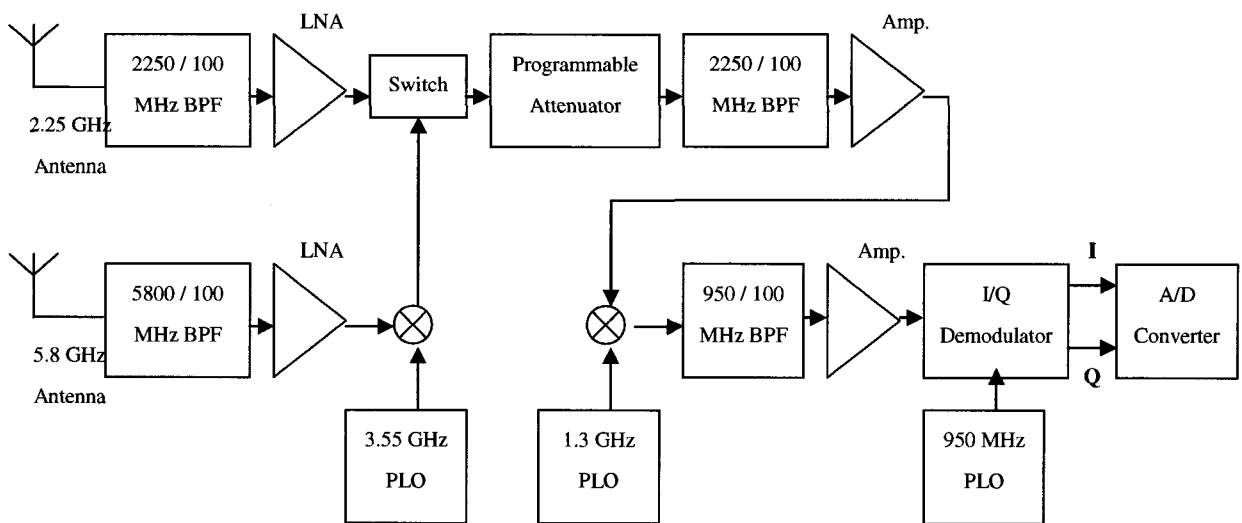


Fig. 3.2 Simplified block diagram of the CRC-Chanprobe receiver.

At the channel sounder receiver, the signals from both 2.25 GHz and 5.8GHz antennas are bandpass filtered and amplified by a low noise amplifier (LNA). Then the 5.8 GHz signal is down converted to 2.25 GHz and applied to an RF switch together with the 2.25 GHz signal. The switch is controlled by a computer and automatically switches to

alternately connect the two signals to the receiver IF stages. A programmable attenuator with 1 dB steps is also controlled by the computer. After an IF bandpass filter and amplifier, the signal is down converted to 950 MHz and applied to an I/Q demodulator. The I/Q signals at the output of this demodulator are sampled at a rate of 2 samples per bit of the PN sequence, and digitized in a 14 bit A/D converter. They are then temporarily stored in a 1 Gbyte RAM and transferred from there to the hard disk in specified portions of the data acquisition cycle during each measurement run. In this way, the length of a measurement run is made to be independent of the size of the RAM. The overall specifications of the CRC-Chanprobe channel sounder are shown in Table 3.1

The channel sounder is calibrated by a back-to-back test prior to the conduct of field measurements. A copy of the PN sequence is recorded by connecting the output of the transmitter through a suitable attenuator to the input of the receiver. Radio channel impulse response functions can then be estimated by cross-correlation of the signal received over the channel of interest with the back-to-back recording of the PN sequence. The auto-correlation of the signal received during a back-to-back test is shown in Fig. 3.3. In reality, the temporal resolution of the channel sounder is lower than the inverse bandwidth by a factor of approximately two, due to the width of the autocorrelation function.

Table 3.1 Specifications of the CRC-Chanprobe

Feature	Value
Centre Frequency	2.25 GHz, 5.8 GHz
RF Bandwidth	100 MHz
Tx Antennas	1 Monopole, 1 Biconical
Rx Antennas	1 Monopole, 1 Biconical Switched UCA (32 elements) Switched 3-D Array (31 elements)
Tx and Rx Antenna Polarizations	Vertical
Max RF Power to Tx Antenna	40 dBm
Receiver Dynamic Range	-65 dBm to -105 dBm
Chip Rate	50 Mchips/s
PN Sequence Length	127-1028
Receiver Noise Figure	3 dB

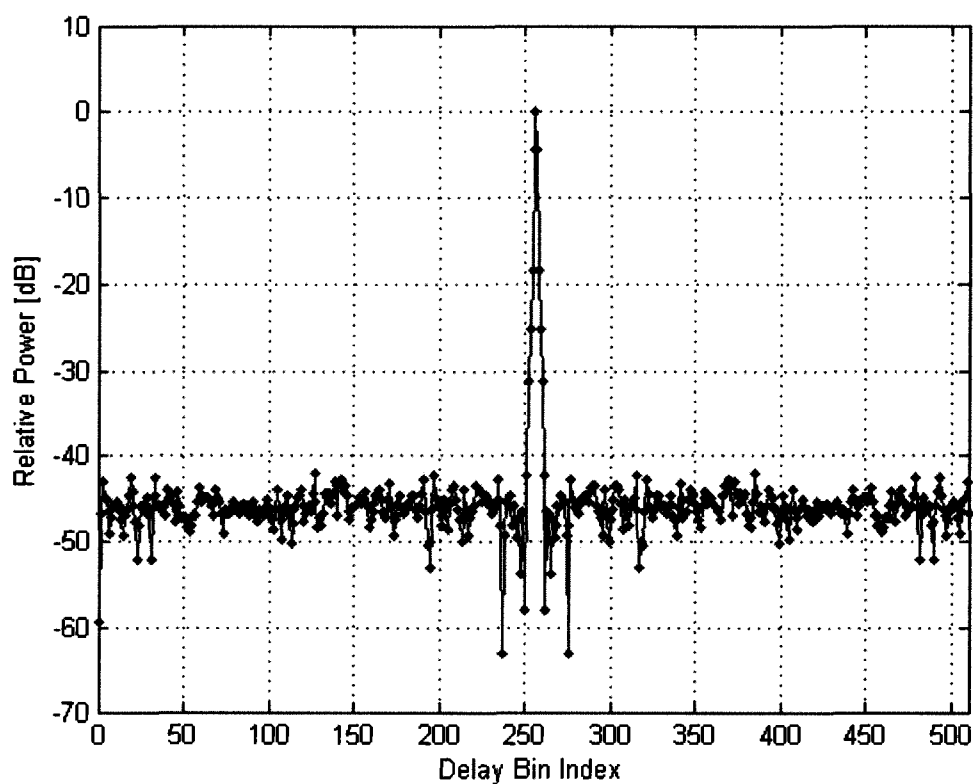


Fig. 3.3 Auto-correlation of the signal received during a back-to-back test.

3.3 The CRC-Chanprobe Switched UCA

The CRC-Chanprobe UCA consists of 32 antenna elements. Each element of the array is a quarter-wavelength drooping-radial monopole antenna. The UCA was employed with an impedance switching technique to minimize the effect of the mutual coupling. Its photograph is shown in Fig. 3.4. It has a radius of 0.25 metres. The idea of the

switched antenna array is to sample each antenna element in sequence. A 32:1 RF switch is used to connect all 32 elements to the input of the receiver and is controlled by a data collection system. The impedance switch is used to connect each antenna element either to the RF switch or to a complex termination impedance of $j250$ ohms. When one element is being sampled (active element), the others are switched to the complex termination impedance (passive elements). Using this method, the mutual coupling is suppressed. Details of the impedance switching technique and coupled-element input impedances are presented in [8].



Fig. 3.4 The CRC-Chanprobe switched UCA.

3.4 Measurement Set-up and Data Analysis Methods

As outlined above, the CRC-Chanprobe measurement system is a 100 MHz wideband system operating at 2.25 GHz. The time domain resolution of the measurement system is 10 ns. Since radio waves travel 3 metres in 10 ns this measurement system can resolve two arriving waves whose traveling distances are different by more than 3 metres. The length of the whole PN sequence is 5100 ns, so the maximum unambiguous measurement range would be about 15 km, were it not for SNR constraints. Since the ratio of the peak of an impulse response estimate to its side-lobe plus noise power should be greater than 20 dB for channel characterization applications, in practice, the system's operating range is limited to about two city blocks. The value of 20 dB has conventionally been chosen over the years for outdoor propagation experiments, as a compromise among several parameters, including transmit range, unambiguous delay range, SNR, and operating bandwidth. During experiments reported in this thesis, the receive UCA was mounted on the roof of a minivan at height of 2.3 metres. The transmit antenna was mounted on a mast extended from a trailer or a stationary minivan at height between 4 and 7 metres, depending on experimental requirements. During the experiments, the trailer that housed the transmitter was parked in an arbitrarily selected position at curb side on moderately busy streets in downtown Ottawa. The minivan that

housed the receiver was driven at a fairly constant, but slow speed on streets that were mostly within two city blocks of the transmitter.

Since all receive antenna elements are sampled in sequence and the antenna array is moving, the elements, except the first one, are actually sampled at different positions from that at which they are expected to be. In other words, the prior spatial knowledge of the array is not correct anymore and the estimation algorithms depending on this knowledge will fail. In [26], which reports previous work at CRC, simulations show a maximum travel distance of 0.01λ keeps the estimation error at a sufficiently low level. During experiments with the switched UCA, the length of the sampled sequence at each element is 600 bits at 100 MHz. This length is a little longer than the length of the PN sequence, which is 510 samples (PN sequence of 255 bits with 2 samples per bit), because the switching between the elements causes a short unstable period. The bit period is 20 ns (50 Mbps) and the sampling duration for one antenna element is thus $6\ \mu s$. Hence, the sampling time for one snapshot (sampling 32 elements) is $192\ \mu s$. With a maximum allowable travel distance of 0.01λ and a carrier frequency of 2.25 GHz, the maximum allowable speed of the vehicle is given as

$$v_{\max} = \frac{0.01 \times 0.1333(m)}{192(\mu s)} = 6.94(m/s) = 25(kph). \quad (3-5)$$

Therefore, the speed of the minivan must be less than 25 kph in order to obtain reasonably accurate estimates of multipath AOAs.

There are also other uncertainties that could lower the accuracy of the measurement results. One is that the radiation patterns of antenna elements were assumed to be isotropic, but in practice were only almost omni-directional, and probably varied from one element to another. Another is that the heading of the receive minivan almost certainly varied randomly by a small amount from nominal during each trajectory. A third is that, arriving waves with elevation angles less than 0 degree, for example the ground wave, might only impinge on some antenna elements on the portion of the UCA in the direction of the arriving waves. A fourth source of errors is that some waves impinging on the array from nearby interacting objects might not be plane waves, violating the plane wave assumption used in the development of the array processing algorithms. Despite these uncertainties, calibration results, reported later, show that resolution and accuracy were such as to be considered adequate to meet the objectives of the project.

The following sections describe how the data collected from the experiments were processed and analyzed. When the CRC-Chanprobe system is running, the output of the

analog to digital (A/D) converter is recorded on the hard disk of a personal computer. After the experiments have been completed, these binary data of both I and Q are read and converted to complex voltages by a MATLAB program. The data collection system at the receiver was time triggered and the data sampled from all 32 elements were recorded in one data block as show in Fig. 3.5.

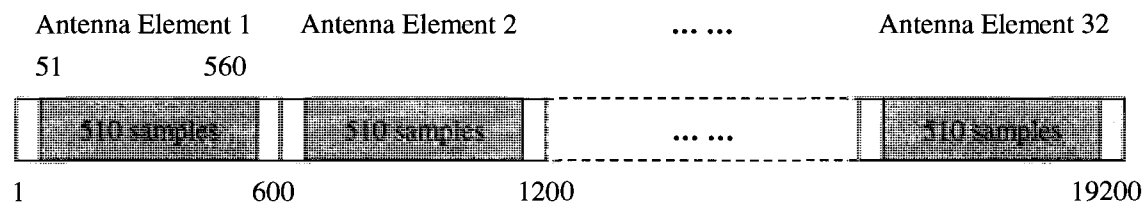


Fig. 3.5 Structure of one data block recorded at the receiver.

At the transmitter, a 50 MHz PN sequence of 255 chips in length was BPSK modulated on a carrier at 2.25 GHz, so the transmitted RF bandwidth is 100 MHz. The transmitting power is 30 dBm from a quarter-wavelength monopole antenna. The receiver recorded 2 samples per chip, so the received PN sequence is 510 samples long. Because the switching between the elements causes a short unstable period, 600 samples were recorded at the receiver, and 510 samples from 51st to 560th were chosen as a sample window for processing. The number of data blocks sampled in one second varies from 200 to 400 depending on experimental objectives. For each antenna element, the mean

value of the complex voltage is subtracted, and the phase is adjusted according to the associated feed system phase offset value obtained from calibration measurements. After that, there is no DC offset in the received signal and the effective phase shifts in the transmission line connections to all 32 antenna elements are the same. After all sample windows of length 510 are aligned and cross-correlated with the local reference signal, impulse response estimates can be obtained.

Parameters of delay spread can be determined from APDPs, which are temporal or spatial averages of the squared moduli of consecutive impulse response estimates, herein referred to as instantaneous power delay profiles (IPDP). An APDP is sometimes herein also referred to as power density spectrum. For the examples in this section, each APDP is obtained by two steps. First, the IPDPs of 32 antenna elements in one snapshot are averaged. Second, the results of 10 consecutive snapshots are averaged, because the number of arriving waves in each delay resolution interval is less than 10 in most cases (this conclusion was obtained by trying different number of snapshots, including 5, 10, 15, and 20, in the AOA estimation algorithm). Fig. 3.6 shows an example of the APDP from a LOS measurement using a log scale. Each dot presents one delay bin.

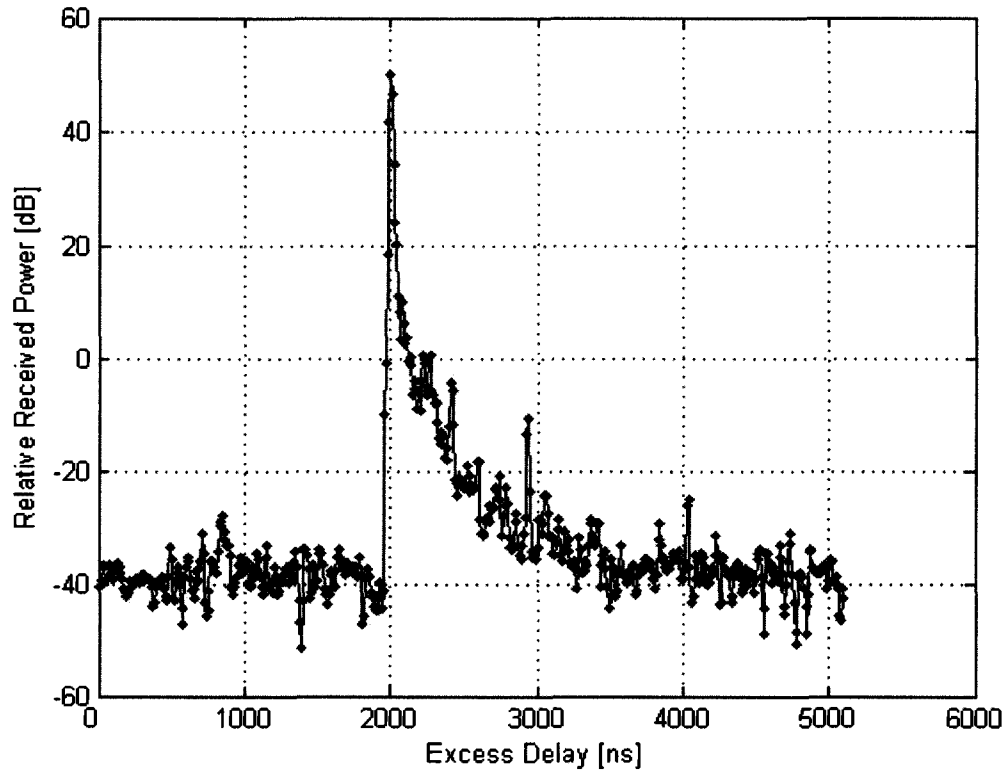


Fig. 3.6 Average power delay profile (APDP).

To study the radio channel, one needs to analyze APDPs estimated from all data recorded during an experiment. Fig. 3.7 shows a consecutive record of 250 APDPs (2500 snapshots) in 10 seconds from a LOS case. This figure is the pseudo-color plot of the relative received power of the impulse response estimate series, so the color in the figure represents the power. The red color shows the signals with strong power and the blue color shows the background noise. In each APDP, there is only one strong signal and it always arrives before other signals, which shows a strong signal with the shortest

distance to the transmitter (LOS signal). As time advances, the LOS signal arrives a little bit later at a constant rate, because the red line is rather straight. This shows the receiver was moving away from the transmitter at almost constant speed. The LOS signal at 10 seconds is seen to arrive 220 ns later than that it does at 0 seconds in Fig. 3.7. Since radio waves travel 66 metres in 220 ns, and the vehicle moves 66 metres in 10 seconds the speed of the receive vehicle during this recording was about 24 kph.

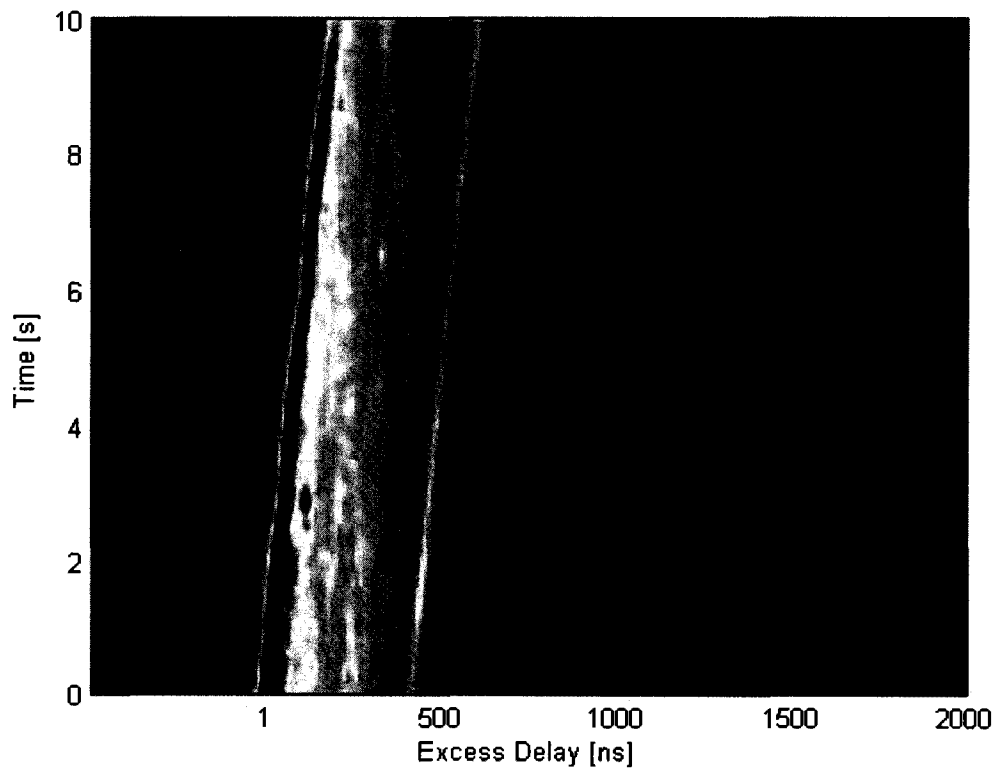


Fig. 3.7 Time series of APDPs for a LOS case.

For comparison with the LOS case, Fig. 3.8 shows similar results for a NLOS case. One can see that there was more than one strong signal in every APDP and the strongest signal did not arrive first. Since the channel properties of the LOS case and the NLOS case are so different, these two cases are usually analyzed separately.

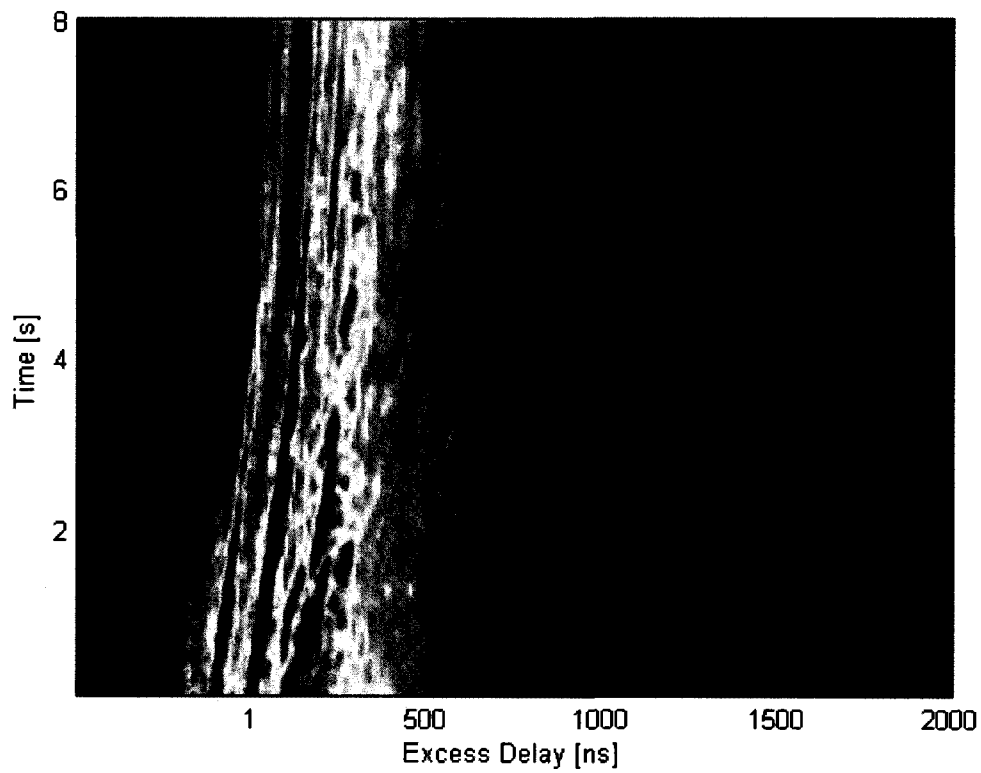


Fig. 3.8 Time series of APDPs for a NLOS case.

3.4.1 Estimation of RMS Delay Spread

The mean excess delay, rms delay spread, and maximum excess delay on a radio channel are used to describe multipath dispersion on the channel, and can be estimated from the channel's APDPs. An example of these parameters is shown in Fig. 3.9. They are processed with respect to a power threshold to avoid the influence of unwanted noise at long delays. In this thesis, the threshold was chosen as 20 dB below the peak power.

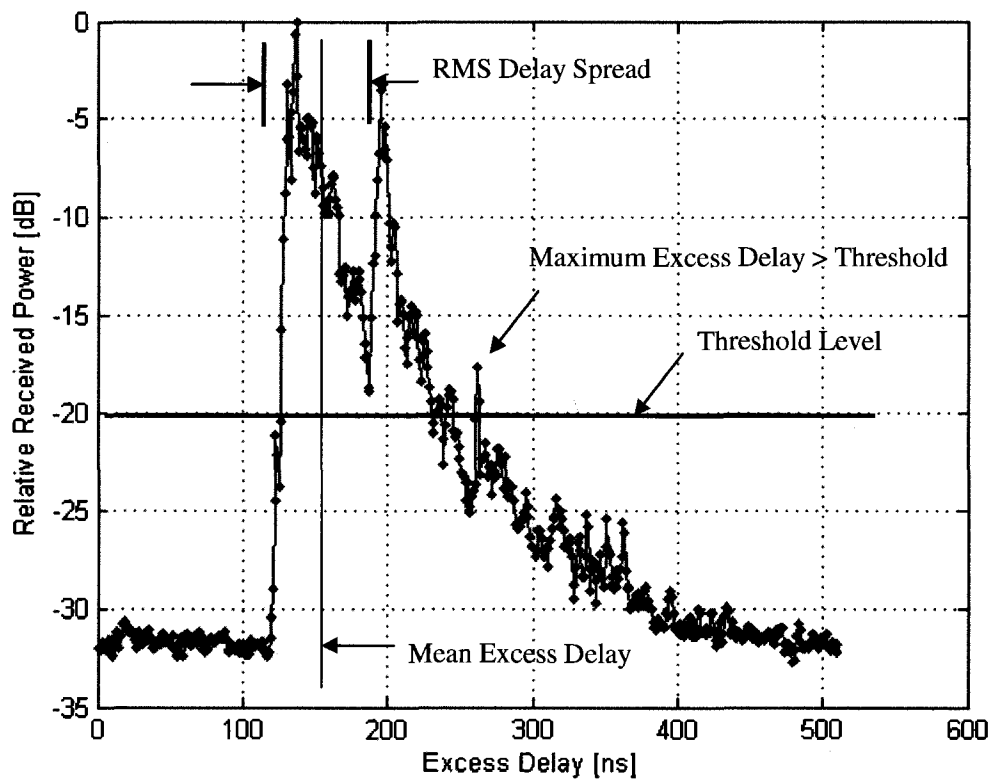


Fig. 3.9 Example of an APDP and parameters of a channel's multipath spread.

The maximum excess delay is the time period during which multipath signals with significant energy arrive. The mean excess delay is the power-weighted average of the delays contributing to the APDP [27], and can be written as,

$$\bar{\tau} = \frac{\sum_n P(\tau_n)\tau_n}{\sum_n P(\tau_n)}. \quad (3-6)$$

The rms delay spread is the power-weighted standard deviation of excess delays, which is the square root of the second central moment of the power delay profile and is defined as [27]

$$\begin{aligned} \sigma_\tau &= \sqrt{\tau^2 - (\bar{\tau})^2} \\ &= \sqrt{\frac{\sum_n P(\tau_n)\tau_n^2}{\sum_n P(\tau_n)} - (\bar{\tau})^2}. \end{aligned} \quad (3-7)$$

In this thesis, the APDP used to calculate rms delay spread is obtained by two steps. First, the IPDPs of 32 antenna elements in one snapshot are averaged. Second, the previous results of a certain number of snapshots are averaged. APDPs reported herein are therefore both spatial and temporal average of impulse response estimates. An APDP is obtained by averaging the impulse response estimates over time, but the arrival time of each impulse response estimate is different as shown in Fig. 3.7 and 3.8. Therefore, one needs to align these estimates. There are several ways to do this. One

can align them with the first noticeable signal, which is the first signal whose power exceeds a certain threshold above the noise floor. One can align them with the peak power signal in the LOS case, because the strongest signal always arrives first in the LOS case. In this thesis, however, impulse response estimates are aligned at their centroids, since this is where a receiver with a phase locked loop would synchronize to communications signals transmitted over the measured channels [28]. The centroid is the power-weighted mean delay of an impulse response estimate, and is given by

$$\tau_{centroid} = \frac{\sum P(\tau_n)\tau_n}{\sum_n P(\tau_n)}. \quad (3-8)$$

After the impulse response estimates are aligned, the APDP can be obtained and the rms delay spread can be calculated.

3.4.2 Estimation of AOAs

In Chapter 2, it was reported that it has been chosen to employ UCA-ESPRIT as the array processing algorithm used for AOA estimation in this thesis project. Multiple snapshots are imperative to UCA-ESPRIT. One snapshot consists of complex voltage samples of 32 antenna elements at the same delay. Multiple snapshots are those sampled over time, so it is important that these impulse responses are accurately aligned. In this thesis

project, the number of the snapshots is chosen to 10 for the following two reasons. First, the number of arriving waves in each delay resolution interval is less than 10 in most cases, so this meets the requirement of the UCA-ESPRIT to have covariance matrices of appropriate rank to estimate the parameters of all arriving waves. Second, it is not necessary to align the impulse responses in this time interval, as demonstrated in the following. The time between the 2 samples (i.e. two dots in Fig. 3.6) is 10 ns. Radio waves travel 3 metres in 10 ns. If 250 data blocks are recorded in one second, the time to record 10 snapshots is 0.04 second. Thus, the time difference of arriving waves of 10 snapshots would be within the resolution of the CRC Chanprobe system if the vehicle speed is less than 75 m/s, which is much larger than the vehicle speed (5–7 m/s) used in urban experiments. Therefore, it is safe to average the 10 consecutive snapshots without alignment.

A relative power threshold is chosen to obtain the time interval of signals with significant power in each impulse response estimate. The time interval is chosen from the first delay bin whose power exceeds the threshold to the last delay bin whose power exceeds the threshold. For example, if the threshold is chosen as -20 dB as shown in Fig. 3.9, this time interval would be from 1960 ns to 2940 ns, which is from delay bin 196 to delay bin 294. Data in all the delay bins within this time interval are processed by

UCA-ESPRIT. In this thesis project, all multipath signals with relative powers greater than 15 dB or 20 dB down with respect to the peak power of IPDPs are retained, depending on the data being analyzed.

After the UCA-ESPRIT algorithm is applied to process data at all selected delays, the azimuth angles, elevation angles, and relative power of multipath signals in each delay bin are estimated and paired. Fig. 3.3 shows the auto-correlation function of the back-to-back test, which is the impulse response that would be obtained if there was only one arriving wave. Notice that not only the delay bin with the peak power (delay bin 256) contains the information of the arriving wave, but also the delay bins (252 to 260) contain that information. With the threshold of 20 dB down to the peak power, two adjacent delay bins (255 and 257) would provide duplicate estimates of angle of arrivals with significant power. Therefore, one needs to exclude duplicate estimates. In this thesis, every estimate of azimuth angle of each delay bin is compared with estimates of azimuth angles of adjacent delay bins. If the difference between the azimuth angles of two estimates is less than 3 degrees, which is about half the angular resolution of the measurement system, the estimate with lower estimated power is excluded.

3.4.3 Estimation of Azimuth Angular Spread

In this thesis, only the azimuth angular spread is processed and analyzed because the estimation of elevation angles is not accurate, as shown in the calibration tests discussed in section 3.5.

The angular spread is defined based on an assumption of super-resolution as [29]

$$\sigma_{AS} = \min_{\Delta} \sigma_{AS}(\Delta) = \sqrt{\frac{\sum_{m=1}^M (\theta_{m,\mu}(\Delta))^2 \cdot P_m}{\sum_{m=1}^M P_m}}, \quad (3-9)$$

where P_m is the power of the m th multipath signal and $\theta_{m,\mu}(\Delta)$ is defined as

$$\theta_{m,\mu}(\Delta) = \begin{cases} 2\pi + (\theta_m(\Delta) - \mu_{\theta}(\Delta)), & (\theta_m(\Delta) - \mu_{\theta}(\Delta)) < -\pi \\ (\theta_m(\Delta) - \mu_{\theta}(\Delta)), & |\theta_m(\Delta) - \mu_{\theta}(\Delta)| \leq \pi \\ 2\pi - (\theta_m(\Delta) - \mu_{\theta}(\Delta)), & (\theta_m(\Delta) - \mu_{\theta}(\Delta)) > \pi \end{cases},$$

$$\text{where } \mu_{\theta}(\Delta) = \frac{\sum_{m=1}^M \theta_m(\Delta) \cdot P_m}{\sum_{m=1}^M P_m},$$

and $\theta_m(\Delta) = \theta_m + \Delta$, where θ_m is an AOA estimated from the measurement data.

This definition will not give correct results if the azimuth angles are mainly from directions close to 0 degrees, or 360 degrees. In the circular azimuth diagram, the azimuth angle rotating from 360 degrees to 1 degree is linear, but there is a 359 degree

change in the degree dimension. In this situation, the power weighted mean of the azimuth angles $\mu_\theta(\Delta)$ would be around 180 degrees, and the resultant angular spread would be larger than it should be. The method used to compensate for this in work reported in this thesis is by adding 180 degrees to each azimuth angle estimate and then calculate the angular spread from the new values, in cases where the azimuth angles are mainly from directions close to 0 degrees.

3.4.4 Estimation of Consistency Intervals

Intervals between significant changes on radio channels are herein referred to as CIs [4]. These are believed to be the intervals over which measurements should be averaged to estimate rms delay spreads and angular spreads. Results averaged over such intervals are reported for the first time herein, whereas results previously reported are from averages over a variety of arbitrarily chosen intervals, such as one second, or a frame interval proposed for use in the anticipated future mobile radio system. In this section, a method using K-S tests to obtain the CIs, as proposed by Bultitude [4] is described. The K-S test is used to determine if two ECDFs represent the same random population based on the analysis of a finite number of samples. In this section, the results of UCA-ESPRIT applied to sets of 30 groups of data recorded during 10 measurement

snapshots is used to estimate power-weighted ECDFs for the angles of arrival and excess delays of multipath signals. For convenience, 10 consecutive snapshots is called a group. Group 1 consists of snapshots 1 to 10, and group 2 consists of snapshots 2 to 11. All groups are obtained according to this rule, like a 10 snapshot length sliding window. A set of 30 consecutive groups is called a set. Set 1 consists of groups 1 to 30, and set 2 consists of groups 2 to 31. All sets are formed according to this rule. There are two parameters, AOAs and excess delays, that are considered to estimate CIs.

For the estimation of CIs using only AOAs, a PAS is generated for each group and a power-weighted experimentally-determined probability density function (EPDF) is estimated for each set from 30 groups of generated PAS. The areas of these EPDFs are then normalized and the results are integrated to yield ECDFs for AOAs. Each ECDF corresponds to one set.

For the estimation of CIs using knowledge of only excess delays, a PDS is generated for each group, and all such spectra are aligned with respect to their centroids. A power-weighted EPDF is then estimated from a set of 30 aligned groups. The areas of these EPDFs are then normalized and the results are integrated to yield ECDFs for excess delays.

After the ECDFs for power-weighted AOAs and excess delays are estimated as above, one must estimate the critical values for use in K-S tests for the comparison of consecutive ECDFs. Under the reasonable assumption that there would be no changes in the channel characteristics for nearest-neighbor parameter estimates, which are derived from data recorded in closely spaced overlapping intervals along the street, the critical values are taken as the maxima (exemplified in Fig. 3.10) of the ECDF distances between nearest neighbors for each measurement run. It is considered that choosing values that are less than this could result in false declaration of changes as a result of estimation errors and equipment effects, whereas choosing values that are greater than this could result in CIs that span some channel changes, while, for the purpose of defining averaging intervals, conservative estimates of CI lengths are considered adequate. The so-estimated critical values change somewhat from measurement run to measurement run. This could be the result of traffic effects, changes in direction, impulsive noise, and the like. For this reason, the critical value for each run is only applied in processing data from that run. If the distance at the 95th percentile of nearest-neighbor ECDFs is taken as the desired critical value, there is only 5% probability that a rejection of the hypothesis that two ECDFs under comparison represent the same population of AOAs or delays would be incorrect. In this thesis, however, critical values were chosen as the 100th percentiles of nearest neighbor distance ECDFs, since the results from this were found to

reveal patterns in CIs that might, in future work, allow association of results with the physical environment.

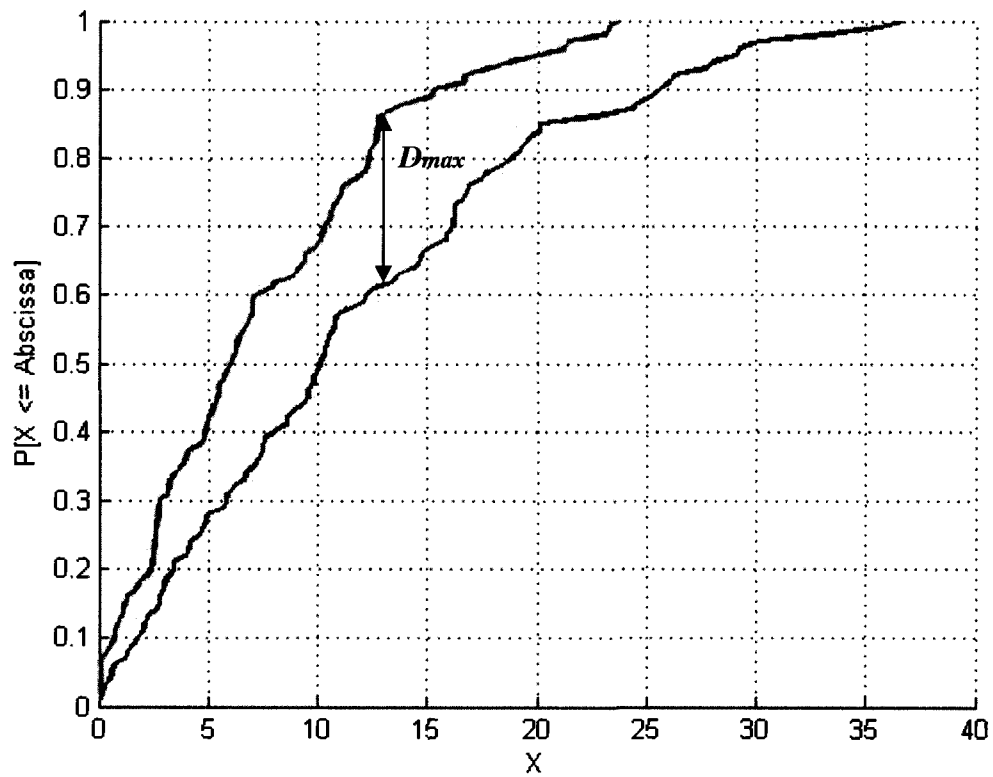


Fig. 3.10 Maximum distance (D_{max}) between two ECDFs.

Once the critical values are determined, a search for CIs is carried out in both forward and reverse directions. The reference set is chosen to be 100 in the beginning, and increments 1 each time. To determine the beginning of a CI about a reference set, the ECDF of the reference set is compared with ECDFs of consecutive sets with lower

indices in the time series until the distance between the compared ECDFs is greater than the critical value. To determine the end of a CI about this reference set, the ECDF of the reference set is compared with ECDFs of consecutive sets with greater indices in the time series until the distance between the compared ECDFs is greater than the critical value. Then, a CI is determined and used to calculate the rms delay spread and the angular spread. The lesser of the CIs for AOA and excess delays in both directions with respect to the reference set is chosen as the CI for use in further analyses.

3.5 Calibration Tests

Experiments for determination of the accuracy and resolution of AOAs estimated using the UCA and post processing using UCA-RB-MUSIC were conducted. These were conducted before it was found that processing speeds are unacceptably slow with this algorithm, and the change to UCA ESPRIT as the algorithm of choice for use in this thesis. However, it is considered that similar results would also be obtained using UCA-ESPRIT.

3.5.1. The Accuracy of AOA Estimation

Experiments were carried out at the entrance to the CRC reserve on October 26th, 2006, where there was a large open area free of obstacles between the transmit antenna and the receive antenna as shown in Fig. 3.11. Thus, the first arriving impulse response peak should have been significantly contributed to by the LOS wave. The solid line indicates the trajectory of the mobile receive antenna array and was 60 metres in length. The transmit antenna was placed along the dotted line at distances of 50, 40, 30, 20, and 10 metres from the receiver's trajectory. The dotted line along which the transmitter was positioned intersected the receiver's trajectory at its centre, and was perpendicular to it (i.e. it was a right bisector of the receiver's trajectory). The transmit antenna was mounted on a mast extended from the rear of a stationary minivan at height of 6.5 metres and the receive UCA was mounted on the roof of a moving minivan at height of 2.3 metres.

Since the delay bin of peak power contains the information of the LOS signal from the transmitter, the complex voltages of delay bins having peak power of 10 consecutive impulse response estimates were passed as snapshots to UCA-RB-MUSIC algorithm to estimate the azimuth and elevation angles. There were 250 data blocks sampled in one second, and 10 consecutive data blocks from every 500 data blocks were processed by

UCA-RB-MUSIC.



Fig. 3.11 Satellite photograph of the area where the calibration test was made.

The experimental set-up is shown in Fig. 3.12, and the AOA configuration of the UCA depended on whether the receiver was moving from Northeast (NE) to Southwest (SW) or from SW to NE. The distance between the transmit antenna and the receive antenna is denoted by dI . The angle between the transmit antenna and the direction of the moving receiver is denoted by φ , which should be correctly estimated. The minivan

was moving at an almost constant speed having a value between 5 and 7 kph (neither distance nor speed was recorded during the experiments, and the ground was not level).

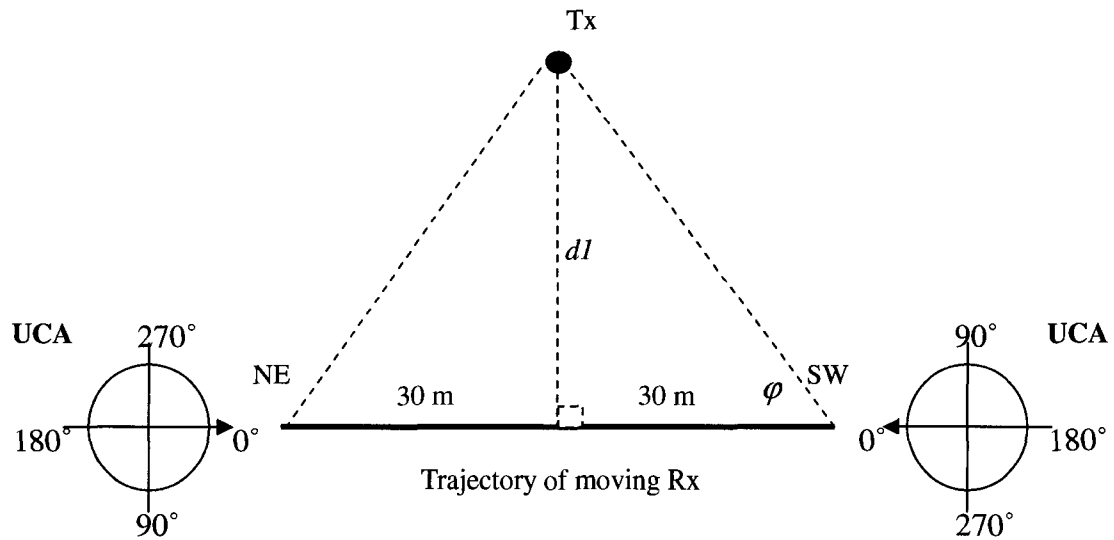


Fig. 3.12 Measurement set-up of the accuracy experiment.

The geometry of the azimuth and elevation angle is shown in Fig. 3.13, where φ denotes the azimuth angle and θ denotes the elevation angle.

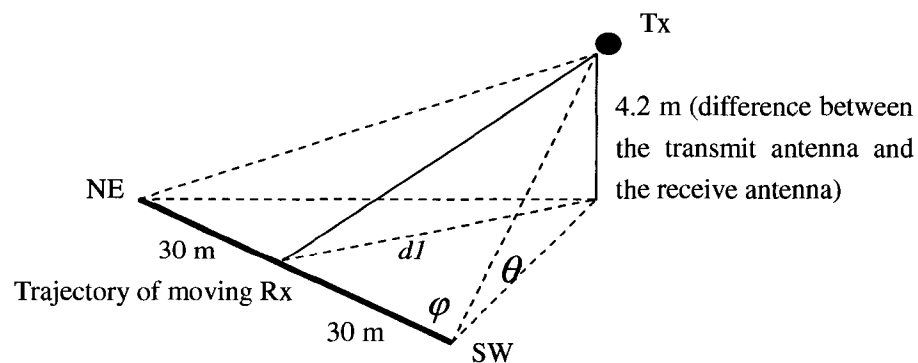


Fig. 3.13 Geometry of the azimuth and elevation angle.

One example of AOA estimation results when d_l was 50 metres are shown in Fig. 3.14. The dots in the figures show the estimated azimuth angles (a) and elevation angles (b) along the trajectory, and the sizes of dots correspond to relative received power. The lines are expected results calculated from the geometry with the assumption that the moving receiver was moving at a constant speed, for the total measurement time.

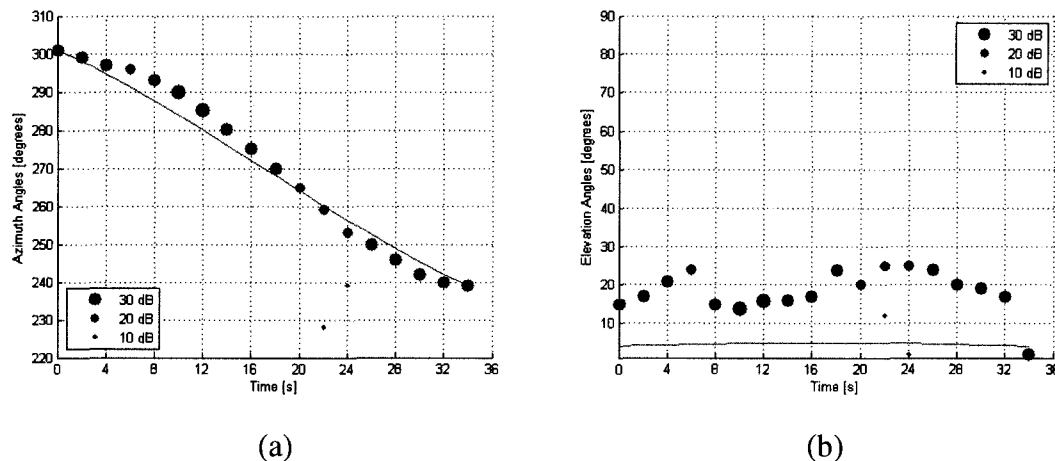


Fig. 3.14 Azimuth (a) and elevation (b) angles estimates.

The estimated azimuth angles at the beginning and the end exactly match the expected values in Fig. 3.14 (a), but slightly deviate along the trajectory, which could be the result of inconstant vehicle speed. The mean value and standard deviation of the errors of azimuth angles estimates in this measurement run are 2.75 and 1.78 degrees, respectively. The estimated elevation angles are much higher than the expected values in Fig. 3.14 (b). It is believed that the errors in these estimates of elevation angles are large because of the

narrow extent of the array aperture in the elevation plane, leading to a broad inherent beamwidth for the array in this plane, being that of a single monopole element.

Other experiments were done when the transmitter was at different locations and the receiver was driving towards different directions. The results were consistent, which is that estimates of azimuth angles with UCA are very good and estimates of elevation angles are poor.

3.5.2. The Resolution of AOA Estimation

Experiments were carried out on the CRC reserve as shown in Fig. 3.15. The two yellow dots represent the approximate positions of two transmit antennas. The height of these two antennas was 4.6 metres and they transmitted the same power. These experiments were designed to determine the resolution of azimuth angles at the same elevation angle. The configuration of the experiment was the same as for the previous experiments.

The measurement set-up is shown in Fig. 3.16. There were 250 data blocks sampled in one second, and 10 consecutive data blocks from every 100 data blocks were processed

by UCA-RB-MUSIC. Measurements were made at different distances d_2 , and the relationship between γ and d_2 according to the geometry is shown in Table 3.2.



Fig. 3.15 Satellite photograph of the area where the calibration test was made.

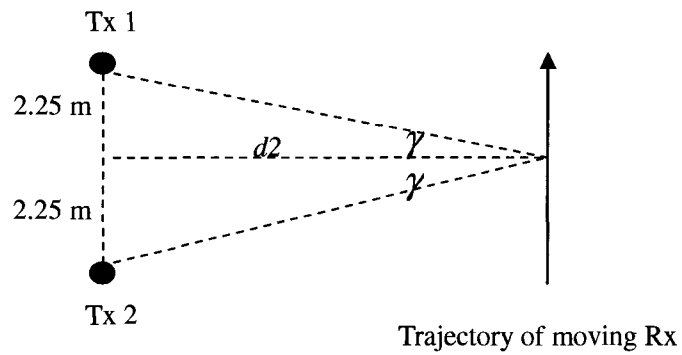
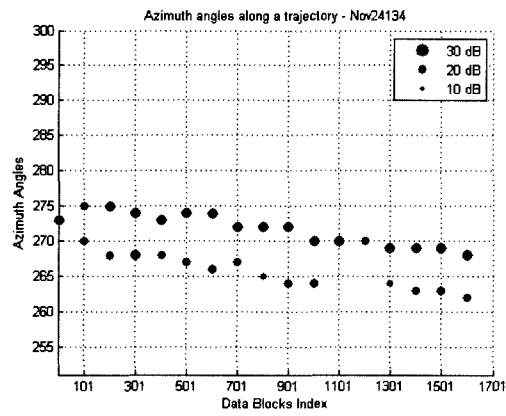


Fig. 3.16 Measurement set-up of the resolution experiment.

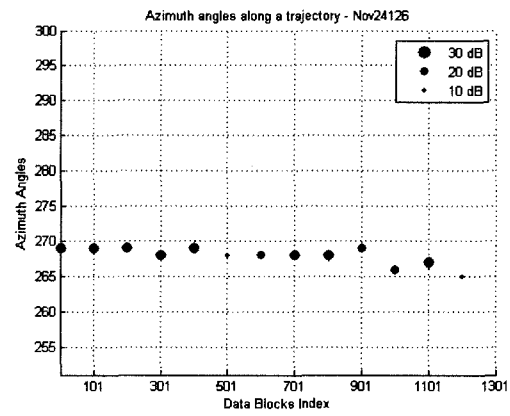
Table 3.2 Relationship between the resolution and the distance

γ	2γ (resolution)	$d2$
4°	8°	32.2 m
3°	6°	42.9 m
2.5°	5°	51.5 m

Estimates of azimuth angles when $d2$ was 32.2 metres and 42.9 metres are shown in Fig. 3.17. From the figures, we can see that the UCA resolved the azimuth angles at the distance 32.2 metres (a), but did not resolve the azimuth angles at the distance 42.9 metres (b). Therefore, the resolution of the UCA is concluded to be between 6 and 8 degrees.



(a)



(b)

Fig. 3.17 Azimuth angles estimates of $d = 32.2$ m (a) and $d = 42.9$ m (b).

Chapter 4

Measurement and Analysis Results

Radio propagation experiments were conducted in downtown Ottawa on April 11th, 2007. This area is a typical North American downtown area, which has rectangular street grids with high buildings of around 80 metres in height. This is markedly different than a typical European downtown area with irregular street patterns and lower buildings. Fig. 4.1 shows a satellite photo of the area where the experiments were carried out. The flag indicates the location of the transmitter. The yellow lines indicate routes where the receiver was in NLOS conditions and the blue line indicates the route where the receiver was in LOS conditions. The green lines represent experimental runs and the arrows indicate directions of movement. Only experiments that resulted in impulse response estimates with a minimum 20 dB between their peak powers and their noise floors were included for analysis results reported in this section. All experimental runs are grouped into three categories according to their physical environments:

- **LOS**: A1, A2, A3, and A4.
- **NLOS perpendicular** (to the street where the transmitter was located): B5, B8, B17, B18, B20, and B21.

- **NLOS parallel** (to the street where the transmitter was located): C16, C22, C27, and C28.

The transmit antenna was a quarter-wavelength monopole mounted on a trailer at a height of about 5 metres above the ground. The trailer was parked at curb side on the street. The receive UCA was mounted on a minivan at a height of 2.3 metres and the minivan moved at a speed between 10 kph and 20 kph. The measurements were taken at 250 snapshots per second and the carrier frequency was 2.25 GHz.

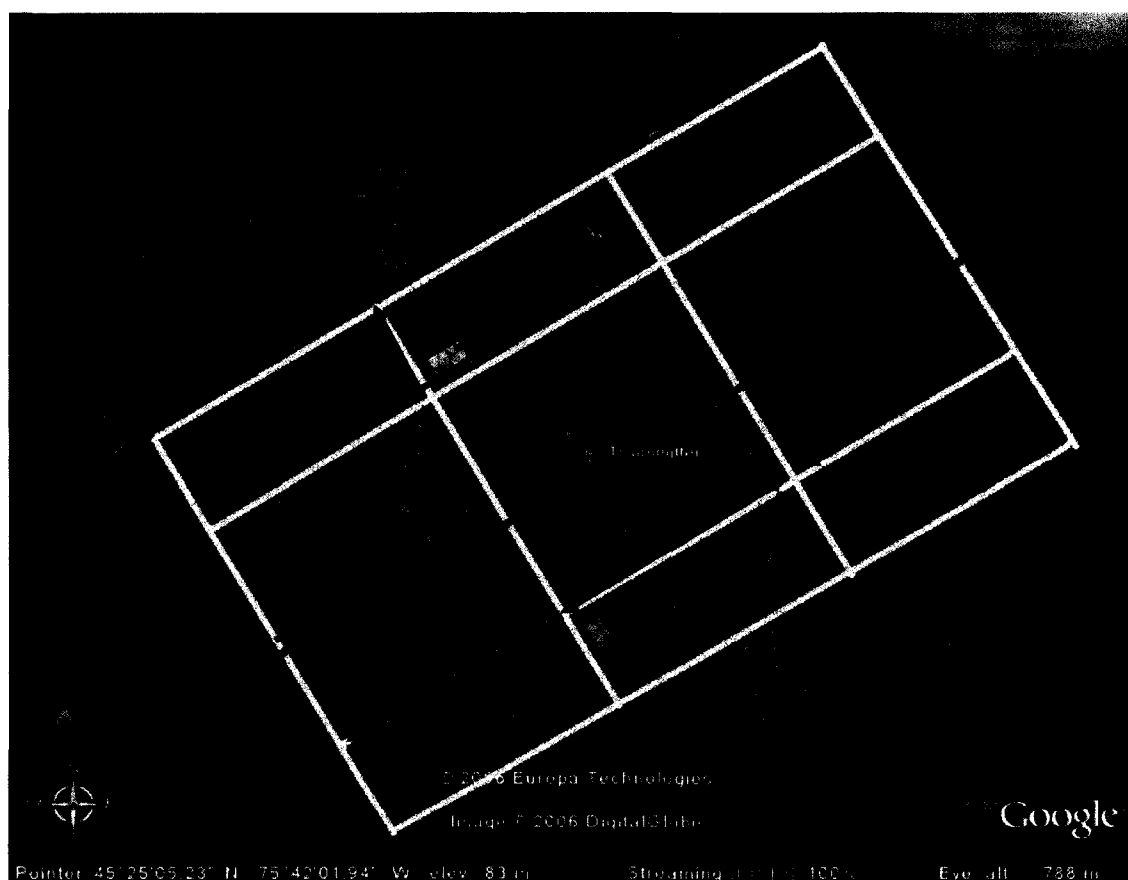


Fig. 4.1 A satellite photo of downtown Ottawa where radio propagation experiments were carried out.

4.1 Study of AOAs

In this section, the data were processed according to methods described in Section 3.4.2. The pseudo-color plots of time series of estimated AOAs in azimuth for measurement runs along streets in the three categories are shown in Fig. 4.2 (LOS), Fig. 4.3 (NLOS perpendicular), and Fig. 4.4 (NLOS parallel) respectively. The colors show relative received power in dB of the multipath wave received at each AOA in azimuth.

The figures in Fig. 4.2, which are results from LOS scenarios, show that most of the AOAs were in the direction to the transmit antenna, and the azimuth angular spreads were very small. The figures in Fig. 4.3 and Fig. 4.4, which are results from NLOS scenarios, show that most of the AOAs were in the direction towards the nearest opening to the street on which the transmitter was located. However, the azimuth angular spreads were much greater than those of the LOS scenarios. Fig 4.3 (e) shows a group of AOAs corresponding to multipath components with high relative powers that persisted throughout the whole measurement run because there was a big parking lot between the receiver and the transmitter. Fig 4.3 (d) and Fig. 4.4 (a) (b) (d) show more groups of AOAs because there were waves with significant energy propagating through gaps between buildings. These observations match conclusions reported in [3]. Future

work could be done to relate the groups of AOAs to the physical environment, so one can determine the scattering, reflection and diffraction mechanisms that prevail in microcell environments.

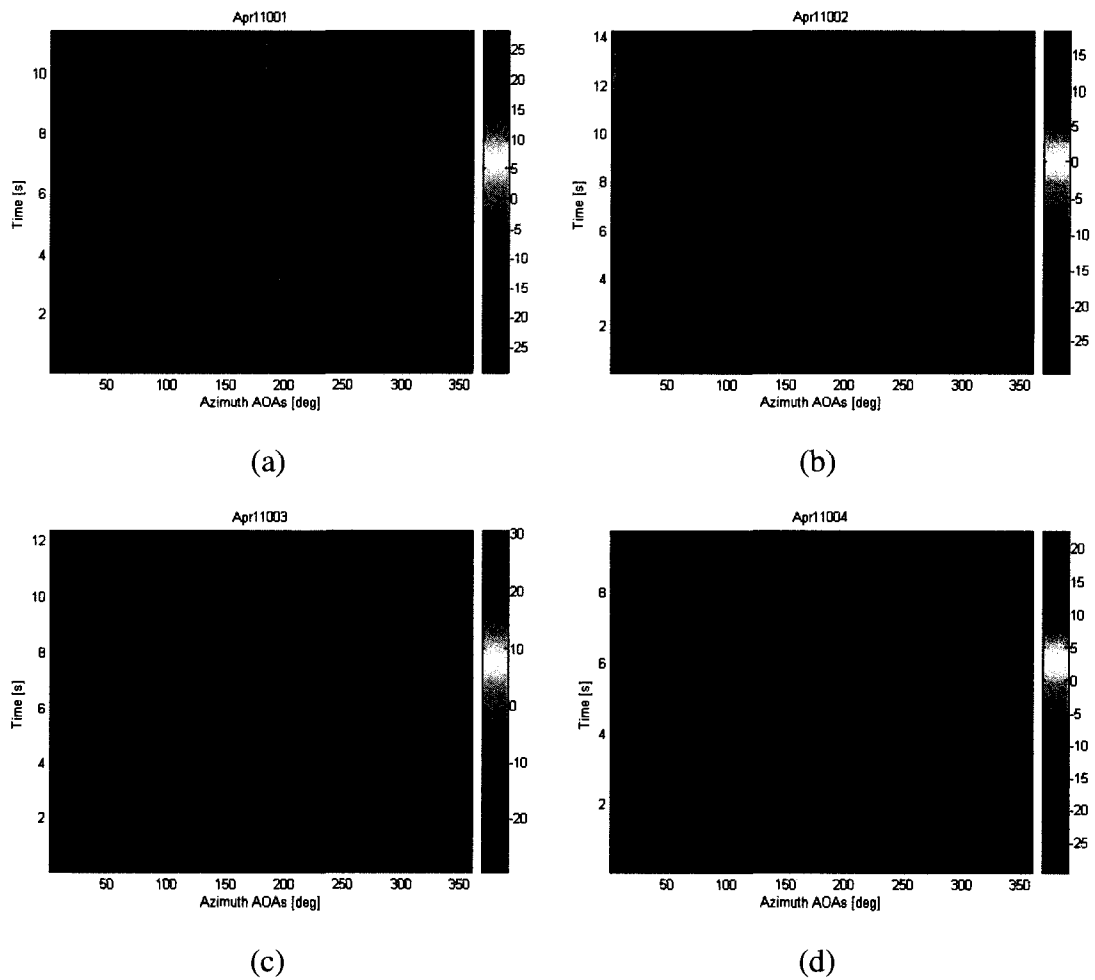


Fig. 4.2 Time series of estimated azimuth AOAs for LOS measurement runs, (a) A1, (b) A2, (c) A3, (d) A4.

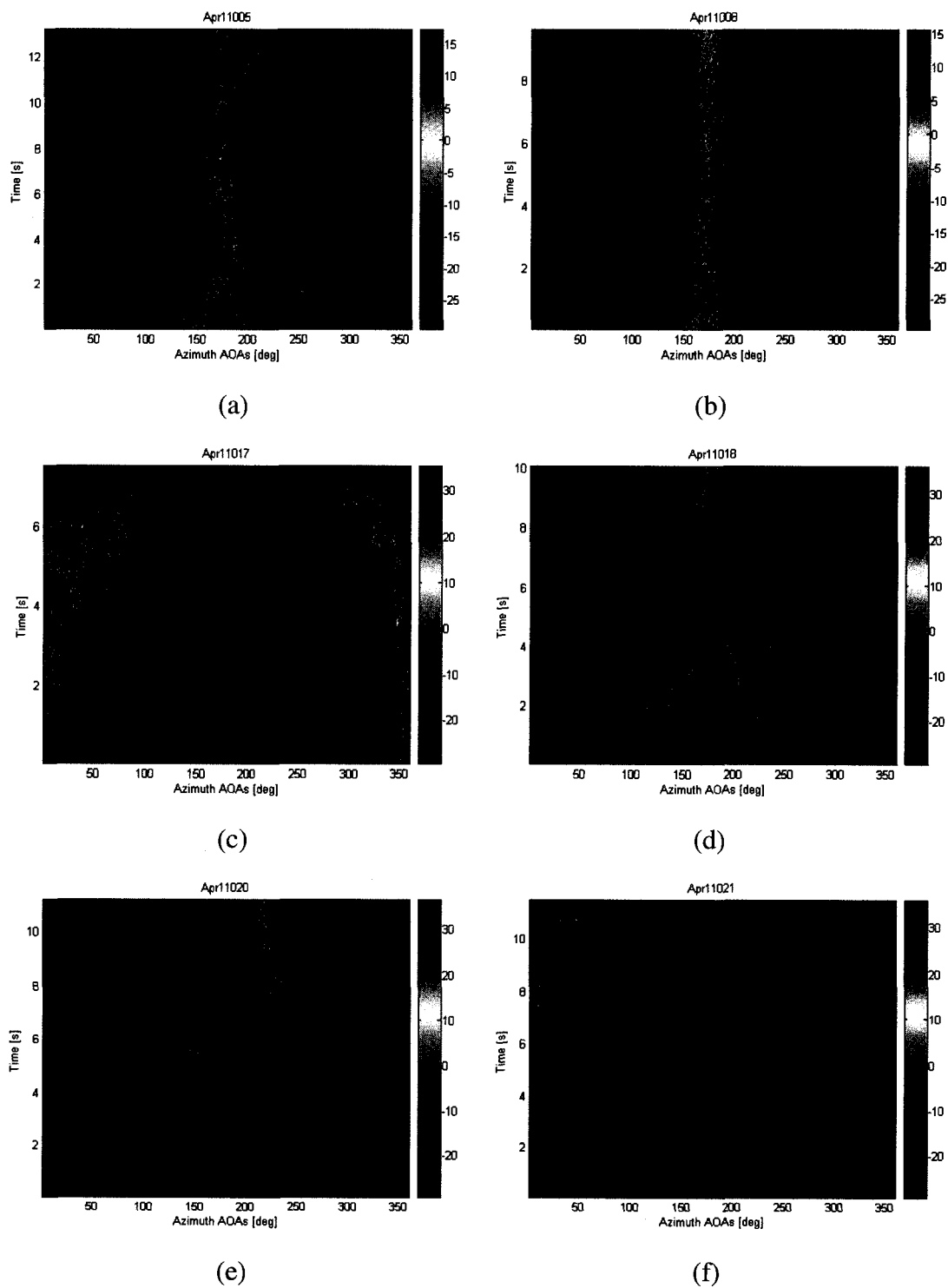


Fig. 4.3 Time series of estimated azimuth AOAs for NLOS measurement runs on streets that run perpendicular to the LOS street, (a) B5, (b) B8, (c) B17, (d) B18, (e) B20, (f) B21.

100 in each data file. Each CI is the sum of the forward and reverse intervals of consistency (IoCs) centred on the reference snapshot. The forward and reverse IoCs are estimated separately and depend on two important parameters: azimuth AOAs and delays. The shorter of the estimated IoCs for azimuth AOAs and delays in both forward and reverse directions was selected. The sum of the selected forward and reverse intervals is the determined CIs that were used as averaging intervals to generate the rms delay spreads and azimuth angular spreads. In this thesis, the critical values for the K-S tests were taken from the nearest neighbor difference ECDFs at their 100th percentiles.

Fig. 4.5 shows an example of IoCs and CIs estimated from an experiment. Both azimuth AOAs (a) and excess delays (b) were first estimated, and the shorter of IoCs from either azimuth AOAs and delays in both forward and reverse directions was selected to get CIs (c). Each bar represents a CI centred on a reference snapshot. The estimated IoCs/CIs for the forward direction are shown by the blue bars, and the estimated IoCs/CIs for the reverse direction are shown by the red bars.

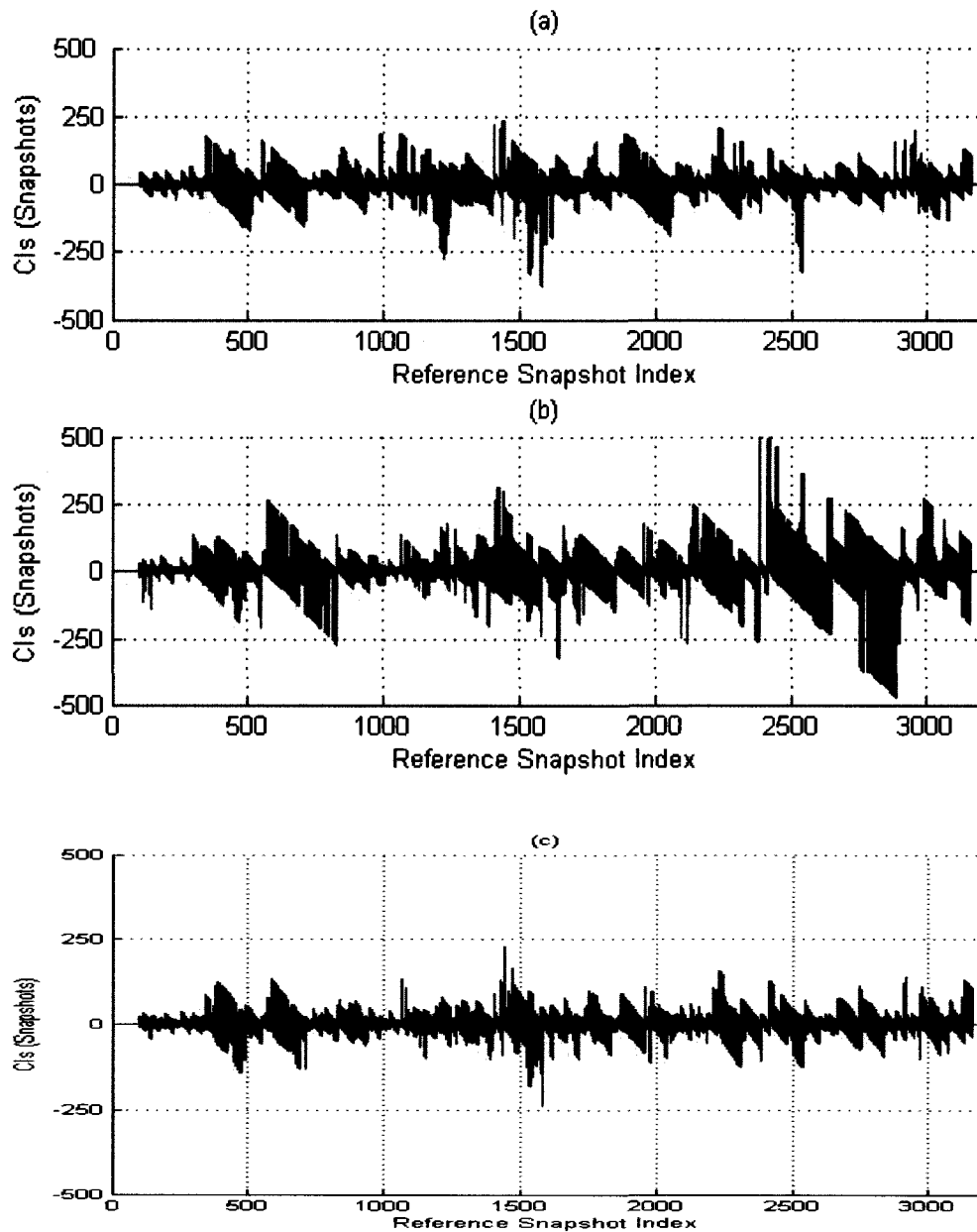


Fig. 4.5 IoCs (number of snapshots) (a) when comparing only AOA ECDFs, (b) when comparing only excess delay ECDFs, and (c) based on both AOA and excess delay ECDF comparisons. (acquisition rate = 250 snapshots per second, average vehicle speed = 5.8 mps)

The ECDFs for the IoCs for a LOS example and a NLOS example are shown in Fig. 4.6. The blue lines represent the ECDFs for the forward IoCs and the red lines represent the ECDFs for reverse IoCs. The figures show similar distribution of the IoCs for both directions in both LOS and NLOS scenario.

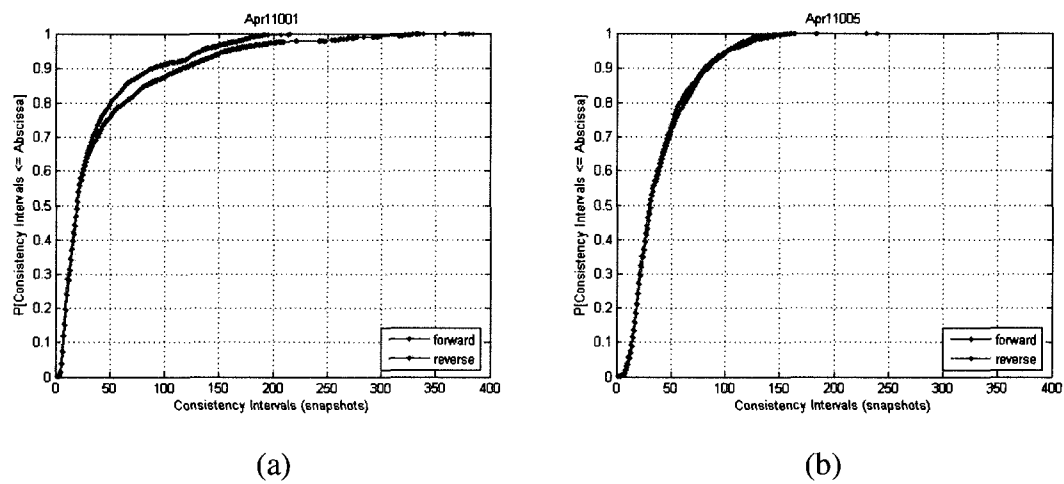


Fig. 4.6 ECDFs for IoCs for forward and reverse directions, (a) LOS, (b) NLOS.

The ECDFs for CIs for the three categories of propagation scenario are shown in Fig. 4.7

(LOS), Fig. 4.8 (NLOS perpendicular), and Fig. 4.9 (NLOS parallel) respectively.

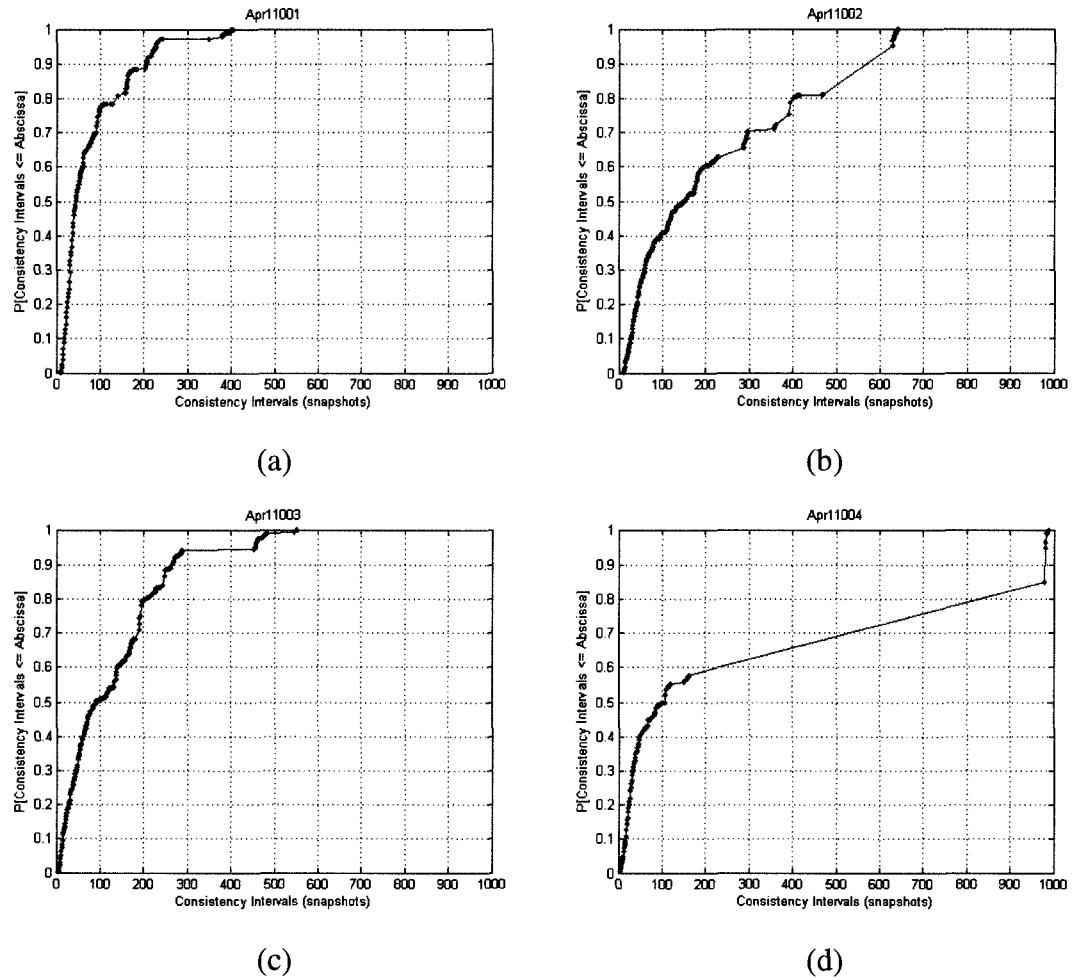
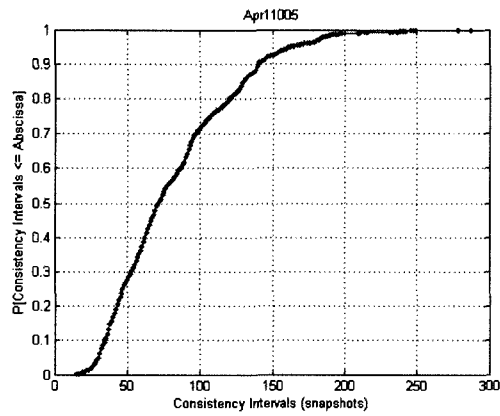
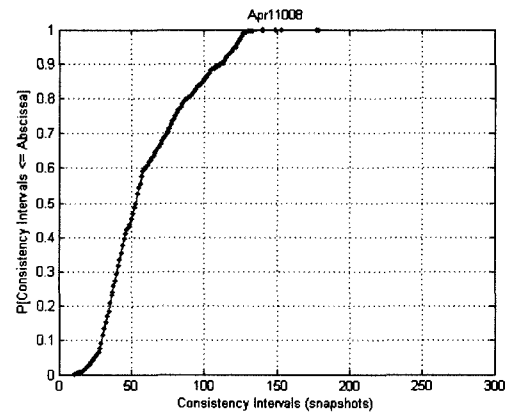


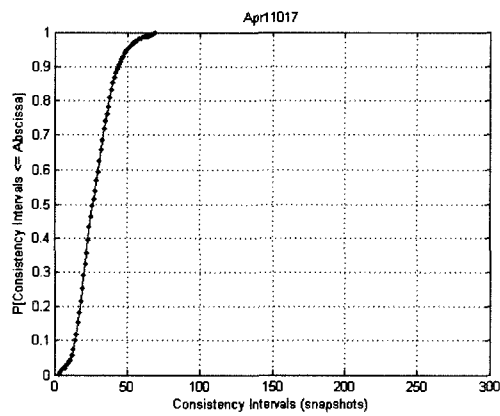
Fig. 4.7 ECDFs for CIs under LOS conditions, (a) A1, (b) A2, (c) A3, (d) A4.



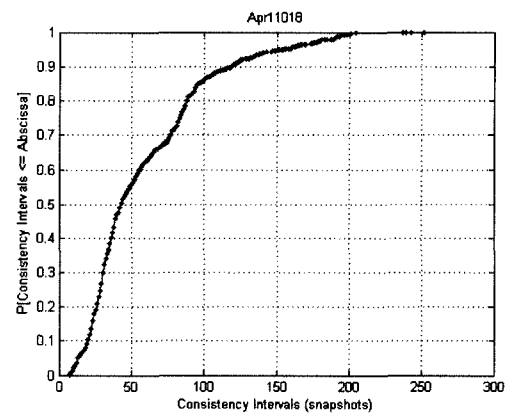
(a)



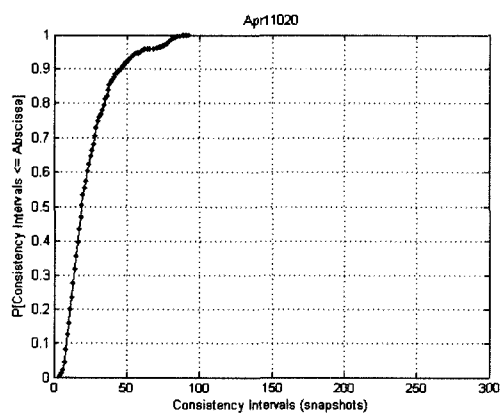
(b)



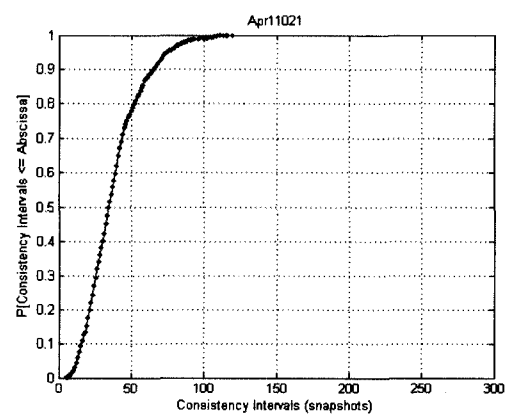
(c)



(d)



(e)



(f)

Fig. 4.8 ECDFs for CIs under NLOS conditions on perpendicular streets, (a) B5, (b) B8, (c) B17, (d) B18, (e) B20, (f) B21.

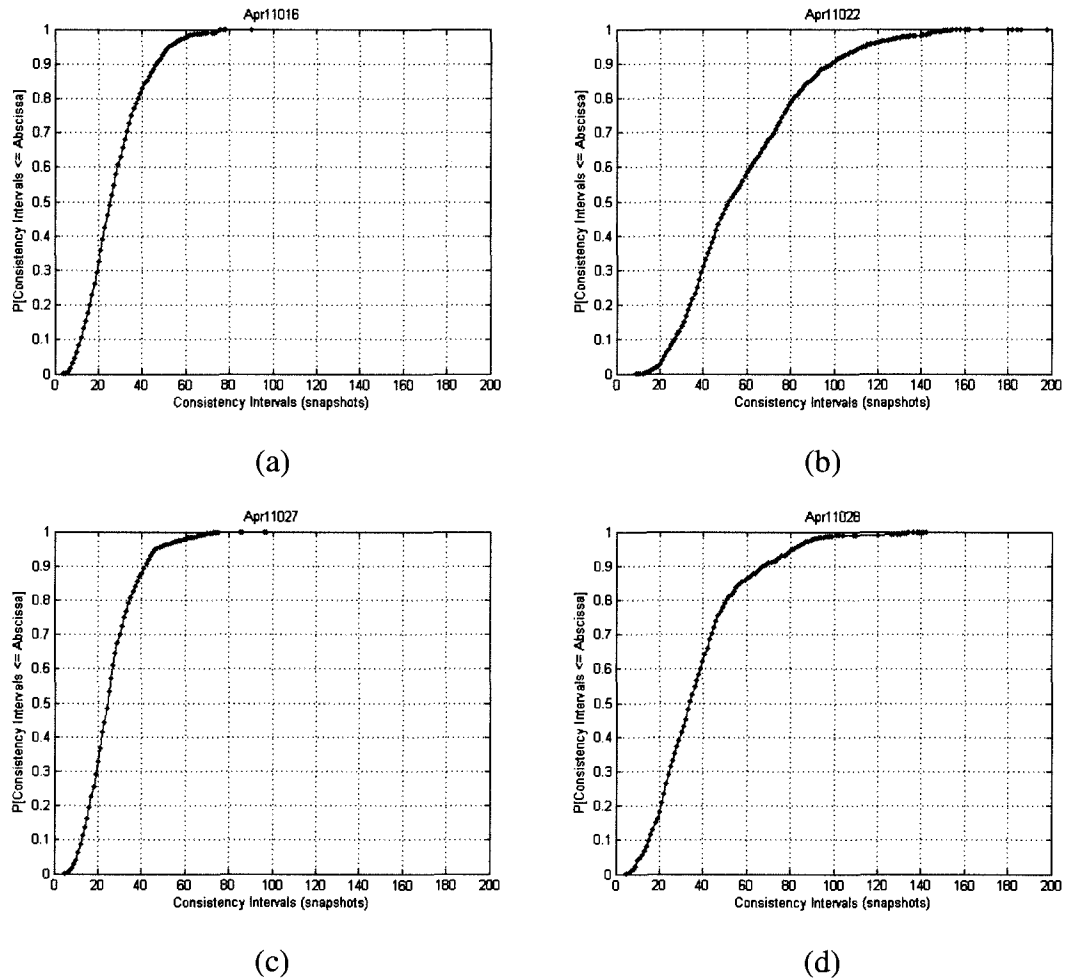


Fig. 4.9 ECDFs for CIs under NLOS conditions on parallel streets, (a) C16, (b) C22, (c) C27, (d) C28.

Comparisons were made of CI values in Table 4.1 for the different experiments of three categories. From the table, it is clear that the minimum CI values for all the measurements were very small and close, which means there were significant changes in short periods for both LOS and NLOS scenarios. The table also shows that the 50th percentiles of CI values in LOS scenarios were larger than those in NLOS scenarios, and

the 90th percentiles and maximum CI values in LOS scenarios were much larger than those in NLOS scenarios. That means more than there is a 50% possibility the periods where there were no significant changes in LOS scenarios were longer than those in NLOS scenarios, which can be explained by the fact that that the LOS signal makes the channel more stable through the power-weighting used in the estimation of the AOA and delay ECDFs.

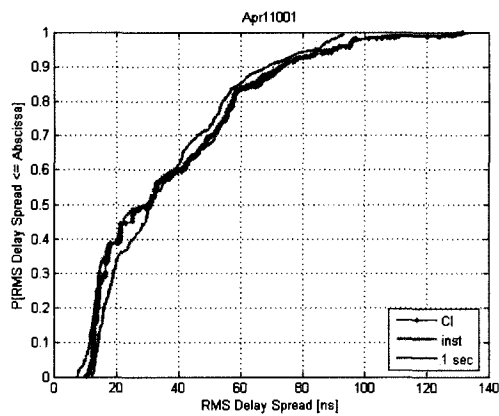
Table 4.1 Minimum, 50th percentiles, 90th percentiles, and maximum CIs computed from the measurements

	CIs (snapshots*)			
	Min.	50 th percentile	90 th percentile	Max.
A1 (LOS)	9	44	205	405
A2 (LOS)	11	150	570	642
A3 (LOS)	4	91	265	551
A4 (LOS)	4	106	980	988
B5 (NLOS)	15	71	140	287
B8 (NLOS)	11	53	112	179
B17 (NLOS)	3	26	44	69
B18 (NLOS)	7	43	119	251
B20 (NLOS)	4	19	46	92
B21 (NLOS)	5	34	65	119
C16 (NLOS)	4	25	46	90
C22 (NLOS)	9	52	99	198
C27 (NLOS)	5	24	41	97
C28 (NLOS)	5	34	67	142

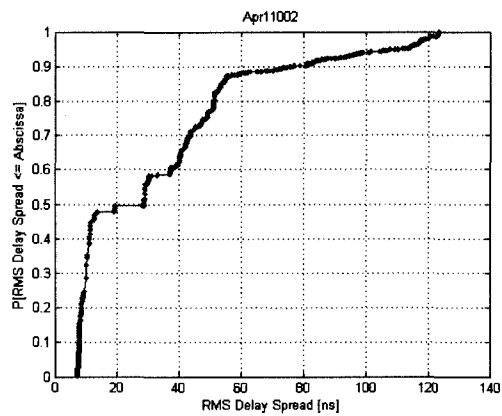
* (acquisition rate = 250 snapshots per second, average vehicle speed = 5.8 mps.)

4.3 Study of RMS Delay Spread

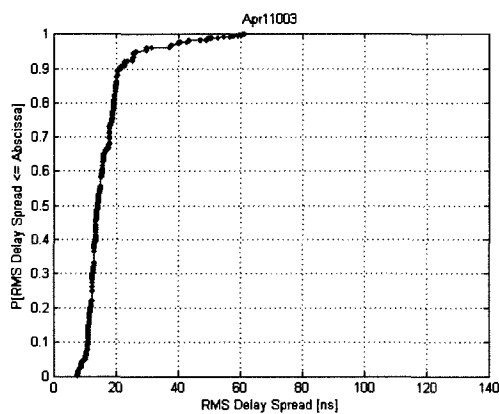
In this section, the data were processed according to methods described in Section 3.4.1. The rms delay spreads were calculated from APDPs averaged over CIs. The ECDFs of rms delay spreads for the three different propagation scenarios are shown in Fig. 4.10 (LOS), Fig. 4.11 (NLOS perpendicular), and Fig. 4.12 (NLOS parallel) respectively. The rms delay spreads were also calculated from IPDPs averaged over 32 antenna elements (instantaneous single snapshot results) and APDPs averaged over 1 second periods, with results shown in Fig. 4.10 (a), Fig. 4.11 (a), and Fig. 4.12 (a).



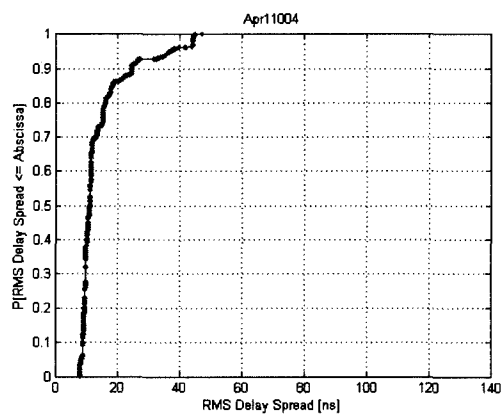
(a)



(b)



(c)



(d)

Fig. 4.10 ECDFs for rms delay spreads under LOS conditions, (a) A1, (b) A2, (c) A3, (d) A4.

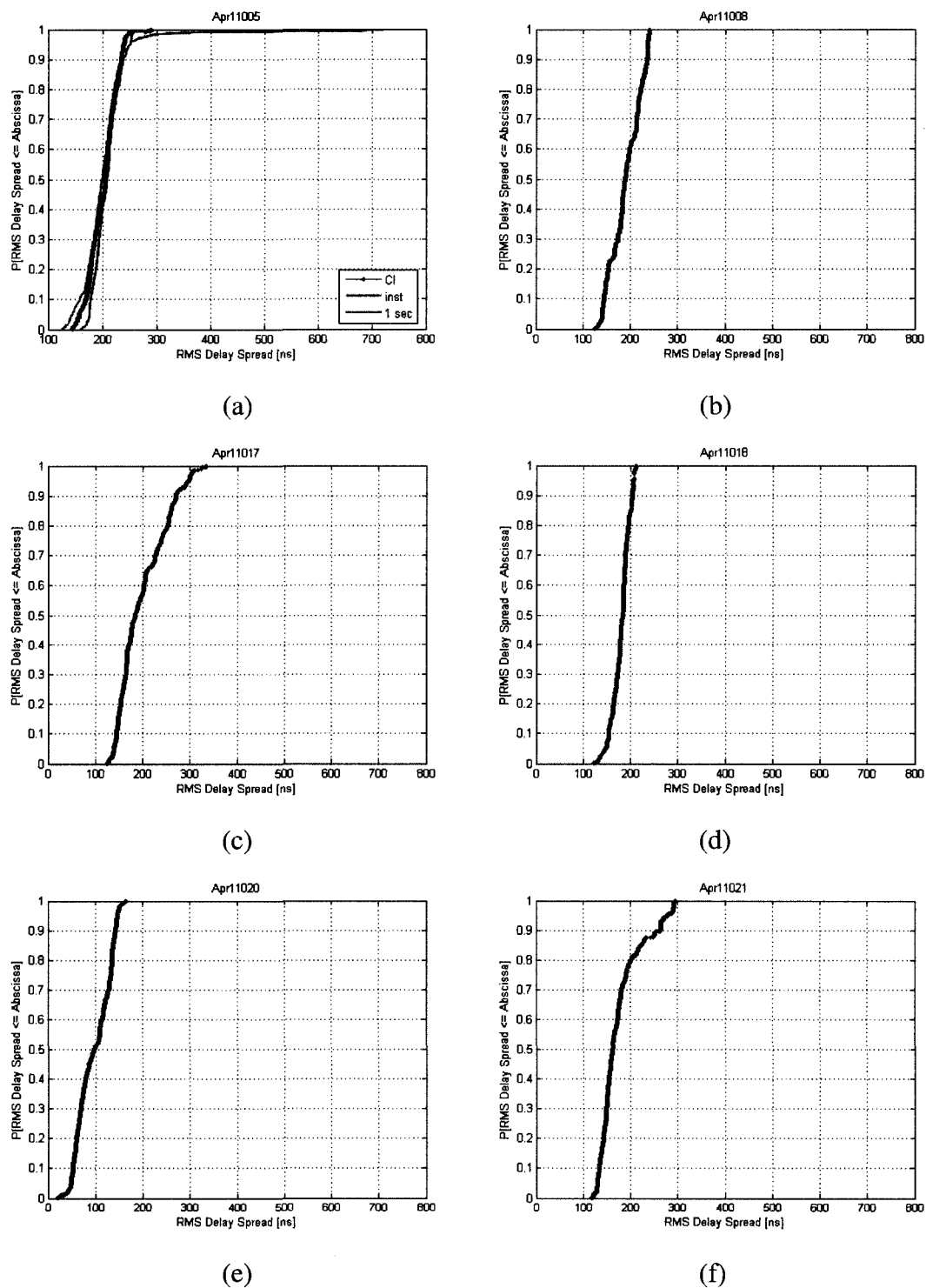


Fig. 4.11 ECDFs for rms delay spreads under NLOS conditions on perpendicular streets, (a) B5, (b) B8, (c) B17, (d) B18, (e) B20, (f) B21.

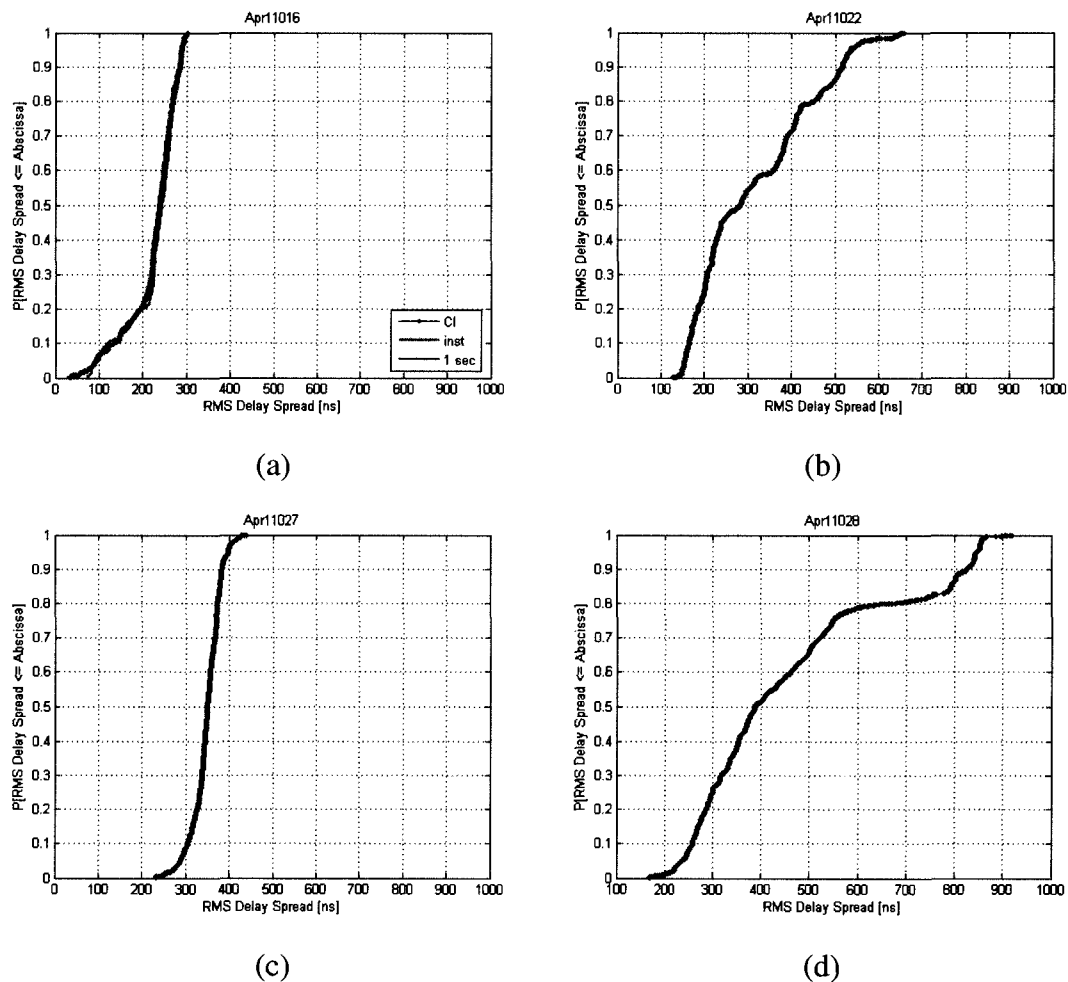


Fig. 4.12 ECDFs for rms delay spreads under NLOS conditions on parallel streets, (a) C16, (b) C22, (c) C27, (d) C28.

The comparisons among ECDFs for rms delay spreads averaged over CIs, single array snapshots (which is a spatial average), and 1 second in Fig. 4.10 (a), Fig. 4.11 (a), and Fig. 4.12 (a) show that the ECDFs of rms delay spreads averaged over CIs lie mostly between those averaged over 1 snapshot and 1 second, and they are so close as to represent similar distributions.

Comparisons were made of rms delay spreads estimated by averaging over CIs in Table 4.2 for the different experiments for propagation scenarios in the three categories. From the table, the rms delay spreads in LOS scenarios can be seen to be much smaller than those in NLOS scenarios, because in LOS scenarios most received energy is directly from the transmit antenna. The rms delay spreads are greater on parallel streets than on perpendicular streets. Propagation measurement results analyzed during this thesis project show that on NLOS streets in microcells, most energy propagates through the streets by diffractions from the buildings at the street intersections and at gaps between buildings. One can see in Fig. 4.1 that the signal from the transmitter requires diffraction at 2 intersections to reach all parallel streets, and 1 intersection to reach all perpendicular streets. On parallel streets the dominant signals are therefore weaker and the distances between the transmitter and the receiver are longer. Therefore, the rms delay spreads on parallel streets are greater than on perpendicular streets.

Table 4.2 Minimum, 50th percentiles, 90th percentiles, and maximum rms delay spreads estimated from the measurements

	rms delay spreads (ns)			
	Min.	50 th percentile	90 th percentile	Max.
A1 (LOS)	11	31	73	132
A2 (LOS)	8	29	77	124
A3 (LOS)	8	14	21	62
A4 (LOS)	8	11	24	47
B5 (NLOS)	144	206	234	290
B8 (NLOS)	124	189	236	241
B17 (NLOS)	124	183	270	334
B18 (NLOS)	123	184	203	211
B20 (NLOS)	20	97	143	165
B21 (NLOS)	118	162	263	296
C16 (NLOS)	33	240	284	303
C22 (NLOS)	127	283	515	658
C27 (NLOS)	231	350	383	438
C28 (NLOS)	167	386	825	919

4.4 Study of Azimuth Angular Spread

In this section, the data were processed according to methods described in Section 3.4.3.

The ECDFs of azimuth angular spreads for the three propagation scenarios are shown in

Fig. 4.13 (LOS), Fig. 4.14 (NLOS perpendicular), and Fig. 4.15 (NLOS parallel)

respectively.

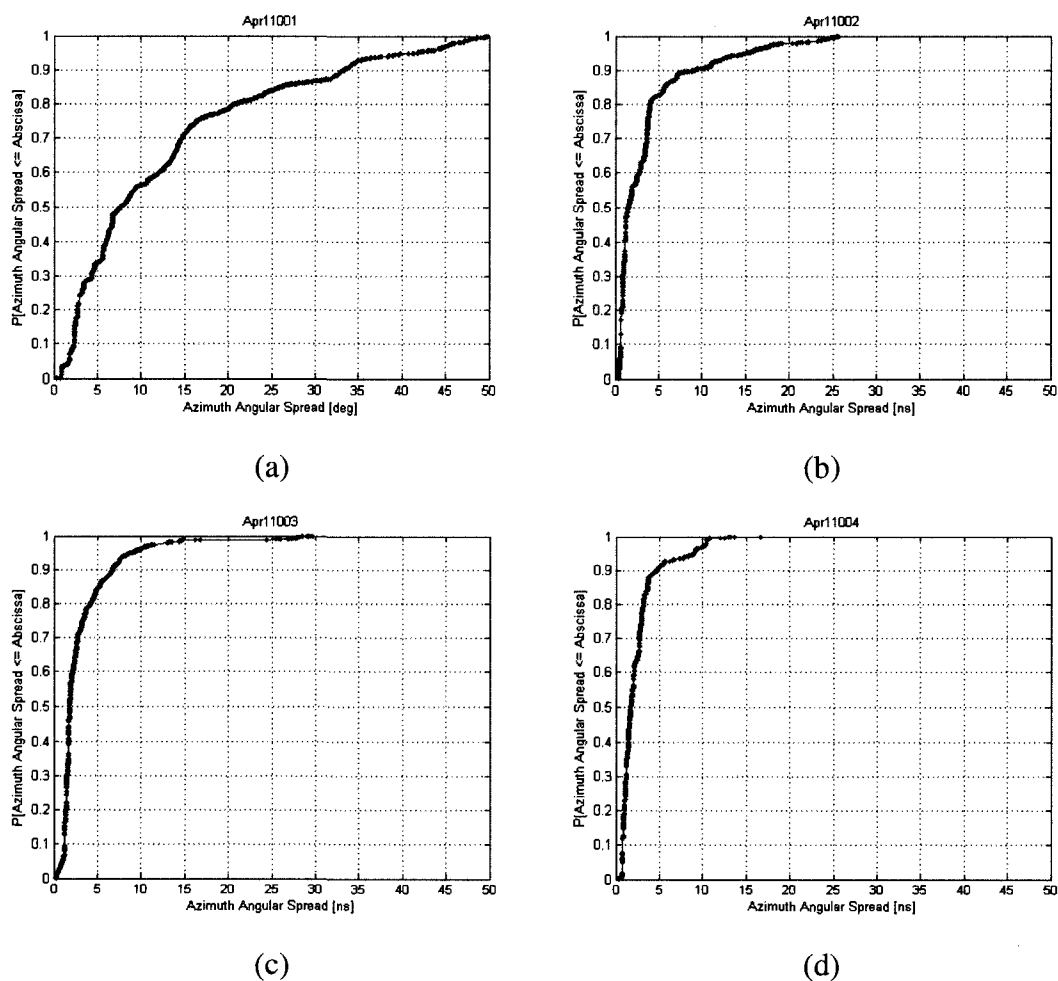


Fig. 4.13 ECDFs of azimuth angular spreads under LOS conditions, (a) A1, (b) A2, (c) A3, (d) A4.

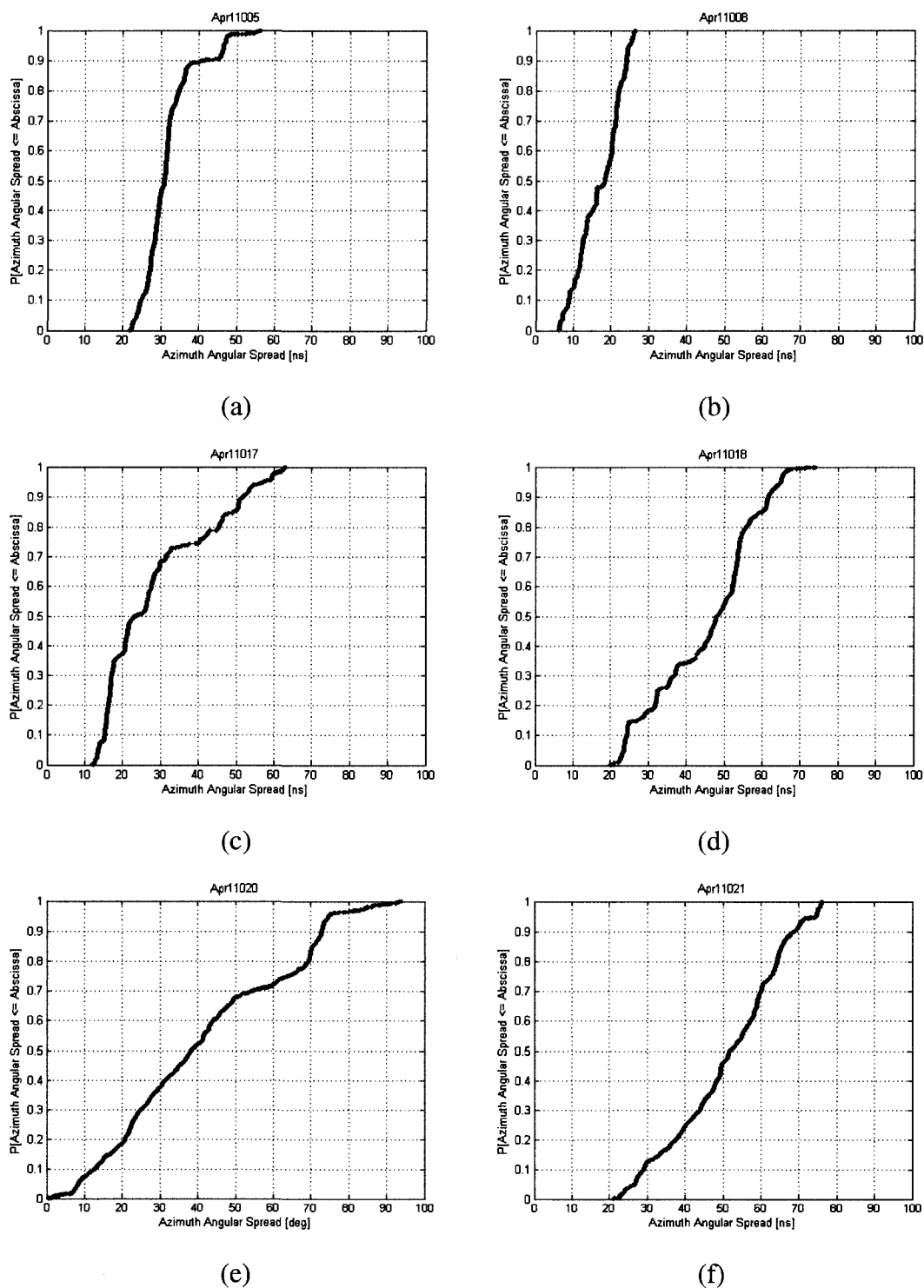


Fig. 4.14 ECDFs for azimuth angular spreads under NLOS conditions on perpendicular streets, (a) B5, (b) B8, (c) B17, (d) B18, (e) B20, (f) B21.

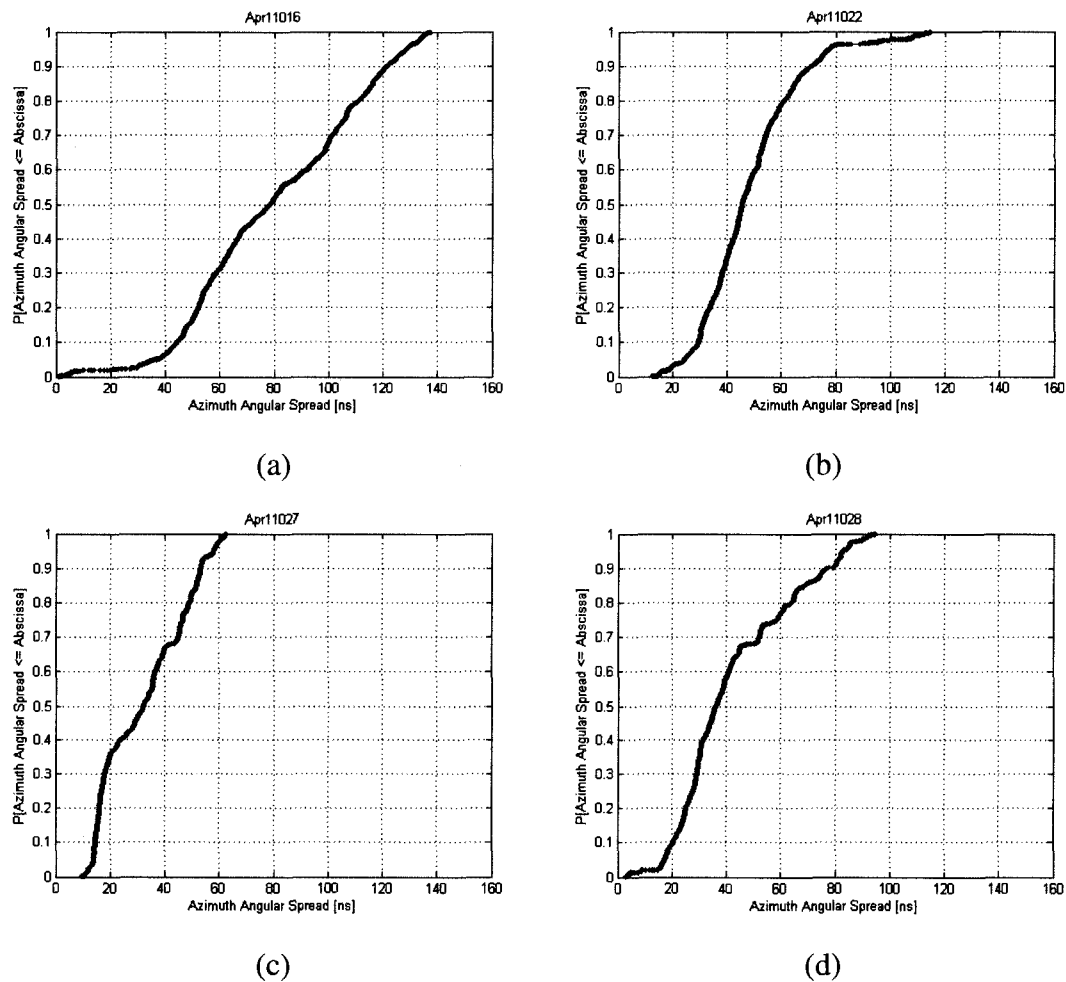


Fig. 4.15 ECDFs for azimuth angular spreads under NLOS conditions on parallel streets, (a) C16, (b) C22, (c) C27, (d) C28.

Comparisons were made of azimuth angular spreads in Table 4.3 for the different experiments in three propagation scenarios. From the table, it is clear that the azimuth angular spreads in LOS scenarios are smaller than those in NLOS scenarios, because in LOS scenarios most received energy is directly from the transmit antenna.

Table 4.3 Minimum, 50th percentile, 90th percentile, and maximum azimuth angular spreads computed from the measurements

	angular spreads (deg)			
	Min.	50 th percentile	90 th percentile	Max.
A1 (LOS)	1	7	33	50
A2 (LOS)	1	2	9	26
A3 (LOS)	1	2	7	30
A4 (LOS)	1	2	5	17
B5 (NLOS)	22	31	41	56
B8 (NLOS)	6	18	24	26
B17 (NLOS)	12	23	52	63
B18 (NLOS)	20	48	62	74
B20 (NLOS)	1	38	73	94
B21 (NLOS)	21	52	69	76
C16 (NLOS)	5	78	121	137
C22 (NLOS)	13	45	72	114
C27 (NLOS)	10	32	53	62
C28 (NLOS)	3	36	77	95

4.5 Study of the Dependence of RMS Delay Spread on Measurement System Bandwidth

It is difficult to compare rms delay spread results from different papers reporting measurements made with channel sounders have different bandwidths. Therefore, it is necessary to investigate the relationship between rms delay spreads and measurement system bandwidths. For example, it would be good to be able to extrapolate rms delay spreads estimated from data recorded with a sounder having 10 MHz RF bandwidth to get an equivalent for 200 MHz RF bandwidth. This section reports a study of how rms delay spread varies with measurement system bandwidth in a microcell environment. In the following sections, measurements from downtown Ottawa will be analyzed and results from computer simulations will be compared with measurement results to draw conclusions.

4.5.1 Measurement Results

Radio propagation experiments were conducted on August 18, 2006 in downtown Ottawa as shown in Fig. 4.1. The configuration of this measurement was different than the measurement used during experiments reported in Section 4.1 in the following ways.

Data were recorded at 250 snapshots per second and the carrier frequencies were switched between 2.25 GHz and 5.8 GHz. There were 4 PN sequences in 1 snapshot and they were averaged to increase the SNR. There were two transmit antennas. A quarter-wavelength monopole was used for the 2.25 GHz transmit antenna, and a biconical antenna was used for 5.8 GHz transmit antenna. The receive antenna was a biconical antenna mounted on the minivan at a height of 1.8 metres and the minivan moved at speeds between 10 kph and 20 kph. The rms delay spreads were estimated from APDPs averaged over 1 second. This choice of averaging interval was made because this work was done earlier than the work on CIs. In a 1 second period, the vehicle moved a distance of about 4 metres.

Fig. 4.16 and Fig. 4.17 show the rms delay spread ECDFs for 100 MHz LOS measurements and NLOS measurements at both 2.25 GHz and 5.8 GHz carrier frequencies. One hundred APDPs were used to estimate the rms delay spread ECDFs for both LOS and NLOS scenarios.

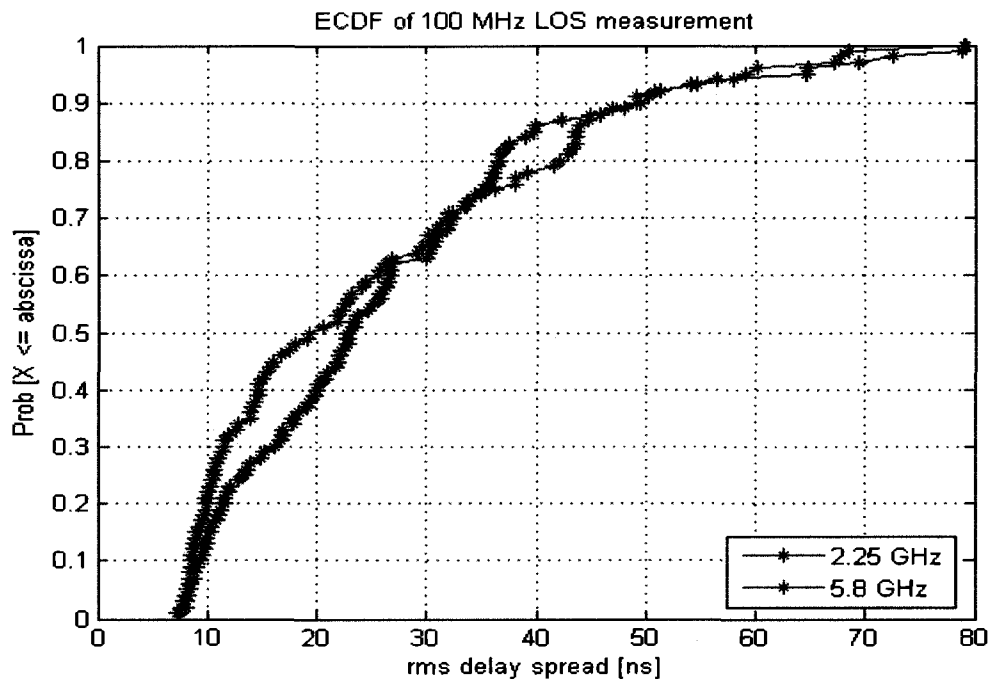


Fig. 4.16 ECDFs for rms delay spreads at two carrier frequencies from LOS scenarios.

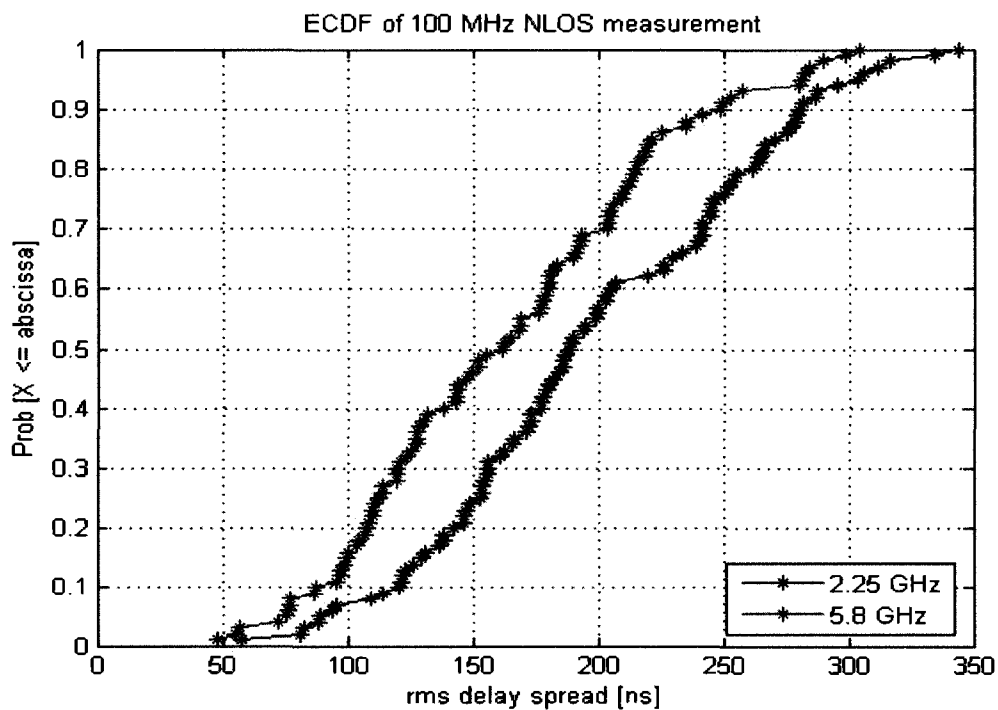


Fig. 4.17 ECDFs for rms delay spreads at two carrier frequencies from NLOS scenarios.

4.5.2 Filtered Measurements Results for Different Bandwidths

In order to analyze rms delay spreads for different system bandwidths, Finite Impulse Response (FIR) filters were used to filter measured data to obtain filtered channel transfer functions with bandwidths 10 MHz to 80 MHz. The FIR filter that was used was a 100th order bandpass filter using the Hamming window method provided by MATLAB. The magnitude and the phase of the frequency response of a 40 MHz wide FIR filter are shown in Fig. 4.18. The filter meets requirements well as one can see a fast and smooth transition at the cut-off frequency and a linear phase response.

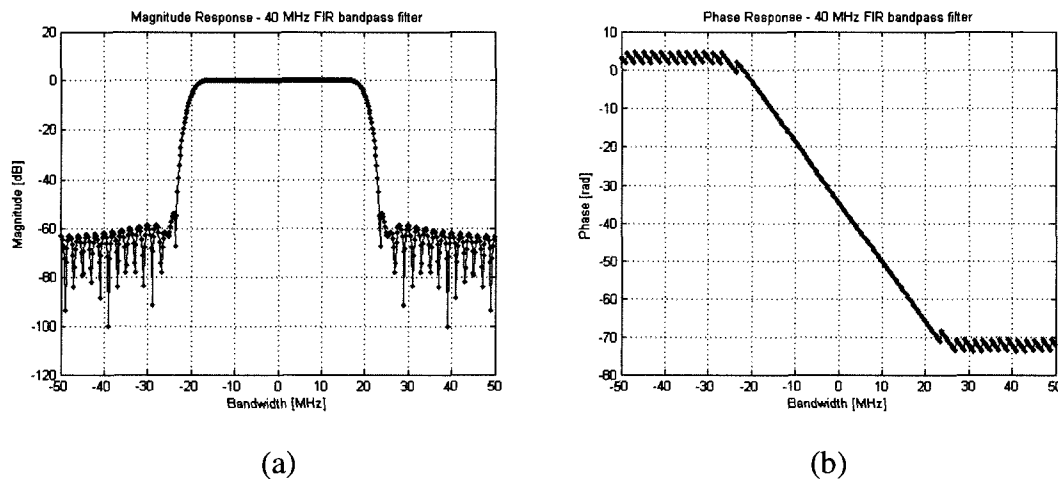


Fig. 4.18 Magnitude (a) and phase (b) of the FIR filter.

The frequency responses of the filters were multiplied with estimated channel transfer functions to obtain equivalent channel transfer functions with bandwidths ranging from

10 MHz to 80 MHz. The rms delay spread for each bandwidth was calculated from these results. The scatter plot of the relationship between the system bandwidth and rms delay spreads is shown in the following figures. Fig. 4.19 shows the LOS case at 2.25 GHz (a) and 5.8 GHz (b). Fig. 4.20 shows the NLOS case at 2.25 GHz (a) and 5.8 GHz (b). The green line indicates a 3rd degree polynomial curve fit using the least squares method.

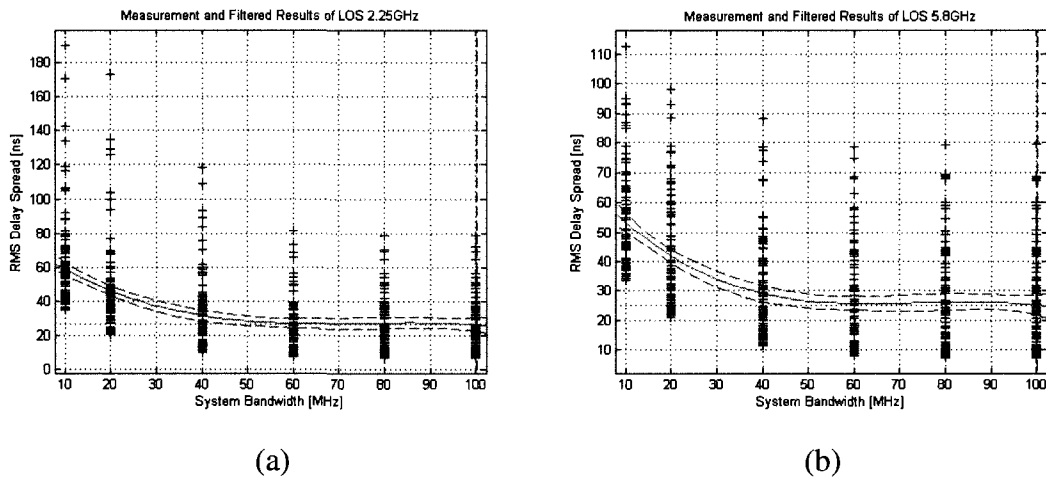


Fig. 4.19 Relationship between rms delay spread and system bandwidth for measured and filtered results from LOS scenarios at carrier frequencies of 2.25 GHz (a) and 5.8 GHz (b).

The equation of the cubic fit in Fig. 4.19 (a) is given by

$$y = -0.00011939x^3 + 0.027242x^2 - 2.0361x + 77.178, \quad (4-1)$$

where y represents rms delay spread, and x represents system bandwidth.

The equation of the cubic fit in Fig. 4.19 (b) is given by

$$y = -0.00011336x^3 + 0.025273x^2 - 1.8365x + 69.353. \quad (4-2)$$

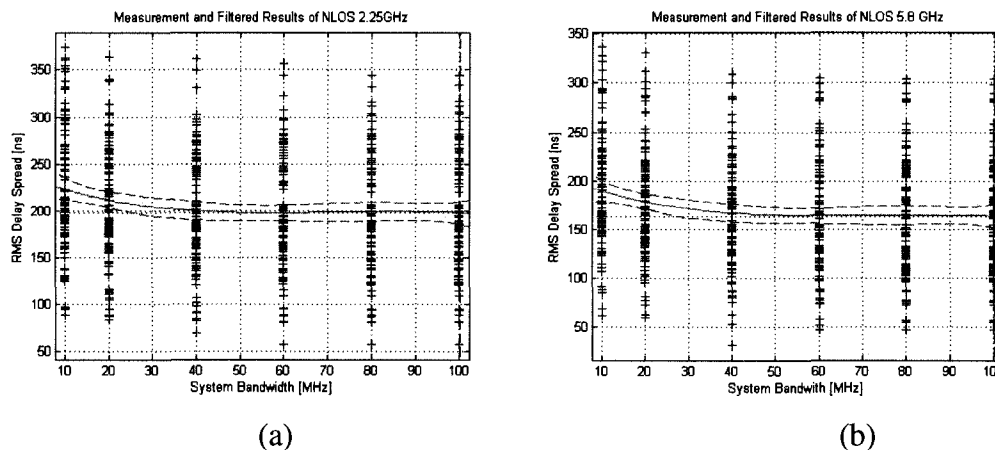


Fig. 4.20 Relationship between rms delay spread and system bandwidth for measured and filtered results from NLOS scenarios at carrier frequencies of 2.25 GHz (a) and 5.8 GHz (b).

The equation of the cubic fit in Fig. 4.20 (a) is given by

$$y = -0.00012762x^3 + 0.0274x^2 - 1.8828x + 239.85. \quad (4-3)$$

The equation of the cubic fit in Fig. 4.20 (b) is given by

$$y = -0.00010969x^3 + 0.024143x^2 - 1.7303x + 205.03. \quad (4-4)$$

Conclusions:

- For LOS cases, the rms delay spread is almost the same for both carrier frequencies, because multipath signals with significant energy come from the LOS wave and the

reflection of waves from buildings. Since the buildings are large, the reflection process is nearly independent of frequency.

- For NLOS cases, the rms delay spread of 2.25 GHz is larger than that of 5.8 GHz. This could be caused by the fact that the diffraction loss from buildings at 5.8 GHz is larger than that of 2.25 GHz, and the building penetration loss at 5.8 GHz is larger than that at 2.25 GHz, and hence multipath waves with longer delays are attenuated more at 5.8 GHz.
- The rms delay spread decreases for measurement system RF bandwidths from 10 MHz to 40 MHz and thereafter, remains at almost the same value for measurement system RF bandwidths from 40 MHz to 100 MHz.

4.5.3 Simulation of LOS Scenarios

To study the effect of bandwidth on rms delay spread in the LOS case, a MATLAB plane wave simulator code was written based on the often referred to Geometrically Based Single Bounce Elliptical Model (GBSBEM) [30]. The interacting objects were uniformly distributed in the associated ellipse with the transmitter and receiver at its foci as shown in Fig. 4.21. The red asterisk represents the transmitter and red dots represent 10 receive locations. The blue squares represent interacting objects.

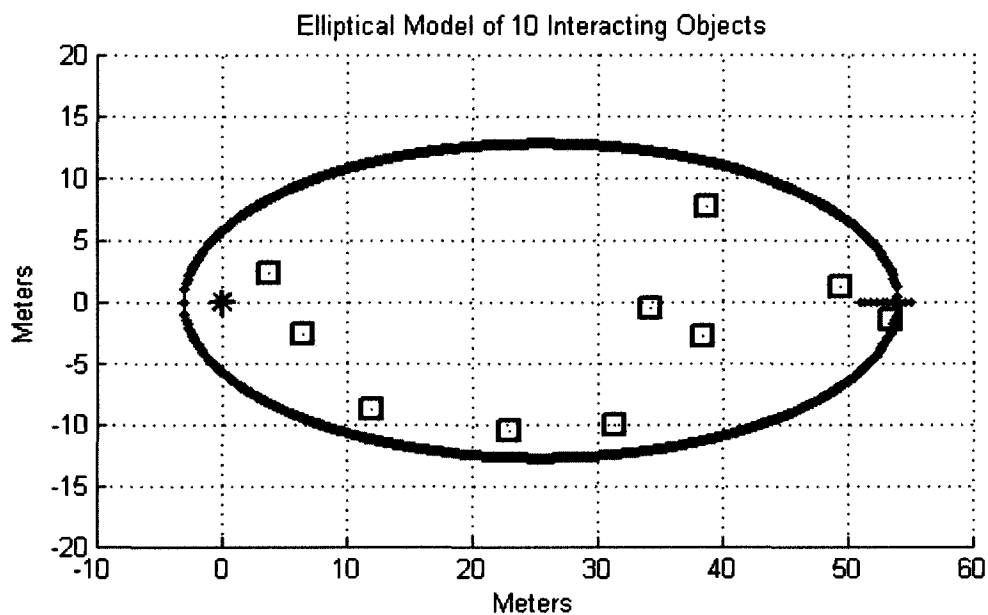


Fig. 4.21 Elliptical model with 10 interacting objects.

The elliptical model assumes that the interacting objects are distributed within an ellipse where the transmitter and the receiver are the foci of the ellipse. In LOS cases, most of the waves arriving at the receiver come from the direction of the transmitter. This model therefore fits the scenario well.

The power and the phase of each multipath component are a function of the length of the propagation path it follows between the transmitter and the receiver. The interacting (i.e.

scattering or reflection) coefficients of the interacting objects were assumed uniformly distributed between 0.1 and 1. The phase shifts incurred by the interacting objects were assumed to be uniformly distributed between 0 and 2π . To be consistent with the acquisition method used in measurements, each APDP was the temporal average of 10 instantaneous power delay profiles uniformly distributed along a 30λ straight line, which is about 4 metres at 2.25 GHz. The SNR was 30 dB. The number of interacting objects was 10. The major axis of the ellipse is represented by $2a$, and the minor axis of the ellipse is represented by $2b$. The distance between the transmitter and the receiver is represented by $d = 2f$. Different values of b were used in the simulation, and finally $b = d/4 = f/2$ was chosen, because with this value, the rms delay spreads calculated from simulations exhibited similar CDFs to those from measurement results. In total, 400 APDPs were simulated with d uniformly distributed from 51 metres to 450 metres. The simulation results are compared with measurement results for 2.25 GHz and 5.8 GHz in Fig. 4.22.

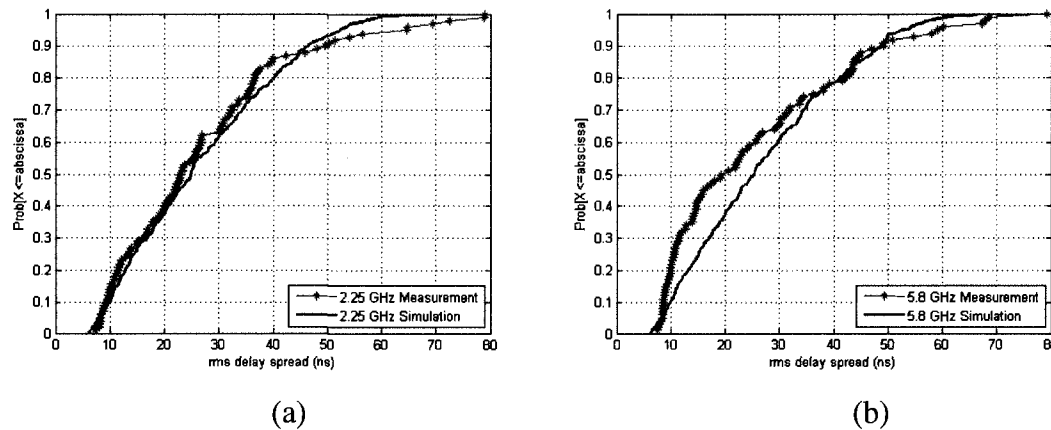


Fig. 4.22 Comparison of simulation and measurement results for rms delay spreads at carrier frequencies of 2.25 GHz (a) and 5.8 GHz (b).

To study the influence of system bandwidths from 5 MHz to 200 MHz, 100 APDPs were simulated with d uniformly distributed from 51 metres to 450 metres for each bandwidth. The scatter plot of the relationship between the system bandwidth and the rms delay spread with 6th degree polynomial curve fit is shown in Fig. 4.23. This simulation result corresponds well with the measurement results for RF bandwidths from 10 MHz to 100 MHz and extends them to be applicable for an RF bandwidth of 200 MHz.

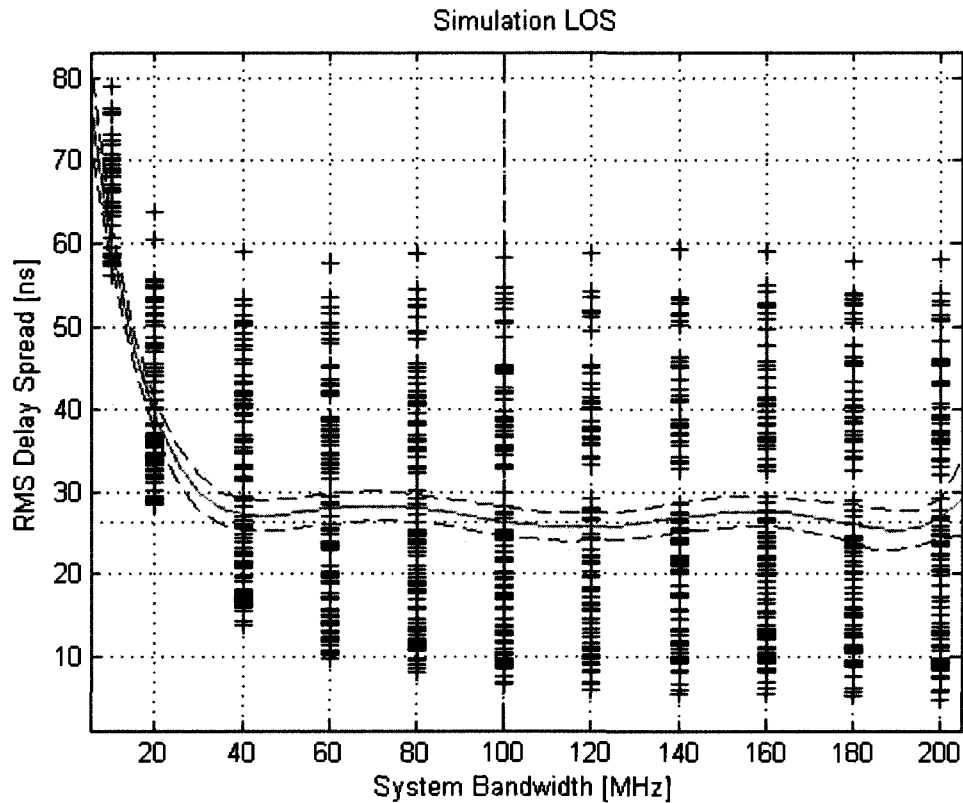


Fig. 4.23 Relationship between rms delay spread and system bandwidth for simulated LOS scenarios at a carrier frequency 2.25 GHz.

Simulations were also made to explain why the rms delay spread varies with the system RF bandwidth. The simulation used the above LOS model and the distance transmitter and receiver separation was 100 metres. Fig. 4.24 shows the APDPs for different system bandwidths (a) and the power and arrival time (b) of 10 multipath components, equivalent to what would be observed with an infinite bandwidth.

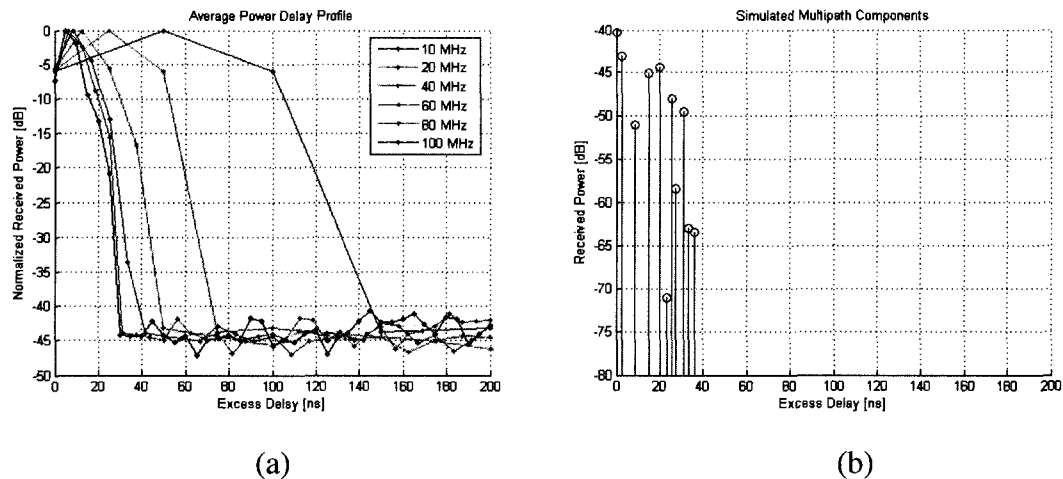


Fig. 4.24 Simulated APDP for different system bandwidths (a) and the power and arrival times (b) of 10 multipath components.

From Fig. 4.24, one can see that the wider the RF bandwidth, the better the ability to resolve the multipath components, and that there is not much change after a bandwidth of 40 MHz. The time resolution of multipath components is two times the chip period for the PRBS (Pseudo-Random Binary Sequence) sounding signal used in the simulations. In other words, if two multipath components arrive at time differences equal to or longer than two chip durations, they can be resolved by the system. When the resolution is better, the rms delay spread decreases because there is no vector addition of multiple multipath components, which can enhance the power of multipath groups within the system resolution interval. It also avoids the interpolation of the impulse response profile between multipath groups where there is actually no power.

The rms delays spread calculated from APDPs representing results measured with sounders having different RF bandwidths are shown in Table 4.4, and compared with the actual rms delay spread, which is calculated from the power and arriving time of the simulated multipath components (i.e. the infinite bandwidth equivalents)

Table 4.4 RMS delay spreads obtained from different system bandwidths

Simulated Channel Sounder Bandwidth (MHz)	RMS Delay Spread (ns)
10	57.67
20	28.83
40	15.76
60	11.62
80	10.10
100	8.28
Actual value based on knowledge of simulated multipath component powers and delays	10.42

The results for 80 and 100 MHz RF bandwidths are smaller than the actual value. This could be the result of multipath components arriving within the delay resolution interval that cancel each other because of their phase differences.

There is still some difference between the measurement and simulation results. This

could be for the following reasons:

- The simulation assumes a single interaction, whereas, multiple interactions might have taken place on the measured radio channels.
- The measurements might include multipath signals from interacting objects far from the transmitter, for example, high buildings 4 or 5 blocks away. The simulation only includes multipath signals from the specified geometrical region.
- The snapshots of the simulation are uniformly distributed in space, while the snapshots from the measurement are uniform in time, but the vehicle speed might not have been constant, making sampling in space non-uniform.

Simulations for NLOS conditions are not reported because the single interaction model described above resulted in a poor comparison between measurement and simulation results and an alternate more suitable model was not found for NLOS cases. This was therefore left for future study.

In this chapter, it was found that rms delay spreads are a function of measurement system bandwidth. They decrease rapidly for RF bandwidths between 10 MHz and about 30 MHz, then level at approximately 50 MHz, continuing thereafter at a constant, minimum value. This is because it is only at bandwidths above about 50 MHz, that the envelope

enclosing the last received multipath component falls rapidly enough on its trailing edge that the spreading due to the finite bandwidth is insignificant, and this doesn't change significantly as bandwidth increases further. A polynomial equation is reported for estimating rms delay spreads for systems with different bandwidths. This equation could be fine tuned, given estimates from reported measurements made by others of rms delay spreads for a specific bandwidth, in order to estimate equivalent results for greater bandwidths.

Chapter 5

Summary, Conclusions and Recommendations for Further Research

5.1 Summary

This thesis had the objective of estimating rms delay spreads and azimuth angular spreads at a vehicular mobile receiver in a microcell environment. Such results are required for the accurate simulation of radio channel processes for the evaluation of new mobile radio systems concepts and technologies. Appropriate equipment was reconfigured and calibrated, and wideband propagation measurements were made in downtown Ottawa using a UCA and a 50 Mchps PN channel sounder operating at 2.25 GHz. A number of previously-reported high-resolution AOA estimation algorithms were evaluated and the most suitable ones were chosen to estimate AOAs in azimuth and associated azimuth angular spreads. A novel procedure for selecting the averaging intervals, the CIs, was used to estimate the rms delay spreads and angular spreads.

The popular high-resolution AOA estimation algorithms UCA-RB-MUSIC,

UCA-ESPRIT, and SAGE were reviewed, and their performance attributes evaluated. Initially, the UCA-RB-MUSIC algorithm was selected as most appropriate because its accuracy is better than that of the UCA-ESPRIT algorithm and both of the aforementioned are less computationally intensive than SAGE. However, it was found that the UCA-RB-MUSIC algorithm was too computationally inefficient and took unacceptable time durations to generate results from measured data. The UCA-ESPRIT algorithm, the implementation of which ran almost ten times faster, was therefore used to analyze most measurement data during this thesis project.

A measurement system including the channel sounder and the switched UCA was built at CRC by a team of researchers, with participation by the author. The equipment was tested and calibrated, and the accuracy and resolution of AOA estimates made using data recorded by the measurement system were accessed through experiments. Then, the measurement system was set up so as to simulate a base station (transmitter) and a mobile station (receiver) in an urban microcell in downtown Ottawa and experiments were carried out. To process the measurement data, algorithms were written to align estimated impulse response functions, generate APDPs, make high resolution AOA estimates, and exclude duplicates in the high resolution results from adjacent propagation time delay intervals.

To eliminate concerns about previously reported multipath dispersion results based on averaging over arbitrary intervals to estimate rms delay spreads and angular spreads, a newly-reported method using K-S tests was applied to identify changes in radio channel properties. The intervals between significant changes, herein referred to as CIs, were used as the required averaging intervals.

The measurement results were categorized as belonging to three different propagation scenarios according to the physical environment, including: LOS, NLOS on streets perpendicular to the LOS street, and NLOS on streets parallel to the LOS street. The AOA results from these three scenarios were studied. Algorithms were also written to estimate CIs, rms delay spreads and azimuth angular spreads. The ECDFs of rms delay spreads and azimuth angular spreads for these three scenarios on streets surrounding one base station location were reported and compared.

Finally, a study of the dependence of rms delay spread on measurement system bandwidth based on both experiments and simulations was reported. As a spin-off, this work resulted in a better understanding of the multipath propagation mechanisms in LOS microcells through comparisons between modelling and measurement results. However, such comparisons were poor for NLOS scenarios.

5.2 Conclusions

During the course of work for the thesis project reported herein, a number of results led to conclusions on various aspects of the work, including: the estimation of channel parameters, radio wave propagation in microcells, and microcell channel modelling.

These conclusions can be summarised as follows:

(a) The Estimation of Channel Parameters

- The accuracy of elevation AOA estimates using a UCA, which is a planar antenna array, is poor because the elevation plane beamwidth of the array is large, since its aperture is small in the vertical plane. Therefore, a 3D antenna array should be used to estimate elevation angles.
- The cross sectional sizes of materials used in the UCA that was implemented for the work reported here are large enough to shadow some waves. Slimmer materials should be used on next generation UCA or 3D array.
- When the thesis project reported herein began, there was considerable scepticism about the use of arbitrary intervals for averaging to estimate rms delay spreads, as has been the practice by many researchers over the past 30 years. This is because it was considered that changing multipath conditions could produce erroneous

averaging results due to the mixing of different channel processes. A recently reported procedure was therefore applied to estimate intervals along a street wherein multipath conditions remain consistent. Averaging to estimate rms delay spreads and azimuth spreads was then conducted over these intervals instead of arbitrary choices, such as 1 second, or 1 measurement snapshot. Rms delay spread CDFs estimated using rms delay spread values evaluated from single snapshots (each being a spatial average of data from all 32 array elements), from averaging over 1 second and from averaging over consistency intervals were then compared. Results showed that CDFs for rms delay spreads estimated from single snapshot data sometimes included extreme values. On the other hand, results from 1 second averages indicated too much smoothing. Both these effects influenced the tails of rms delay spread distributions significantly. However, the medians from averages over 1 second and over CIs are very close to each other. It is therefore concluded that for broad system design applications, arbitrary averages over 1 or several seconds are adequate, but for applications requiring knowledge of maximum values, averaging over CIs gives results that are less likely to be influenced by either excessive smoothing or extreme values.

- Through simulations, modelling, and measurements it was found that rms delay spreads are a function of measurement system bandwidth. They decrease rapidly

for RF bandwidths between 10 MHz and about 30 MHz, then level at approximately 50 MHz, continuing thereafter at a constant, minimum value. This is because it is only at bandwidths above about 50 MHz, that the envelope enclosing the last received multipath component falls rapidly enough on its trailing edge that the spreading due to the finite bandwidth is insignificant, and this doesn't change significantly as bandwidth increases further. A polynomial equation is reported in Chapter 4 for estimating rms delay spreads for systems with different bandwidths. This equation could be fine tuned, given estimates from reported measurements made by others of rms delay spreads for a specific bandwidth, in order to estimate equivalent results for greater bandwidths. This would allow measurement results reported by different researchers and for different operating environments to be compared more accurately than comparisons that are possible without this knowledge. In addition, it would make narrower bandwidth measurements reported over the past 3 decades useful for engineering work associated with the conception, development and deployment of future systems with considerably wider bandwidths.

- Based on the foregoing conclusion, it is considered that rms delay spreads reported herein for measurements with a 50 Mchps channel sounder (100 MHz RF bandwidth) are appropriate for work concerned with future systems that could operate with bandwidths as high as 100 MHz. This is because of the leveling off of the rms

delay spread/bandwidth relationship at bandwidths slightly lower than the bandwidth of the sounder used during this project.

(b) Radio Propagation in Microcells

- In microcells, there is always a dominant angle from which multipath waves arrive at a mobile station. This is the direction towards the base station (i.e. the transmitter in propagation measurement work reported here) in LOS scenarios and the direction towards the nearest street intersection or gap between buildings in the general direction of the base station in NLOS scenarios.
- On NLOS streets, angular dispersion is greatest at intersections and near gaps between buildings where energy can propagate from the street where the transmitter is located and impinge from the side, adding to persistent energy that propagates along the street canyon, and increasing the angular dispersion.
- In microcells, angular dispersion in azimuth and delay dispersion are both significantly lower on LOS streets than they are on either perpendicular NLOS streets or parallel NLOS streets. The ninetieth percentiles of rms delay spreads for different streets in the measurement area studied during this thesis project ranged between 21 ns and 73 ns for LOS streets, between 143 ns and 270 ns for perpendicular NLOS streets, and between 284 ns and 515 ns for parallel NLOS

streets. The ninetieth percentiles of azimuth angular spreads on different streets ranged between 5 and 33 deg. for LOS streets, between 24 and 73 deg. for perpendicular NLOS streets and between 53 and 121 for parallel NLOS streets.

- The numerical dispersion values reported in the foregoing can be used to fine tune models and simulations, as well as in systems design considerations. For instance, the greater delay dispersion on NLOS streets means that if microcell systems were designed to cover such areas, rather than just short LOS street sections, error rate floors would be encountered at symbol rates of about 100K symbols per second, in the absence of equalization and coding. Because the latter impairment mitigation methods automatically cause reductions in throughput, it can be concluded that for simple SISO systems, microcells that cover NLOS areas would suffer from reduced throughput and exhibit non-uniform coverage characteristics. However, with due consideration for the fact that increased dispersion can never fully compensate for reduced SNR, in cases where sophisticated processing and/or MIMO operation is employed, the increased dispersion in both domains could, perhaps, yield throughput gains (i.e. through diversity) in NLOS regions that could partially compensate for decreases in SNR with respect to that achievable under LOS condition. It is conceivable that this could make link performance (at an acceptable, but sub-LOS level) approximately uniform in one or two block microcells covering both LOS and

NLOS areas. It appears therefore, that future microcell system design will involve tradeoffs between the cost of increased infrastructure to provide LOS coverage in all areas and increased equipment cost to provide greater signal processing capabilities in NLOS areas.

(c) Microcell channel modeling

- As a result of the good comparison of rms delay spread results obtained from both raw measurement data and filtered measurement data with rms delay spreads estimated from a single interaction geometrical channel model, it can be concluded that such a model is appropriate for LOS microcells. However, since similar comparisons between measurement and modeling results for NLOS cases were not very good, it is concluded that a single bounce reflection model is not a good model for NLOS microcell scenarios.
- Knowledge of consistency intervals reported herein has two applications. It can be used to establish averaging intervals for the estimation of such results as rms delay spreads and angular spreads as discussed earlier in this section. In addition, this knowledge is useful for controlling when multipath parameter changes should be made during channel simulations. Interest in making such changes arises from consideration of possible performance gains that can be achieved through adaptivity,

and the need for more realistic simulators to test adaptive algorithms and evaluate achievable gains. Although the initial work on consistency intervals observed that there are deterministic trends in consistency interval plots, in such an application, intervals between simulator changes could, as a first step, be made random, having minimum and maximum values, as reported herein for CIs, being: a minimum of about 1 centimetre and a maximum of 22 metres along a mobile receiver's trajectory for LOS streets in microcells, a minimum of 1 centimetre and a maximum of 6 metres for parallel NLOS streets in microcells and a minimum of 1 centimetre and a maximum of 4 metres for perpendicular NLOS streets in microcells.

5.3 Recommendations for Further Research

A number of topics were identified during the course of this thesis project as being pertinent, but for various reasons, including equipment and time limitations, these could not be addressed. They are therefore left as topics for future study, and can be cited as:

- The conduct of similar experiments using a 3D array, since angles of arrival in elevation, and changes thereof should also be studied.

- Work related to the minimization of the time required for high resolution estimates of the channel parameters to enable the more accurate identification of points of change. It is possible that estimation algorithms, other than those that are sub-space based, such as SAGE, would be more appropriate.
- Work to relate the groups of estimated AOAs to the physical environment in order to better understand the reflection, diffraction, and scattering mechanisms involved in radio propagation within microcells.
- Work to relate detected channel changes to the physical environment in order to improve the understanding of what causes the channel to change.
- Work to relate detected channel change intervals to intervals of varying behaviour of the received signal, such as the onset or end of intervals in which the channel process can be modelled as being wide sense stationary.
- The consideration of other methods for the detection of changes.
- Use of the tools that have been made available through the conduct of this thesis project to analyze more of the existing data from downtown Ottawa propagation experiments, including data from different transmitter locations, to improve on the statistical significance of results reported herein and produce a model of CIs, rms delay spreads, and angular spreads for urban microcells in cities similar to Ottawa.
- Work towards the development of a suitable model for the simulation of channel

impulse response characteristics in NLOS scenarios in microcells.

- An analysis of errors associated with the plane wave assumption used in estimating AOA's in urban environments, and the effects of these errors on angular spread results.

References

- [1] R. Steele, "Toward A High-Capacity Digital Cellular Mobile Radio System," *Proc. Inst. Elect. Eng.*, vol. 132, pt. F, no. 5, pp. 405-415, August 1995.
- [2] K.I. Pedersen, P.E. Mogensen, and B.H. Fleury, "A Stochastic Model of The Temporal and Azimuthal Dispersion Seen at The Base Station in Outdoor Propagation Environments," *IEEE Trans. on Vehicular Tech.*, vol. 49, no. 2, pp. 437-447, March 2000.
- [3] P. Pajusco, "Experimental Characterization of DOA at The Base Station in Rural and Urban Area," *IEEE Vehicular Technology Conference 1998*, vol. 2, pp. 993-997, May 1998.
- [4] R.J.C. Bultitude, "Methods for Estimating Consistency Intervals and the Detection of Changes on Mobile Radio Channels," invited paper, URSI General Assembly, Chicago, August, 2008.
- [5] T.T. Soong, *Fundamentals of Probability and Statistics for Engineers*, Wiley, 2004
- [6] H. Krim and M. Viberg, "Two Decades of Array Signal Processing Research: The Parametric Approach," *IEEE Signal Processing Magazine*, vol. 13, pp. 67-94, July 1996.
- [7] A. Manikas, A. Alexiou, and H.R. Karimi, "Comparison of the Ultimate

- Direction-Finding Capabilities of a Number of Planar Array Geometries,” *IEE Proc.-Radar, Sonar Navig.*, vol. 144, no. 6, pp. 321-329, December 1997.
- [8] M.R.J.A.E. Kwakkernaat, *Design of a 3-D Switched Antenna Array for Mobile, High-Resolution Direction-of-Arrival Measurements*, Master of Science Thesis, Technische Universiteit Eindhoven, Eindhoven, The Netherlands, August 2004
- [9] L.C. Godara, “Application of Antenna Arrays to Mobile Communications, Part II: Beam-Forming and Direction-of-Arrival Considerations,” *Proceedings of the IEEE*, vol. 85, no. 8, August 1997.
- [10] B.D. Van Veen and K.M. Buckley, “Beamforming: A Versatile Approach to Spatial Filtering,” *IEEE ASSP Magazine*, pp. 4-24, April 1988.
- [11] R.O. Schmidt, “Multiple Emitter Location and Signal Parameter Estimation,” *IEEE Trans. Ant. Prop.*, vol. 34, no. 3, pp. 276-280, March 1986.
- [12] X.L. Xu and K. Buckley, “An Analysis of Beam-Space Source Localization,” *IEEE Trans. on SP*, vol. 41, no. 1, pp. 501–504, January 1993.
- [13] B. Friedlander and A. Weiss, “Direction Finding Using Spatial Smoothing with Interpolated Arrays,” *IEEE Trans. AES*, vol. 28, no. 2, pp. 574-587, April 1992.
- [14] T.J. Shan, M. Wax, and T. Kailath, “On spatial Smoothing for Directions of Arrival Estimation of Coherent Signals,” *IEEE Trans. ASSP*, vol. ASSP-33, no. 4, pp. 806-811, April 1985.

- [15] C.P. Mathews and M. D. Zoltowski, "Eigenstructure Techniques for 2-D Angle Estimation with Uniform Circular Arrays," *IEEE Trans. on SP*, vol. 42, no. 9, pp. 2395-2407, September 1994.
- [16] R. Roy and T. Kailath, "ESPRIT - Estimation of Signal Parameters via Rotational Invariance Techniques," *IEEE Trans. ASSP*, vol. ASSP-37, no. 7, pp. 984-995, July 1989.
- [17] M. Haardt, M.D. Zoltowski, C.P. Mathews, and J.A. Nossek, "2D Unitary ESPRIT for Efficient 2D Parameter Estimation," *Proceedings of the 1995 IEEE International Conference on ASSP*, vol. 3, pp. 2096-2099, May 1995.
- [18] M. Wax and T. Kailath, "Optimum Localization of Multiple Sources by Passive Arrays," *IEEE Trans. ASSP*, vol. ASSP-31, no. 5, pp. 1210-1217, October 1983.
- [19] J.A. Fessler and A.O. Hero, "Space-Alternating Generalized Expectation-Maximization Algorithm," *IEEE Trans. on SP*, vol. 42, pp. 2664-2677, October 1994.
- [20] M. Wax and T. Kailath, "Detection of Signals by Information Theoretic Criteria," *IEEE Trans. on ASSP*, vol. ASSP-33, no. 2, pp. 387-392, February 1985.
- [21] R.J.C. Bultitude and G.K. Bedal, "Propagation Characteristics on Microcellular Urban Mobile Radio Channels at 910 MHz," *IEEE Journal on Selected Areas in Communications*, vol. 7, no. 1, pp. 31-39, Jan. 1989.

- [22] J. Wiart, P. Pajusco, A. Levy, and J.C. Bic, "Analysis of Microcellular Wide Band Measurements in Paris," *PIMRC 1995*, vol. 1, pp. 144-147, Sept. 1995.
- [23] A.J. Paulraj, D.A. Gore, R.U. Nabar, and H. Bolcskei, "An Overview of MIMO Communications - A Key to Gigabit Wireless," *Proceedings of the IEEE*, vol. 92, no. 2, pp. 198-218, Feb. 2004.
- [24] R.J.C. Bultitude, G. Brussaard, et. al., "Radio Channel Modelling for Terrestrial Vehicular Mobile Applications," *Proc., ICAP/JINA Millennium Conference on Antennas and Propagation, Davos, Switzerland, April 2000*.
- [25] R.J.C. Bultitude, T.J. Willink, et. al., "Detection of Changes in The Spectral Characteristics of Measured Mobile Radio Data for Space Wave Modelling Applications," *Proc. Queens University Biennial Symposium on Communications, Kingston, Canada, pp. 90-94, May 2000*.
- [26] R.J.C. Bultitude, and M.H.A.J. Herben, "Segmentation of Measured Data and Modelling of The Nonstationary Characteristics of Narrowband Radio Channels in Urban Microcells," *COST273 Temporary Document TD03-135, presented in Paris, France, May 2003*.
- [27] D.C. Cox, "Delay Doppler Characteristics of Multiple Propagation at 910 MHz in A Suburban Mobile Radio Environment," *IEEE Trans. Antennas Propagat.*, vol. 20, no. 5, pp. 625-635, Sept. 1972.

- [28] J.C.-I. Chuang, "The Effects of Multipath Delay Spread on Timing Recovery," *IEEE Trans. on Vehicular Tech.*, vol. 36, no. 3, pp. 135-140, Aug. 1987.
- [29] IST-4-027756 WINNER II D1.1.1 V1.2 *WINNER II Interim Channel Models*
- [30] R. B. Ertel, P. Cardieri, K. W. Sowerby, T. S. Rappaport, J. H. Reed, "Overview of spatial channel models for antenna array communication systems," *IEEE Personal Communications*, vol. 5, no. 1, pp. 10 – 22, February 1998.

Acronyms

A/D	Analog to Digital
AIC	Akaike's Information Criterion
AOA	Angle Of Arrival
APDP	Average Power Delay Profile
BS	Base Station
BPSK	Binary Phase Shift Keying
CDF	Cumulative Distribution Function
CI	Consistency Interval
CRC	Communications Research Centre
CW	Continuous Wave
ECDF	Experimentally-determined Cumulative Distribution Function
EPDF	Experimentally-determined Probability Density Function
ESPRIT	Estimation of Signal Parameters via Rotational Invariance Techniques
FIR	Finite Impulse Response
GBSBEM	Geometrically Based Single Bounce Elliptical Model
IPDP	Instantaneous Power Delay Profile
ISI	Inter-Symbol Interference

K-S tests	Kolmogorov-Smirnov tests
LNA	Low Noise Amplifier
LOS	Line Of Sight
MDL	Minimum Description Length
MIMO	Multiple Input Multiple Output
ML	Maximum Likelihood
MPC	Multipath Component
MS	Mobile Station
MUSIC	Multiple Signal Classification
NLOS	Non Line Of Sight
PAS	Power Azimuth Spectrum/Spectra
PDF	Probability Density Function
PDS	Power Delay Spectrum
PN	Pseudo Noise
RB	Real Beamspace
RMS	Root Mean Square
SAGE	Space-Alternating Generalized Expectation-maximization
SNR	Signal to Noise Ratio
UCA	Uniform Circular Array

ULA	Uniform Linear Array
UTCA	Uniform Tilted Cross Array
WSS	Wide Sense Stationary

Bibliography

- [1] G. D. Durgin, V. Kukshya, T.S. Rappaport, "Wideband measurements of angle and delay dispersion for outdoor and indoor peer-to-peer radio channels at 1920 MHz," *Antennas and Propagation, IEEE Transactions on*, Volume 51, Issue 5, May 2003, Page(s):936 – 944.
- [2] N. Blaunstein, M. Toeltsch, J. Laurila, E. Bonek, D. Katz, P. Vainikainen, N. Tsouri, K. Kalliola, H. Laitinen, "Signal Power Distribution in the Azimuth, Elevation and Time Delay Domains in Urban Environments for Various Elevations of Base Station Antenna," *Antennas and Propagation, IEEE Transactions on*, Volume 54, Issue 10, Oct. 2006, Page(s):2902 – 2916.
- [3] L. Vuokko, K. Sulonen, P. Vainikainen, "Analysis of propagation mechanisms based on direction-of-arrival measurements in urban environments at 2 GHz frequency range," *Antennas and Propagation Society International Symposium, 2002 IEEE*, Volume 1, June 2002, Page(s):248 – 251.
- [4] M. Toeltsch, J. Laurila, K. Kalliola, A. F. Molisch, P. Vainikainen, E. Bonek, "Statistical characterization of urban spatial radio channels," *Selected Areas in Communications, IEEE Journal on*, Volume 20, Issue 3, April 2002, Page(s):539 – 549.

- [5] A. Kuchar, J. P. Rossi, E. Bonek, "Directional macro-cell channel characterization from urban measurements," *Antennas and Propagation, IEEE Transactions on*, Volume 48, Issue 2, Feb. 2000, Page(s):137 – 146.
- [6] J. Fuhl, J. P. Rossi, E. Bonek, "High-resolution 3-D direction-of-arrival determination for urban mobile radio," *Antennas and Propagation, IEEE Transactions on*, Volume 45, Issue 4, April 1997, Page(s):672 – 682.
- [7] H. Masui, M. Ishii, K. Sakawa, H. Shimizu, T. Kobayashi, M. Akaike, "Microwave spatial-temporal channel characteristics measured at base station in an urban environment," *Vehicular Technology Conference, 2000. IEEE VTS-Fall VTC 2000. 52nd*, Volume 2, Sept. 2000, Page(s):829 – 832.
- [8] M. Ghoraishi, J. Takada, T. Imai, "Identification of Scattering Objects in Microcell Urban Mobile Propagation Channel," *Antennas and Propagation, IEEE Transactions on*, Volume 54, Issue 11, Part 2, Nov. 2006, Page(s):3473 – 3480.
- [9] M. Ghoraishi, J. Takada, T. Imai, "Microcell urban propagation channel analysis using measurement data," *Vehicular Technology Conference, 2005. VTC-2005-Fall. 2005 IEEE 62nd*, Volume 3, Sept., 2005, Page(s):1728 – 1731.
- [10] A. A. Arowojolu, A. M. D. Turkmani, J. D. Parsons, "Time dispersion measurements in urban microcellular environments," *Vehicular Technology Conference, 1994 IEEE 44th*, Volume 1, June 1994, Page(s):150 – 154.